UNIVERSITÉ DE GRENOBLE

THÈSE

Pour obtenir le grade de

DOCTEUR DE L'UNIVERSITÉ DE GRENOBLE

Spécialité : **Nano Electronique et Nano Technologies**

Arrêté ministériel : 7 août 2006

Présentée par

Lin YOU

Thèse dirigée par **François BERTIN** et
codirigée par **Georges BREMOND**

préparée au sein du **Laboratoire d'Electronique et des Technologies de l'Information (LETI) du CEA Grenoble**
dans **l'École Doctorale Electronique, Electrotechnique, Automatisme et Traitement du Signal (EEATS)**

Optimisation de la mesure du travail de sortie par microscopie à sonde locale sous vide : application aux dispositifs avancés

Thèse soutenue publiquement le **01 juin 2012**,
devant le jury composé de :

M. Abdelillah EL HDIY
Professeur, LMEN, Université de Reims - Rapporteur

M. Thierry MELIN
Chargé de recherche, IEMN, Lille - Rapporteur

M. Michel RAMONDA
Ingénieur de recherche, CTM, Université de Montpellier -Examinateur

M. Ahmad BSIESY
Professeur, LTM, Grenoble - Examinateur

M. François BERTIN
CEA-LETI-MINATEC, Grenoble –Directeur de thèse

M. Georges BREMOND
Professeur, INL, INSA, Lyon – Co-directeur de thès

Acknowledgements

First, I want to thank my thesis advisor François Bertin and co-advisor Georges Bremond, who built up this project and offered me a chance to work in the top-level of semiconductor research team. Without them, this PhD work can never be carried out. I am thankful for their constant guild that leads me to become a great scientist.

I am also very grateful to my supervisor Nicolas Chevalier, with whom I had lots of fruitful discussions. I remember, sometimes, we debated on some small but deep questions for hours till very late that nobody else is still in the offices. However, such brain storming always turns out to be progress in work. It was a really pleasure to work with him.

For the thesis, I am grateful to other the board members: Abdelillah EL HDIY, Thierry MELIN, Michel RAMONDA, Ahmad BSIESY. Their positive comments and insightful questions contribute to the final version.

I am very thankful to Denis Mariolle, Martin Kogelschatz and Lukasz Borowik for introducing me the various AFM systems. With their expert guidance, patience and support at all levels, my research can leap ahead.

I would like to thank Guy Feuillet and their team for providing me the thin-film photovoltaic sample; thank Eugénie Martinez and Jean-Paul Barnes for your precious support in SAM and Tof-SIMS measurements.

I would like to express my thanks to Jean-Claude Royer and Frédéric Laugier not only for welcoming me aboard when I started the PhD but also for the help and support in the past three years.

I would say thanks to Claude Viguier from Omicron, Romain Stomp from Nanonis. With the strong link and communication with the systems manufacturer, our research can move forward smoothly.

I thank all the other colleagues involved in this projects and my Ph.D. life here. I sincerely hope that we would have opportunities to cooperate together in the near future.

Abstract

The development of nanoscience makes the understanding of the electrical properties of nano-objects essential. The Kelvin Force Microscopy (KFM) is a well suited technique to map at the nanoscale and simultaneously both the topography and contact potential difference (CPD). After 20 years of development, KFM is mainly operated under air at normal pressure, allowing to perform, in an easy way, multiple comparative analyses. However, under UHV, as the surface is controlled, more accurate and reliable measurements can be achieved. In the first part, KFM under ambient atmosphere is improved by developing the single-scan method using either a frequency modulation (FM) or an amplitude modulation (AM) mode. An external Nanonis electronic has been implemented on commercial AFMs (Dimension 3100 and MultiMode, Bruker). A comparative study with the common Lift-mode is done by imaging epitaxial graphene layers on SiC sample. The tip-sample separation effect on the CPD contrast and resolution is described as well as experimental settings. It is shown that higher contrasts are obtained using single-scan frequency modulation KFM regardless the tip-sample operating distance. In a second part, the KFM technique under secondary vacuum is developed. The instrumental work is carried out with an EnviroScope AFM from Bruker. We outfitted our Veeco's AFMs with an external Nanonis electronic to perform simultaneously the acquisition of topography and CPD using either the amplitude or the frequency modulation mode. The upgrade of the electronic has raised compatibility issues. Our results show that the comparable results are obtained with KFM under UHV. Finally, having laid down both the experimental and theoretical groundwork of the KFM, this technique is used to characterize CdTe/CdS heterostructures used in thin films solar cell application. A protocol for the cross section sample preparation has been specifically developed. The CdTe/CdS heterojunction is studied under polarization both in dark and under illumination. The influence of the CdS layer thickness is also studied to understand its dramatic effect on the solar cell efficiency.

Keywords: Atomic force microscopy (AFM), Kelvin force microscopy (KFM), work function, CdTe/CdS, heterojunction.

Table of contents

General introduction

The miniaturization is currently playing an important role in research and development on materials (semiconductors, data storage, biomaterials, health care and others). This development makes essential the availability of characterization tools operating at the nanoscale. This is why in recent years an increasing number of analytical methods have been introduced for comprehensive analyses at the nanometre scale. The scanning probe microscopy (SPM) techniques are of particular interest because of their capabilities to measure, at the nanoscale, surface morphology together with a surface physicochemical property. Among these accessible properties, the surface potential distribution (a quantity closely related to the work function), has grown considerably in interest to understand many chemical and physical surface and interface phenomena. Among these phenomena we can cite: semiconductors doping profiling, imaging trapped surface charges in insulators, chemical identification of individual surface species, many aspects of biology, the formation of organic and hybrid photovoltaic thin films and graphene. The Kelvin probe force microscope (KFM) is a surface technique extremely sensitive to any changes of surface properties in term of structure, composition and contamination. KFM is an AFM-based technique well suited to map the local contact potential difference (CPD) variation at the nanoscale.

Under normal atmosphere, the KFM technique is usually operated in Lift-mode, with a spatial resolution not better than 50 nm. The Lift-mode is a double pass technique that acquires the topography during the first scan and the CPD during the second scan. Obviously the acquisition time of the double pass mode is twice the one of the standard single pass mode. Moreover, due to the long-range electrostatic interaction, the CPD depends on the tip-sample distance. Therefore, a new KFM operating mode is highly desirable to both decrease the dependence of the CPD on the tip-sample distance and to increase the spatial resolution.

KFM operated under ultrahigh vacuum (UHV), using the so-called non-contact mode, is both more reliable and more sensitive, mainly for two reasons:

- Firstly, as KFM is susceptible to environment artifacts, UHV provides a better surface conditioning. Indeed, in air the work function of a sample depends on the surface quality that can be heavily altered by the presence of a thin film of water and/or by the presence of a contamination layer. This affects both the contrast of the CPD images and the value of the work function.

- Secondly, under vacuum the quality factor is typically up to 100 times higher than the one obtained when operating under normal atmospheric pressure. This higher quality

factor improves the sensibility of the force/gradient detection. However, the high cost of the set up and the difficulty to operate in non-contact mode have been an impediment to the development of this technique.

In this context, one aim of this thesis is to meet this challenge by developing robust protocols to operate KFM under secondary vacuum. We will give the pros and cons of operating under ambient atmosphere, secondary and ultrahigh vacuum.

The second aim of this thesis is to study CdTe/CdS heterojunction using the KFM technique to gain a better understanding of the conduction mechanisms in alternative CdTe/CdS-based solar cell. These solar cells are less expensive than their silicon-based contenders, but their theoretical efficiency can only reach 29 %. As standard analytical techniques usually yield only averaged properties over the probe size, the KFM technique is essential to image the local electrical properties, information necessary to understand the transport mechanisms allegedly responsible for the efficiency variability of these solar cells.

The presentation and discussion of the results obtained during this doctoral work is organized in four chapters:

Chapter 1 provides a reminder of the basics in three fields addressed in this thesis: the work function, the atomic force microscopy as well as the Kelvin probe force microscopy. The theory of the work function is introduced. The concept of the local work function is also presented. Then, the working principle of atomic force microscopy and its different operation modes are briefly overviewed. Finally, the work function measurement by Kelvin probe force microscopy is introduced. Working principle including different operation modes such as amplitude or frequency modulation and the expected contrast and accuracy are discussed.

Chapter 2 is focused on instrumental improvements of the KFM technique performed in ambient atmosphere. The single-scan acquisition has been implemented on commercial AFMs (Dimension 3100 and MultiMode from Bruker) by using external Nanonis electronic. A comparative study of the single scan operation both in frequency and amplitude modulation with the common Lift-mode is performed in ambient atmosphere by imaging graphene layers on SiC sample. The tip-sample separation effect on the surface potential spatial resolution and the contrast is described. Finally, the influence of the main experimental settings on CPD imaging is presented. We will show that higher contrasts are obtained using single-scan frequency modulation KFM regardless the tip-sample operating distance.

Chapter 3 is focused on the instrumentation of KFM under secondary vacuum. This work is carried out with a commercial AFM (EnviroScope, Bruker). An external Nanonis

electronic has been implemented to perform, both in amplitude and frequency modulation mode, simultaneous acquisition of topography and CPD. A thorough presentation of the experimental setup, the effects of experimental conditions and parameters are detailed. In the end, a comparative study with KFM in ambient conditions shows the importance to work under secondary vacuum.

Chapter 4 highlights the combination of high resolved CPD imaging by KFM and nano-resolved Auger electron spectroscopy (AES) on CdTe/CdS heterojunction. A protocol for the cross section sample preparation has been specifically developed. The CdTe/CdS heterojunction is studied under polarization both in dark and under illumination. The influence of the CdS layer thickness is also studied to understand its dramatic effect on the solar cell efficiency.

Finally we summarize the main results obtained during this work.

Chapter 1

Work function measurement by Kelvin probe force microscopy

In this chapter, we give a brief reminder of the theory of work function and how it is possible to measure the work function using an SPM-based technique: the Kelvin force microscopy (KFM). The chapter starts with a brief introduction to the work function theory insisting on the concept of local work function. Then, the basics of the atomic force microscopy (AFM) will be reminded to introduce the KFM technique. The reminder of the chapter is dedicated to a detailed discussion of the KFM two main operating modes: the amplitude modulation (AM) mode and the frequency modulation (FM) mode.

1.1 The theory of work function and concept of local work function

1.1.1 The theory of work function

Work function of metals

Classically, the work function ϕ is defined [1,2] as "the difference in energy between a lattice with an equal number of ions and electrons, and the lattice with the same number of ions, but with one electron removed". Let $F(N)$ be the initial free energy of neutral crystal with N electrons and $F(N-1)$ the final free energy of the crystal with $N-1$ electrons. If we assume that the extracted electron is at rest and therefore possesses only an electrostatic potential energy, we have:

$$\phi = F(N-1) + E_{\text{Vac}} - F(N), \tag{1.1}$$

where E_{Vac} is the vacuum level. In Eq. (1.1) the vacuum level energy can be set to zero but, as it will be shown the notion of vacuum level plays an important role and we will have to

distinguish the vacuum level (level at infinity) from the local vacuum level (near the surface).

The change in free energy $F(N-1)$-$F(N)$ is related to the chemical potential

$$\mu = F(N) - F(N-1) = \left(\frac{\partial F}{\partial N}\right)_{T,V}, \tag{1.2}$$

where the derivative of the free energy is taken at constant volume and temperature. By definition, the Fermi level E_F is equal to the value of the chemical potential μ at $T = 0\,\mathrm{K}$, and is quite constant for temperature that is much lower than the characteristic Fermi temperature[1] $\frac{E_F}{k}$. [3] So, we can safely write:

$$\phi = E_{\mathrm{Vac}} - E_F . \tag{1.3}$$

In another word, the work function is the energy difference between two states of a solid with an infinite homogeneous surface. In the initial state, the electrons fill all the available states up to the highest occupied level of the neutral ground state of the solid, i.e. the Fermi level E_F. In the final state, the solid is singly ionized with the electron being at infinity in vacuum at rest i.e. at the so called vacuum level E_{Vac}.

Theory of the double-layer

To deduce the Eq. (1.3) , two effects that affect the work function value have been ignored: firstly, when removing an electron through the surface of a conductor, work can be done or gained; secondly, the extracted electron electrostatically interacts with its image (Schottky interaction).

The first contribution can be ascertained through the presence of a double-layer located at the surface. The double-layer consists in two parallel planes with both uniform and opposite areal charge density σ. As it is well known the electric field vanishes outside the double layer while, inside the double-layer, the electric field takes a constant value equal to $\frac{\sigma}{\varepsilon_0}$. So, the work done or gained by the electron when it crosses the surface is:

$$W = -\frac{|e|\sigma d}{\varepsilon_0}, \tag{1.4}$$

[1] Typically, for metals $\frac{\mu(0) - \mu(300\mathrm{K})}{\mu(0)} \approx 0.01\%$.

where $|e|$ is the elementary charge of electron, σ the areal charge density of the lower plane, d the distance separating the two planes and ε_0 the vacuum permittivity. Equation (1.4) shows that depending on the sign of σ, the work W can be either positive or negative. The presence of the double-layer can have many different physical origins that fall into two categories: intrinsic or extrinsic. The extrinsic origins of the double layers encompass external alteration of the surface such as: oxidation, contamination, absorption… The intrinsic origins of the double layer encompass phenomena such as: lattice deformation of the upmost atomic layers (surface reconstruction), charge spilling, and band bending …

The second contribution – the Schottky interaction – is due to the fact that the removed charge $-|e|$, located at a distance x away from the surface, creates, inside the bulk, an image point charge $+|e|$ located at the distance x from the surface. The mutual Coulomb interaction between the removed electron and its image charge leads to the attractive potential:

$$\phi_{im} = \frac{-e^2}{16\pi\varepsilon_0 x}. \tag{1.5}$$

This potential vanishes only at infinity. Taking into account these two contributions the work function can be expressed as:

$$\phi = W + \phi_{\text{im}} - \mu \tag{1.6}$$

Surface dipole layer

The effect of the double-layer on the work function is often calculated on the basis of simplified assumptions about the nature and magnitude of dipoles. A simple model describes the dipole-induced work function as the work that undergoes an electron when crossing a parallel plate capacitor (plate separation d). If n_{Dip} is the dipole surface-density then, the charge density of one capacitor plate is $n_{Dip}|e|$ (see Fig. 1.1) so, the electric field between the two plates is

$$E = \frac{n_{Dip}|e|}{\varepsilon_0}. \tag{1.7}$$

Then, the work function change is given by:

$$\Delta\phi = -|e|Ed, \tag{1.8}$$

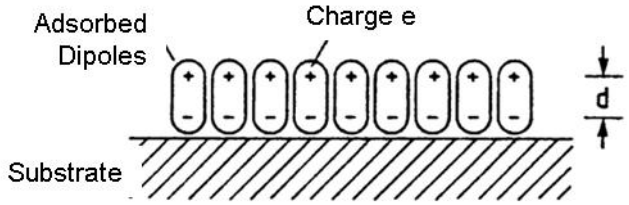

Fig. 1.1 Schematic representation of a well-ordered monolayer of highly-polar molecules with molecular dipole moment $|e|d$. Credit is from reference [4].

Using Eqs. (1.7) and (1.8) and using the expression $p = |e|d$ of the dipole moment of the adsorbed particle, we arrive at the expression,

$$\Delta\phi = -|e|\frac{n_{Dip}}{\varepsilon_0} p\,, \tag{1.9}$$

for the work function change.

Work function of semiconductors

In a semiconductor, the valence band is separated by a gap, of width E_G, from the conduction band. For a non-degenerated semiconductor, the Fermi level lies within the band gap. For a n-type semiconductor, the position of the Fermi level is closer to the conduction band than the one of an intrinsic material. For a p-type semiconductor, the Fermi level is closer to the valence band than the one of an intrinsic material.

Surface states can play an important role. Indeed, the filling or discharging of these surface states can lead to band bending [5,6,7,8], Fermi level pinning. All these phenomena can dramatically impact the work function.

In addition, when dealing with semiconductors, two properties, namely the electron affinity χ (>0) and the ionization energy IE (>0), are used. The electron affinity is defined as the energy required to excite an electron from the bottom of the conduction band E_{CB} to the local vacuum level (Fig. 1.2). Similarly, the ionization energy IE is defined as the energy needed to excite an electron from the top of the valence band E_{VB} to the local vacuum level. Although no electron can occupy the Fermi level, the work function is still defined as: $\phi = E_{\text{Vac}} - E_F$. This choice will be justified afterwards. Therefore, the work function can be defined by one of the following expressions:

$$\phi = \chi - |e|V_{BB} + (E_{CB} - E_F)_{bulk}\,, \tag{1.10}$$

or

$$\phi = IE - |e|V_{BB} - (E_F - E_{VB})_{bulk}\,, \tag{1.11}$$

where e is the elementary charge of electron.

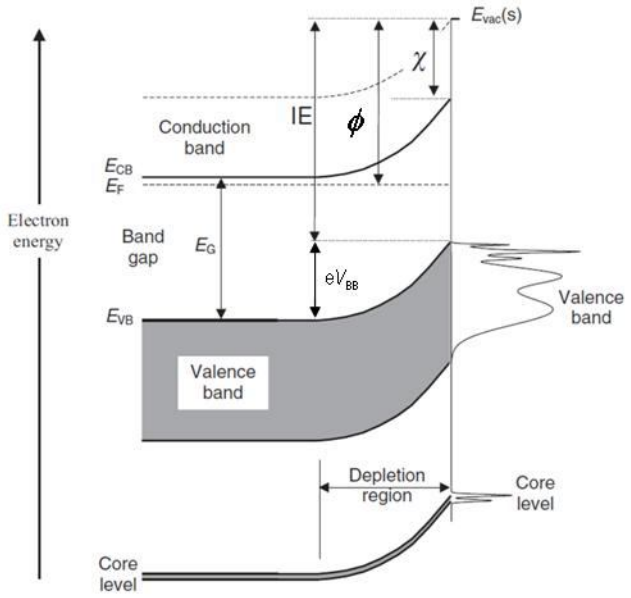

Fig. 1.2 Energy band of a semiconductor near its surface showing the band bending eV_{BB}, the electron affinity χ, the ionization energy IE, the band gap E_G and the edges of the conduction and valence band E_{CB} and E_{VB} respectively. Credit from reference [9].

1.1.2 The concept of local work function

Up to now, the work function has been deduced for ideal surfaces that are perfectly flat, infinitely extended, covered with uniform chemical contamination and/or structural distortion resulting in a uniform dipole layer. However, the real surfaces are rough, limited in size, non homogeneous and most of the time subject to non uniform contamination/oxidation. The difference in work function from one area to another can be related to the surface preparation, to non uniform distribution of adsorbates, to variation of crystallographic orientations or to variations in surface local geometry. [10], [11] Such non uniform surfaces are commonly encountered in materials surface characterization. Therefore, the understanding of these non uniformities on local work function is mandatory.

To analyze the consequences of the surface non uniformity on the work function, let consider two paths P_1 and P_2 with two different dipole real densities and, therefore, with two different work functions ϕ_1 and ϕ_2. Let extract an electron at the Fermi level through the surface of the patch P_1 and bring it back, through the surface of the patch P_2, to the crystal Fermi level. The energy conservation imposes that the net work done in such a cycle vanishes. However, the work done along this circuit is equal to $\phi_1 - \phi_2$. Therefore, as $\phi_1 \neq \phi_2$ the net work can be zeroed if an electrical potential φ is such that:

$$-|e|(\varphi_1 - \varphi_2) + \phi_1 - \phi_2 = 0. \qquad \textbf{(1.12)}$$

As the surface dipole layer cannot yield macroscopic fields outside of the metal, the electric field outside the metal must arise from net macroscopic distributions of electric charges on the surface (known as "patch charges"). These surface charges build the electric potential φ in the vacuum leading to the concept of local vacuum energy defined as the energy $E_{\text{Vac}} = -|e|\varphi(\vec{r})$.

To sum up, the local work function can be locally affected by changes in surface properties and/or changes in bulk chemical potential. These changes result in a non uniform surface charge that in turn creates an electrical potential in the vacuum. This potential affects the energy of the local vacuum level.

1.2 Principles and basics of Kelvin probe force microscopy

KFM is a scanning probe microscopy technique capable to image the electronic surface properties, namely the contact potential difference (CPD). It is based on the atomic force microscopy (AFM) and minimizes the electrostatic interaction occurring between a conductive tip and the surface. Therefore, the description of the KFM technique requires an understanding of some basics of the working principle of the AFM technique. Thus, we provide a brief introduction of some concepts of the AFM before detailing the KFM principle.

1.2.1 Brief introduction to atomic force microscopy (AFM)

Imaging individual atoms was a rather difficult goal until the invention of the scanning tunneling microscope (STM) by Binnig *et al.* in 1981. [12] This instrument provided a breakthrough in the ability to investigate matter at the atomic scale. Indeed, for the first time, the individual surface atoms of flat samples were visible in real space. However, the STM technique was quickly limited to image conductive samples such as metals and semiconductors. In 1986, Binnig and Quate invented the AFM technique to overcome this limitation. [13] The basic idea of AFM is a system based on a sharp tip that can “feel” the atomic force close to the sample surface and so map the surface topography. Strong developments to sharp the tip and improve the working environment have been performed during one decade. Atomic resolution imaging has finally been achieved by Giessibl on silicon (111) in 1995. [14]

1.2.1.1 Working principle

The simplified schematic of AFM setup is shown in Fig. 1.3. The probe is formed by a micro-sharp tip mounted at the end of a cantilever. While the tip interacts with the

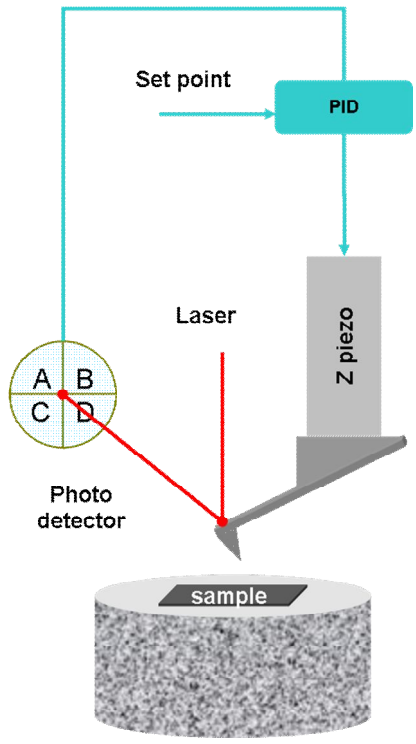

Fig. 1.3 The basic schematic of AFM setup

surface, the cantilever moves depending on the nature of the interaction force (i.e. repulsive or attractive). These movements are transferred to a four segment photodiode by means of a reflected laser beam at the end of the cantilever. An electrical current corresponding to the laser beam movement is therefore created in the photodetector. This current is then converted into a voltage signal that is compared to a setpoint value dictating the desired position of the cantilever.

The resulting error signal is then used by the proportional-integral-derivative (PID) controller to maintain the tip at constant tip-sample separation. The vertical movement of the tip is provided by a piezo-electric ceramic tube moving in the z direction. The lateral scan of the tip in the x and y directions over the surface is provided by two additional piezo-electric ceramics. The variations of the vertical piezo at each x and y position are recorded to provide the topography of the scanned surface $h(x,y)$.

1.2.1.2 Different modes of AFM

Two operation modes of AFM can be used: the static mode (also called contact-mode) and the dynamic mode.

Contact-mode

The contact-mode was developed in the prototype of AFM proposed by Binnig *et al*. [13] The AFM tip makes a soft "physical contact" with the sample in the repulsive force region

(see Fig. 1.4). The tip is in contact with the sample surface and the repulsive force translates into a deflection of the cantilever. This deflection of the cantilever is used as a feedback signal to maintain a constant force during scanning. Because the deflection of the cantilever should be significantly larger than the deformation of the tip and the sample, restrictions on the useful range of k apply. The cantilever should be much softer than the bonds between the bulk atoms in the tip and sample. Interatomic force constants in solids are in a typical range from 10 N/m to approximately 100 N/m, whilst in biological samples they can be as small as 0.1 N/m. Thus typical values for k in the static mode range between 0.01 N/m to 5 N/m depending on the application. [15] More details can be found in literature of applications of the contact mode, such as: manipulation of nanostructures [16], charge injection [17] as well as conductivity [18,19] and capacitance [20] measurements.

Dynamic mode

In the dynamic operation mode, the cantilever is mechanically vibrated resulting in an oscillation of the tip at very small distance above the surface. Unlike the static mode, which operates in the repulsive region, the dynamic mode averages the force over the amplitude oscillation of the cantilever (see Fig. 1.4). Two different strategies can be employed to work in dynamic mode: we can modulate the amplitude or we can modulate the frequency. Before detailing these two methods, basics of the cantilever dynamic are introduced by using the harmonic oscillator model.

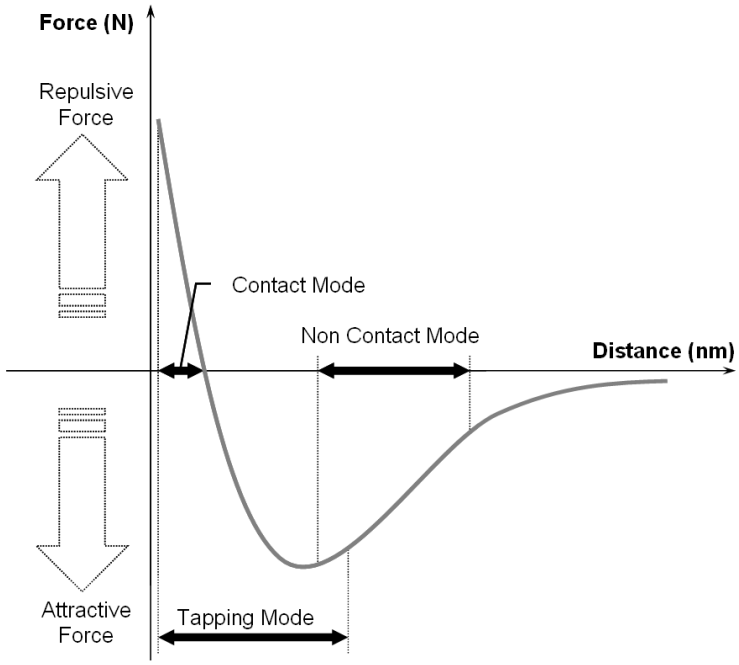

Fig. 1.4 Plot of the interatomic force as a function of distance. The regions of three AFM modes are indicated: contact-mode (or static mode) operating in the repulsive region, the Tapping™ and non-contact modes (dynamic modes) operating respectively in attractive/repulsive and attractive regions.

Dynamic of the cantilever: a harmonic oscillator model

The thorough understanding of the dynamic mode requires solving the motion equation of the cantilever-tip system under the influence of the tip-surface forces. [21,22] The cantilever-tip system can be modeled as a point-mass spring system, acting as an oscillator as shown in Fig. 1.5. Figure 1.4 shows that the tip-sample interaction is non linear and a rigorous solution of the motion equation is rather difficult to calculate by analytical approach. However, if the interacting forces between the tip and the sample are considered to be relatively weak during the tip oscillation, the dynamic motion of the cantilever can be simplified as a simple harmonic oscillator (Fig. 1.5).

Far to the surface sample, the motion equation of the mechanically driven cantilever with damping caused by the viscous friction of the cantilever is given by:

$$m^*\ddot{z} + c\dot{z} + kz = F_{ext}\cos(\omega t), \qquad \textbf{(1.13)}$$

where m^* is the effective mass of the point-mass[2], c is the viscous damping coefficient, k is the spring constant, F_{ext} and ω are respectively the amplitude and the angular pulsation of the driving force. Considering $\gamma = \frac{c}{m^*}$ and knowing the resonant angular pulsation $\omega_0^2 = \frac{k}{m^*}$ implies:

$$\ddot{z} + \gamma\dot{z} + \omega_0^2 z = \frac{F_{ext}}{m^*}\cos(\omega t). \qquad \textbf{(1.14)}$$

In the harmonic oscillator model, the solution of the above equation is given by:

$$z(t) = A(\omega)\cos(\omega t - \varphi(\omega)), \qquad \textbf{(1.15)}$$

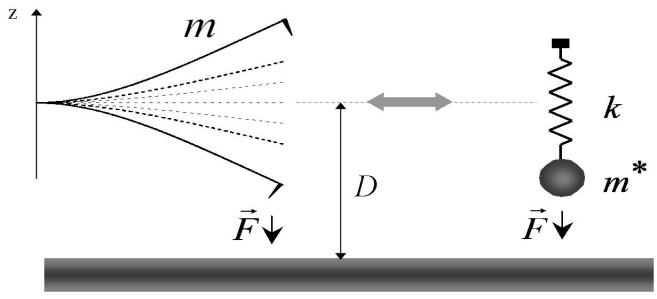

Fig. 1.5 In dynamic operation mode, the oscillating cantilever can be modeled by a point-mass spring system with a single degree of freedom.

[2] A rigorous estimation of the effective mass gives m^* = 0.243 m, where m is the mass of the cantilever with the tip mounted at its extremity.

where $A(\omega)$ and $\varphi(\omega)$ represent respectively the amplitude of the cantilever oscillation and the phase delay of the oscillation with respect to the driving force signal, which can be deduced by using Eqs. (1.14) and (1.15):

$$A(\omega) = \frac{F_{ext}}{m^*} \frac{1}{\sqrt{(\omega_0^2 - \omega^2)^2 + \gamma^2 \omega^2}}, \quad \textbf{(1.16)}$$

$$\varphi(\omega) = \arctan\left(\frac{\gamma\omega}{\omega_0^2 - \omega^2} \right). \quad \textbf{(1.17)}$$

The typical shape of the oscillation amplitude $A(\omega)$ and $\varphi(\omega)$ are shown in Fig. 1.6, where the abscissa represents the frequency $f = 2\pi\ \omega$.

If the tip-cantilever system is brought closer to the sample surface, non linear interaction forces $F_{int}(z)$ need to be taken into account. The free motion previously described by Eq. (1.14) can be rewritten as

$$\ddot{z} + \gamma\dot{z} + \omega_0^2 z = \frac{F_{ext}}{m^*}\cos(\omega t) + \frac{F_{\text{int}}(z)\big|_D}{m^*}, \quad \textbf{(1.18)}$$

where D is the mean position of the cantilever with respect to the sample (Fig. 1.5). In the case of small oscillations, the linear approximation is considered and it is rather possible to develop the interaction force F_{int} into a Taylor expansion at the first order around the equilibrium position D of the cantilever with respect to the sample:

$$F_{\text{int}}(z) \approx F(D) + z\frac{\partial F(D)}{\partial z}. \quad \textbf{(1.19)}$$

Thus by introducing this approximated expression in the Eq.(1.18), we can solve the cantilever equation:

$$\ddot{z} + \gamma\dot{z} + \left(\omega_0^2 - \frac{1}{m^*}\frac{\partial F(D)}{\partial z} \right) z = \frac{F_{ext}}{m^*}\cos(\omega t) + \frac{F(D)}{m^*}. \quad \textbf{(1.20)}$$

The term $F(D)$ induces a simple static deflection of the cantilever, which does not actually affect the treatment. However, by comparing Eq. (1.20) with the initial form of Eq. (1.14), one can see that the cantilever oscillating system in interaction with the sample gets a new angular pulsation ω_1 instead of the free resonant angular pulsation ω_0:

$$\omega_1 = \sqrt{\omega_0^2 - \frac{1}{m^*}\frac{\partial F(D)}{\partial z}} \approx \omega_0\left(1 - \frac{1}{2k}\frac{\partial F(D)}{\partial z} \right). \quad \textbf{(1.21)}$$

This relation shows that the force gradient induces a shift of the resonant angular pulsation of the cantilever. On the other hand, as shown in Fig. 1.6, attractive forces (i.e. $\frac{\partial F(D)}{\partial z} > 0$) induce a negative shift of the resonant angular pulsation, whilst a positive shift is expected for repulsive forces (i.e. $\frac{\partial F(D)}{\partial z} < 0$).

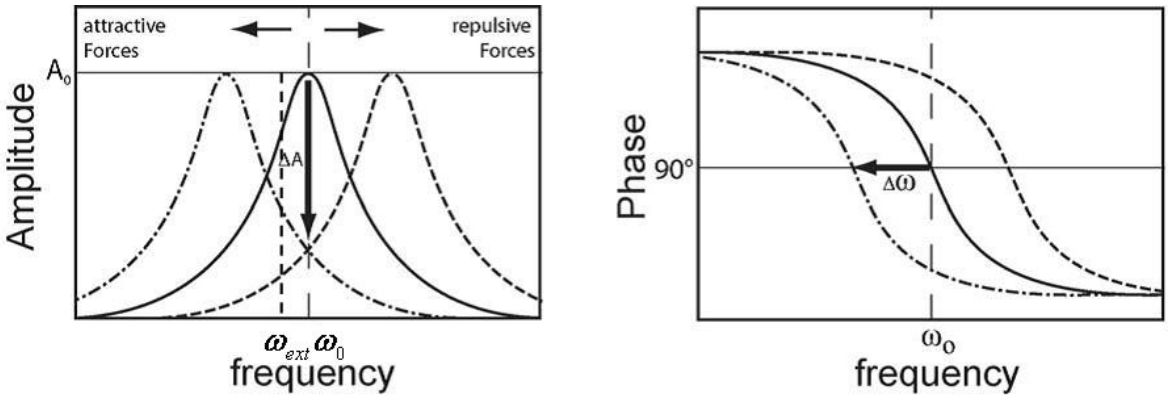

Fig. 1.6 Amplitude and phase response of a free oscillating cantilever (continuous line), with attractive interactions (dash-dot) and with repulsive forces (dashed line). Figure is adapted from the reference [23].

From the Eq. (1.21), an equivalent spring constant k_1 can be defined:

$$k_1 = k - \frac{\partial F(D)}{\partial z}. \qquad \textbf{(1.22)}$$

Everything happens as if, in the presence of attractive (repulsive) interaction with the sample, the stiffness of the cantilever decreases (increases) (Fig. 1.7). Of course, the non-linear behavior of the interaction force is more complicated. Interested reader will find more details on non-linear approach in the following references [24],[25],[26] and [27].

As mentioned above, amplitude-modulation (AM) or frequency-modulation (FM) operation methods can be used in dynamic mode. Brief descriptions of these methods, respectively namely Tapping™ and non-contact modes are presented hereafter.

Amplitude modulation method: Tapping™ mode

This mode was firstly proposed by Martin *et al*. in 1987. [28] In this mode, the cantilever is mechanically vibrated with a piezo actuator driven at fixed amplitude A_{ext} and at fixed frequency $f_{ext} = 2\pi\omega_{ext}$, where f_{ext} is close to the free resonant frequency f_0. As previously mentioned above, when the tip approaches the sample, elastic and inelastic interactions induce a change in both amplitude and phase of the cantilever relating to the driving signal (see Fig. 1.6). In Tapping™ mode, the amplitude $A(\omega_{ext})$ is used as a feedback signal; the amplitude setpoint A_{set} is typically set at 70 % of the free amplitude oscillation A_0. The transient time τ_{AM} of a damped oscillator is defined as $2Q/f_0$ then, the time necessary to acquire N data is at least equal to $N\tau_{AM}$. As in ultrahigh vacuum the quality factor Q can reach values as large as 30 000, the acquisition time of an image can be an issue. [15,29,30] However, AM-AFM operating under ultrahigh vacuum makes the atomic resolution possible. [31]

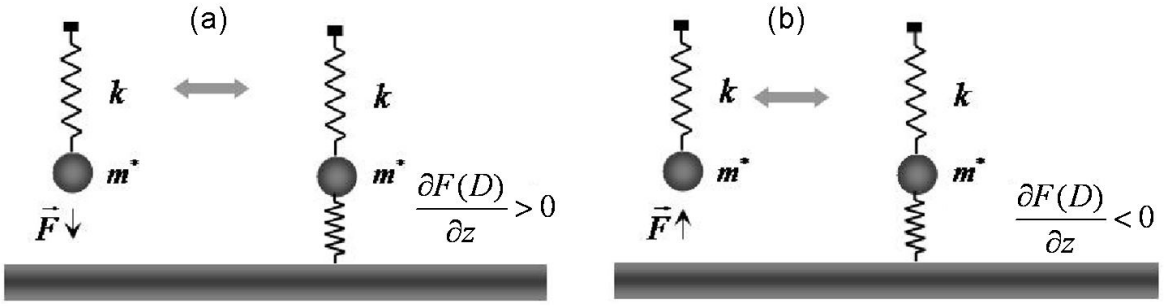

Fig. 1.7 In dynamic operation mode, the oscillating cantilever can be modeled by a simple harmonic oscillator with a single degree of freedom. The tip-sample interaction force can be modeled as an extra spring (a) pulling for attractive forces or (b) pushing for repulsive forces the mass point.

Frequency modulation method: non-contact mode

The frequency modulation mode was introduced by Albrecht *et al.* in 1991 to improve the AFM scan rate under vacuum. [32] The benefits of high Q factor and high speed have been combined by introducing the frequency modulation (FM) mode, where the change in the eigenfrequency occurs within a single oscillation cycle on the time scale of $\tau_{FM} = 1/f_0$. In this mode, the resonant frequency of the cantilever is commonly tracked by phase locked loop (PLL) technique, where the shift in resonant frequency is measured on the induced variations on the phase. In practice, the PLL consists of a low noise and fast controller which varies the excitation frequency to maintain the phase constant. From the Eq. (1.21), the frequency shift induced by tip-sample interaction forces can be estimated as:

$$\Delta f = \frac{\omega_1 - \omega_0}{2\pi} \simeq \frac{1}{2k}\frac{\partial F(D)}{\partial z} f_0 . \qquad \textbf{(1.23)}$$

In frequency modulation method, the frequency shift is used as a feedback signal. Typically, a negative frequency shift is used to work in non-contact mode. The FM mode can be done at constant driving signal [33] or at constant amplitude. In this latter case, the amount of excitation necessary to keep the amplitude constant can be interpreted in terms of energy dissipation. For interested reader, more details can be found in the following references [34], [35], [36].

1.2.2 Kelvin probe force microscopy (KFM)

1.2.2.1 Contact potential difference and detection

The contact potential difference (CPD) refers to the potential difference between two different materials after connecting them. This potential difference corresponds to the difference of work function between these two materials. This is illustrated in Fig. 1.8 with

an AFM tip and a metallic sample. It is noted that here we only discuss the simple case of an ideal metallic sample.

Before connecting the tip and the sample, their vacuum levels are aligned, both are electrically neutral. Once they are connected, due to the different work functions, electrons will move from the material with the lower work function to the material with the higher work function until the Fermi levels align (thermodynamic equilibrium). Consequently, the material with lower work function (i.e. the sample in Fig. 1.8) will lose some electrons and becomes electrically positive and vice versa. An electric field appears between the tip and the sample due the potential difference:

$$V_{CPD} = \frac{\phi_{tip} - \phi_{sample}}{|e|}, \tag{1.24}$$

where e is the elementary charge.

Kelvin probe force microscopy consists in measuring this CPD by cancelling out the electric field between tip and sample due to the work function difference by applying an external bias V_{dc} to the tip. In this case, V_{CPD} equals to V_{dc}.

Kelvin probe force microscopy is widely used to measure the CPD between the tip and the sample, thus providing additional sample properties on a lateral scale in the nanometer range. Since the work function of the tip is known or can be calibrated by a

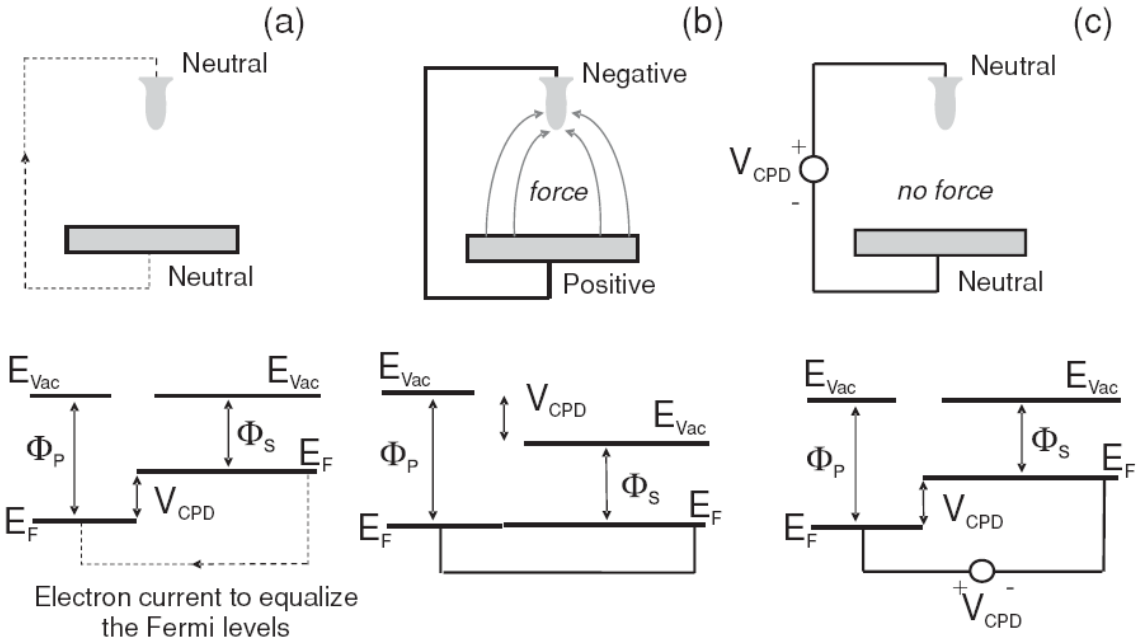

Fig. 1.8 Schematics of contact potential difference (CPD) between tip and sample, both of them are assumed to be metal. (a) Before contact and (b) after contacting. (c) After compensation of CPD with external bias. Figure is adapted from [37].

reference sample, the work function of the sample can be calculated by Eq.(1.24). The first KFM was developed by Nonnenmacher *et al.* in 1991 and it allows one to image surface electronic properties (i.e. contact potential difference). [38]

The name "Kelvin probe force microscope" comes from the macroscopic method developed by Lord Kelvin in 1898 using a vibrating parallel plate capacitor arrangement of capacitance C. When a voltage V is applied to one vibrating plate the resulting current is

$$i = (V_{CPD} - V)\frac{dC}{dt}. \quad \textbf{(1.25)}$$

So, while scanning, by automatically adjusting the dc bias voltage V to nullify the current i, we obtain a mapping of V_{CPD}. [39]

In KFM, the capacitance change dC/dt between the tip and the sample is very small and the current i can not be measured. To get around this difficulty in KFM, we nullify an electrostatic force in place of a current. To do so, in KFM, the sum

$$V = (V_{dc} - V_{CPD}) + V_{ac}\sin\omega_{el}t, \quad \textbf{(1.26)}$$

of an ac voltage $V_{ac}\sin(\omega_{el}t)$ and a dc voltage V_{dc} is applied between the tip and the sample.

Therefore, the resulting electrostatic force is:

$$F_{es} = -\frac{1}{2}\frac{\partial C}{\partial z}\left[V_{dc} - V_{CPD} + V_{ac}\sin(\omega_{el}t)\right]^2, \quad \textbf{(1.27)}$$

where $\frac{\partial C}{\partial z}$ is the tip-sample capacitance gradient. By developing Eq. (1.27), the force can be decomposed in three different components at three different frequencies:

$$F_{es} = F_{dc} + F_{\omega_{el}} + F_{2\omega_{el}}, \quad \textbf{(1.28)}$$

where

$$F_{dc} = -\frac{\partial C}{\partial z}\left[\frac{1}{2}(V_{dc} - V_{CPD})^2 + \frac{1}{4}V_{ac}^2\right], \quad \textbf{(1.29)}$$

$$F_{\omega_{el}} = -\frac{\partial C}{\partial z}(V_{dc} - V_{CPD})V_{ac}\sin(\omega_{el}t), \quad \textbf{(1.30)}$$

$$F_{2\omega_{el}} = +\frac{1}{4}\frac{\partial C}{\partial z}V_{ac}^2\cos(2\omega_{el}t). \quad \textbf{(1.31)}$$

It can be seen from Eq. (1.29) that, even if the CPD is compensated by the applied dc voltage (V_{dc}=V_{CPD}), the dc term F_{dc} of the electrostatic force F_{es} is proportional to V_{ac}^2 and

can not be nullified. This force may contribute to the topographical signal by inducing a constant bending of the cantilever.

The $F_{\omega_{el}}$ term at the angular frequency ω_{el} affects the tip with a periodic electrostatic force that can be modulated by adjusting V_{dc}, which changes the electrostatic field between the tip and the sample. This oscillating force can be nullified by adjusting V_{dc}=V_{CPD}. The V_{dc} voltage necessary to nullify the F_{ω} component of the force is recorded at each point of the surface which allows the potential V_{CPD} to be mapped.

The $F_{2\omega_{el}}$ term at the angular frequency $2\omega_{el}$ can be used for capacitance microscopy applications. [40]

1.2.2.2 Operation modes

KFM exists in two operation modes: amplitude modulation (AM) and frequency modulation (FM). In the following parts, both techniques are presented. The main difference between the two methods is that in FM-mode the electrostatic force gradient [Fig. 1.9(b)] is detected while in AM-mode the electrostatic force itself [Fig. 1.9(a)] is detected.

In an ideal case, only the apex of the tip interacts with the sample surface, but in reality cone/sample and cantilever/sample interactions also contribute to the detected signal, which decreases the resolution. In AM-KFM higher contributions of cone/sample and cantilever/sample interactions to the signal are expected than in the FM mode and therefore absolute and relative work function resolutions are different. This effect is illustrated in Fig. 1.12.

AM-KFM is widely used under vacuum in a single scan technique simultaneously with NC-AFM topography measurements or in ambient atmosphere in a double scan technique which consists in measuring the CPD in the so called Lift-mode combined with topography measurements in Tapping™ mode.

In AM-KFM combined with NC-AFM topography measurement the first resonant peak is commonly used for mechanical oscillation and thus topography measurements [details can be found in section 1.2.1.2], while an ac tip bias voltage is applied at the second resonant peak for the CPD measurement. [41]

There are two reasons to do so. Firstly, the second resonant frequency is approximately 6.3 times [42] higher than the first one which separates the topography and CPD measurement well. Secondly, applying an ac tip bias at the second resonant peak obviously gives highest sensitivity as the first resonant peak is already used for the topography measurement.

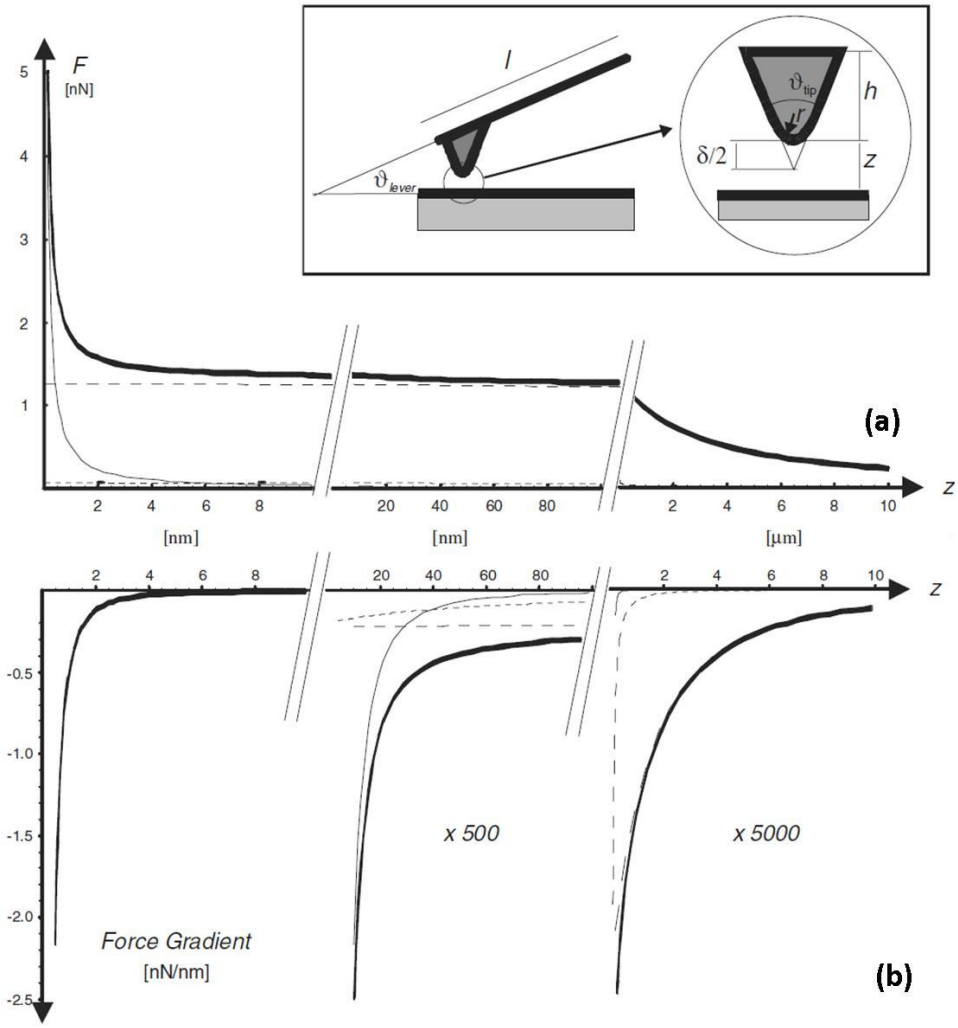

Fig. 1.9 (a) Electrostatic force and (b) electrostatic force gradient versus tip–sample distance calculated from A.Gil et al.'s model. The thick solid curve corresponds to the total electrostatic force [or force gradient in (b)], while the other three contributions from the cantilever (dashed line), the tip cone (short dash) and the tip apex (thin solid) are represented. These curves have been calculated for V_{dc} = 1 V, and a probe with a cantilever of 100 µm length and 40 µm width, a tip cone of 3 µm length and a radius of 20 nm for the tip apex. The opening angle for the tip is θ_{tip} = 45° and an angle of θ_{lever} = 20° was assumed between the cantilever and the sample. Inset: probe proposed for modeling an EFM set-up. This probe is composed of three basic units: a cantilever of length l, width w and tilting angle θ_{lever} with respect to the sample, a mesoscopic tip cone of height h and (full) opening angle θ_{tip}, as well as a parabolic tip apex of radius r. Figure adapted from reference. [43]

When operating under vacuum, most KFM measurements combined the NC-AFM and the FM-KFM modes and, as a consequence, all above mentioned artifacts are suppressed. To achieve enough sensitivity, the amplitude of V_{ac} in single-scan AM-KFM is commonly set between 1 V to 4 V. [37] However, as shown elsewhere [6,8,44] bias induced band

bending can occur. To avoid such effect, one should decrease V_{ac} once enough sensitivity is achieved. More details including schematic of this method can be found in Chapter 3.

Lift-mode is the most common KFM technique in ambient atmosphere (Fig. 1.10). It realizes the KFM in a double-scan technique. During the first scan the topography is acquired over a given surface line in Tapping™ mode operation where the cantilever is driven mechanically by a piezo actuator. For the second scan, the tip is lifted above the same surface line as in the first scan (typically in the range of 10 nm to 50 nm). The mechanical driving signal at the first resonant peak is turned off and an ac bias at first resonant peak can be superimposed to V_{dc} to realize KFM mapping. Similar to the AM-KFM technique mentioned above, the CPD mapping can be obtained through this scan.

FM-KFM employs an off-resonant frequency AC bias to detect the CPD. In this part, we note the frequency of the modulating signal as f_{mod}. As shown in Eq.(1.23), the contribution of long-range forces is negligible as the cantilever frequency shift depends on the force gradient. In the FM-KFM mode, the applied ac voltage V_{ac} induces a modulation of the electrostatic force. This is detected by an oscillation $\Delta\omega$ of the first angular resonant frequency ω of the cantilever with a frequency f_{mod}:

$$\Delta\omega(f_{\mathrm{mod}},t)=\frac{\partial^2 C}{\partial z^2}(V_{dc}-V_{CPD})\times V_{ac}\sin(2\pi f_{\mathrm{mod}}t)\propto\frac{\partial F_{\omega}}{\partial z}. \qquad \textbf{(1.32)}$$

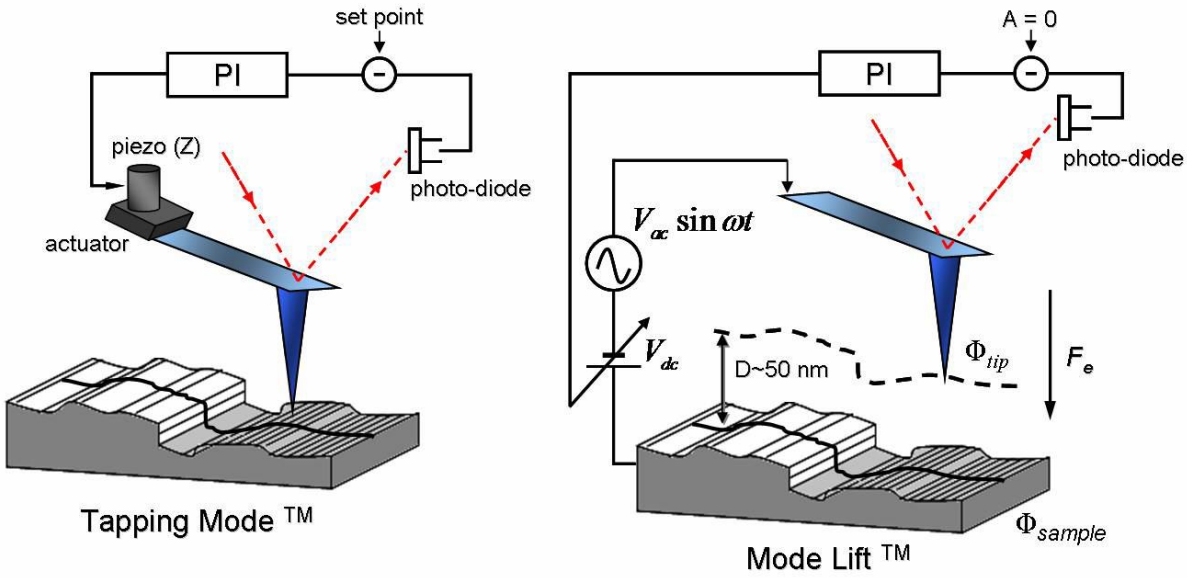

Fig. 1.10 A representative scheme of the two traces principle of the KFM Lift mode. (Details can be found in the text). Figure is adapted from [45].

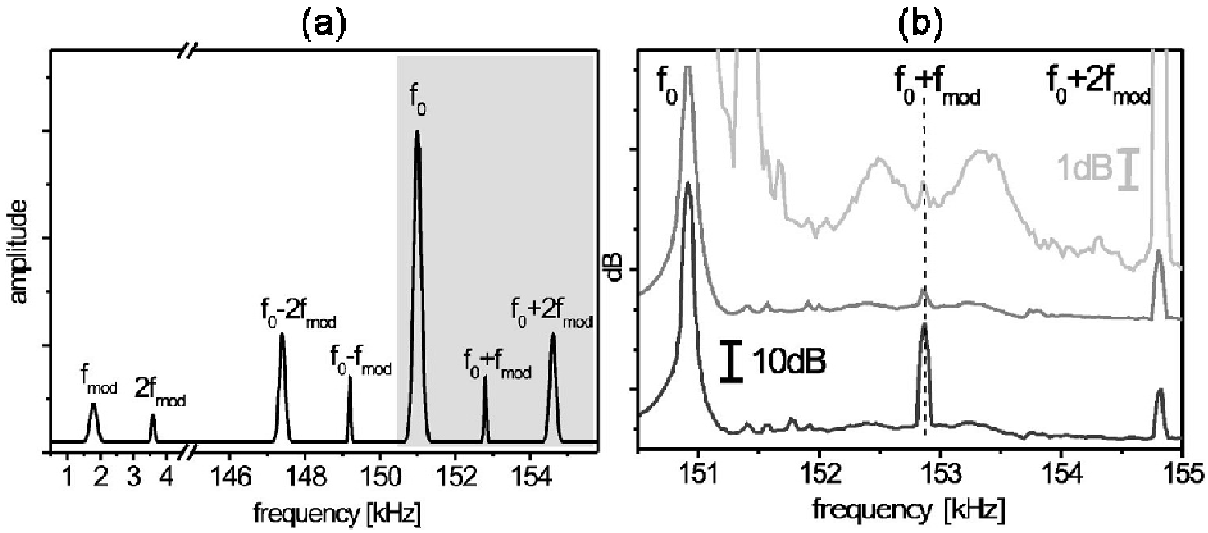

Fig. 1.11 (a) Schematic frequency spectrum of the tip oscillation. The peaks at f_{mod} and $2f_{\mathrm{mod}}$ originate from the electrostatic force, whereas the peaks at $f_0 \pm f_{\mathrm{mod}}$ and $f_0 \pm 2f_{\mathrm{mod}}$ show the frequency modulation of f_0, produced by the oscillating electrostatic force gradient. The experimental spectrum for the gray-shaded frequency range is depicted in (b). (b) Experimental frequency spectra showing the spectral lines at f_0, $f_0 \pm f_{\mathrm{mod}}$, and $f_0 \pm 2f_{\mathrm{mod}}$. The three curves were measured at different bias voltages corresponding to an uncompensated contact potential difference of 1000 mV (black), 50 mV (dark gray), and 5 mV (light gray, y scale 10 times enlarged). Figures are adapted from [46].

By analogy, according to Eq.(1.32) there is also an oscillation $\Delta\omega$ with a frequency of 2fmod which can not be nullified by applying a dc bias. In Fig. 1.11 (a), the sidebands at $f_0 \pm f_{\mathrm{mod}}$ and $f_0 \pm 2f_{\mathrm{mod}}$ are adjacent to the fundamental resonant peak at f_0. In FM-KFM, the side bands at $f_0 \pm f_{\mathrm{mod}}$ are nullified to make V_{dc} equal to V_{CPD}. Experimental data from Zerweck et al. [Fig. 1.11(b)] verified the theory by showing that the spectrum of side bands at $f_0 \pm f_{\mathrm{mod}}$ are significantly reduced as the resulting $V_{dc} - V_{CPD}$ goes low while the $f_0 \pm 2f_{\mathrm{mod}}$ show no change. [46] As shown in Eq.(1.23), such side bands originate from the force gradient $\partial F_{es} / \partial z$. This proves that FM-KFM is sensitive to force gradient instead of force as in the AM-KFM technique.

1.2.2.3 Resolution, contrast and accuracy

The spatial resolution in KFM measurements can be defined as the ability to resolve two adjacent regions, with different electrical properties in the zone of interest, laterally separated by a distance x. This can be represented by the lateral area (diameter d) under the tip where the lines of the electrostatic interaction are concentrated. However,

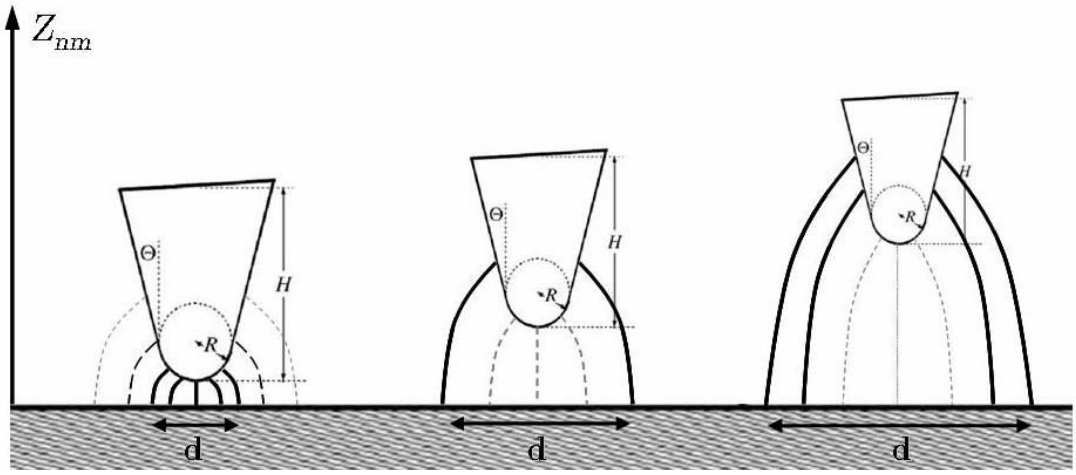

Fig. 1.12 A schematic representation of the enlargement of the electrostatic interaction area under the tip when the distance z between the tip and the sample increases. The cone plays a bigger role for higher separation distances which results in a decrease of the spatial resolution. A better spatial resolution is obtained for small z and slighter tips with small opening angles (θ) and longer cones heights (H). Figure adapted from [45].

the spatial resolution is not only limited by the geometry of the tip but also by the separation distance z between the tip and the sample. These two factors are linked by the widening of the interaction zone under the tip covered by the electric field lines of the electric force (see Fig. 1.12). Moreover, different parts of the tip (i.e. the apex and the cone) become involved in the interaction. These facts result in a decrease of the spatial resolution of KFM measurements.

Kaja. [45] mentioned previous work demonstrated that the spatial resolution varies $\propto \sqrt{Rz}$ for $z < R$ (R being the radius of the tip apex) and $\propto (R + D)$ for $z > D$. However, the evolution of the interacting force as a function of the distance between the tip and the sample has been studied intensively by modeling the geometry of the tip and analyzing the contribution of its different parts to the electric interaction. [43,47,48,49,50] We shall discuss this subject in more details in chapter 2. Therefore spatial resolution can be improved either by minimizing the distance between the tip and the sample (which helps concentrate the interaction between the tip's apex and small region on the surface), either by changing the tip shape in order to improve its sharpness and/or its aspect ratio. Carbon nanotubes, grafted on the tip's apex, represent an important perspective for an improved spatial resolution of KFM electric measurements.

Contrast

Jacobs *et al.* modeled the capacitance influence from the different patches on the sample surface (see Fig. 1.13). [49] The equation of electrostatic force at ω_{el} can be written:

$$F_{\omega_{el}} = -\sum_{i=1}^{n} \frac{\partial C_{it}}{\partial z}(V_{CPDi} - V_{dc})V_{ac}\,, \tag{1.33}$$

where $\frac{\partial C_{it}}{\partial z}$ is the derivative of the mutual capacitance between the tip and the sample . This shows that the $F_{\omega_{el}}$ is the integration of different patches which widely exist in the real surface. The simple capacitor model does not consider the Coulomb interaction of trapped charges and their mirror charges in the conductive tip [51] and semiconducting materials [52] or the presence of stray electric fields. [53,54] Such effects can potentially reduce the CPD contrast.

In AM-KFM mode, as it is sensitive to long rang electrostatic forces, not only the apex but also the cone and even the cantilever can be involved in such contribution. This was shown by Gil *et al.,* [43] where a flat sample surface is assumed. The contributions of the macroscopic cantilever and mesoscopic tip cone as well as the nanometric tip apex are taken into account. The authors show the cantilever plays a greater contribution in electrostatic force when the tip-sample separation exceeds few nanometers (typically 5 nm). However, in the same situation, the tip apex dominates the electrostatic force gradient when the tip-sample distance is less than 20 nm. The effect of cantilever only produces a limited contribution even when the tip-sample distance is up to 10 µm. To the contrary, this distance dependence property is not obvious in the FM-KFM images as it is

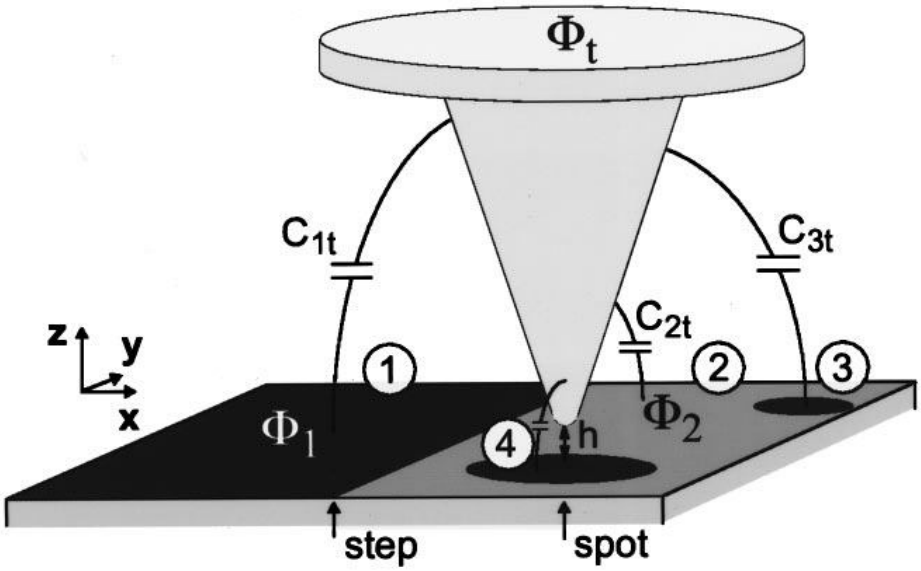

Fig. 1.13 Model of the KFM setup: System of ideal conductors with electrostatic interactions represented by mutual capacitances C_{ij} . [49]

sensitive to the force gradient instead. Fig. 1.9 shows that the force gradient decreases much faster than the electrostatic force and is less influenced by electrostatic coupling from the cone and the cantilever. [42]

Distance dependence

Different groups [53,55,56] reported the distance dependence of CPD. In reality, due to the anisotropic [57,58] properties and different dipole layers [4] of sample surface, electric field [55] exists between "different patches". Therefore, to estimate this surface Coulomb contribution, Eq. (1.27) can be written [53,56]:

$$F_{\text{es}} = -\frac{1}{2}\frac{\partial C}{\partial z}[(V_{dc} - V_{CPD}) + V_{ac}\sin(\omega_{el}t)]^2 + Q_{tip}E_s\,, \tag{1.34}$$

where $Q_{tip} = CV_{ac}$ is the charge on the tip and E_s is the surface electric field between different patches. In Kelvin probe, the ω_{el} term of F_{es} is nullified. We can have F_{ω} :

$$F_{\omega_{el}} = \frac{1}{2}\frac{\partial C}{\partial z}(V_{dc} - V_{CPD})V_{ac} + CV_{ac}E_s\,. \tag{1.35}$$

When Kelvin controller is on ($F_{\omega} = 0$), we have:

$$V_{dc} = V_{CPD} + g(z)E_s\,, \tag{1.36}$$

where $g(z)$ is a geometric factor depending on the mutual capacitance and the separation distance between the tip and the sample:

$$g(z) = 2\frac{C}{\partial C / \partial z}\,. \tag{1.37}$$

According to Eq. (1.37), the V_{dc} value measured in KFM is therefore dependent on:

i) the variation of the mutual tip-sample capacitance C, defined by the geometric factor $g(z)$, with respect to the tip-sample z, distance.

ii) the dependency z of the electric field E_s, induced by the surface Coulomb contribution.

These two facts are actually linked by the variation of the effective area of the electrostatic interaction between the tip and the sample with respect to their separation distance.

Chapter 2

Comparative analysis of KFM acquisition modes in air

After 20 years of development, Kelvin probe force microscopy (KFM), which was invented by Nonnenmacher *et al.* in 1991, [38] has become more and more useful for the characterization of the electrical properties of novel materials and nanostructures at the nanoscale. This technique is available under various conditions such as ultrahigh vacuum, ambient atmosphere and even in liquids. [59,60,61] Several authors have reported KFM mapping showing variations of the CPD at atomic scale on semiconductors and insulators. [30,62] Many variants of KFM measurements exist and have been discussed in various papers or chapters of books. [63,64] However, despite different working environments, two operational modes are possible to probe the electrostatic interaction. [42,65,66] The first mode, named amplitude modulation (AM), is based on the force sensitive detection. [42] The second mode, named frequency modulation (FM), uses a force gradient sensitive detection. [46,67] In the FM mode, due to the detection of the force gradient, the tip apex contributes mainly to the measured signal, while a much stronger influence of the probe shape is expected for AM detection, resulting in a reduction of the contrast in the measured contact potential difference images. It is worth noticing that this difference appears to be essential for the optimization of KFM imaging.

Most conventional ambient KFM measurements are performed using the Lift-mode: a double-scan [53,55,56] technique in which the surface topography is firstly acquired using the intermittent contact mode (Tapping™) and then the CPD is independently measured at a constant tip-sample lift height. [53,68] The spatial resolution in the Lift-mode is dramatically improved as the lift height corresponding to the tip-sample distance is reduced. [69,70] However, simultaneous acquisition of the topography and of the CPD can be realized in single-scan (SS) method, which is based in the simultaneous use of two cantilever flexural resonant frequencies.

In this chapter, we propose to compare experimentally the spatial resolution as well as the contrast obtained with both methods (single scan and Lift-mode) and both modes (AM and FM) for different tip-sample separations. Moreover, the effects of different experimental parameters will also be discussed to understand the influence on KFM results.

2.1 Resolution and contrast: Lift and single scan comparison

2.1.1 Principle of each technique

The KFM technique discriminates electrostatic forces from van der Waals forces by applying an ac voltage between the tip and the sample and by adjusting a static dc component to nullify the electrostatic interaction. Under UHV, the KFM can be operated in a single scan which measures simultaneously both the topography in non-contact mode and CPD. [42] In this case, two types of KFM measurements are possible: one based on the amplitude modulation (AM) and the other one based on the frequency modulation (FM). [71]

The AM-KFM is based on electrostatic force sensitive detection. In order to separate the impact of topography and the CPD in single scan mode, the excitation angular frequency ω_{el} of the ac tip-sample bias is commonly set to the second flexural eigenmode of the cantilever while the first eigenmode is used to acquire the topography. The resulting oscillation amplitude induced by the electrostatic force is detected by a quadrant photodetector and then demodulated (see green dashed line in Fig. 2.1) by a lock-in amplifier at angular frequency ω_{el}. The resulting amplitude is proportional to the electrostatic force:

$$F_{\omega} = -\frac{\partial C}{\partial z}(V_{dc} - V_{cpd})V_{ac}\sin(\omega_{el}t), \qquad (2.1)$$

where $\frac{\partial C}{\partial z}$ is the derivative of the probe-sample capacitance with respect to the distance z. The Kelvin controller adjusts in real time the bias V_{dc} in order to nullify the tip-sample electrostatic force. As shown by Eq. (2.1), the condition $F_{\omega} = 0$ is fulfilled when $V_{dc} = V_{cpd}$.

The FM-KFM is based on sensitive detection to the force gradient. In this mode, the excitation angular frequency ω_{el} ranges between several hundred and a few thousand hertz. This method is based on the fact that the induced oscillating electrostatic force gradient leads to a modulation of the fundamental resonant frequency ω_0 of the

cantilever, giving rise to a sideband at $\omega_0 + \omega_{el}$. [46,72] Demodulation by a lock-in amplifier of the mechanical phase (see purple dashed line in Fig. 2.1) at ω_{el} angular frequency delivers a signal proportional to the electrostatic force gradient given by the relation:

$$\frac{\partial F_{\omega_{el}}}{\partial z} = \frac{\partial^2 C}{\partial z^2}(V_{dc} - V_{cpd})V_{ac}\sin(\omega_{el}t), \qquad (2.2)$$

where $\frac{\partial^2 C}{\partial z^2}$ is the second derivative of the probe-sample capacitance with respect to the distance z. In contrast with AM-KFM mode which nullifies the oscillation amplitude, the FM-KFM nullifies the mechanical phase, measured at ω_{el}, by adjusting the V_{dc} voltage via the Kelvin controller. In practice, the *X* output of the second lock-in is minimized by Kelvin controller to fulfill the condition: $V_{dc} = V_{CPD}$. The *X* component is always used due to the monotonic variation with the V_{dc} bias[3]. In Fig. 2.1, the components in orange are part of Nanonis electronic while the "blue" components are part of Dimension 3100 (Bruker,

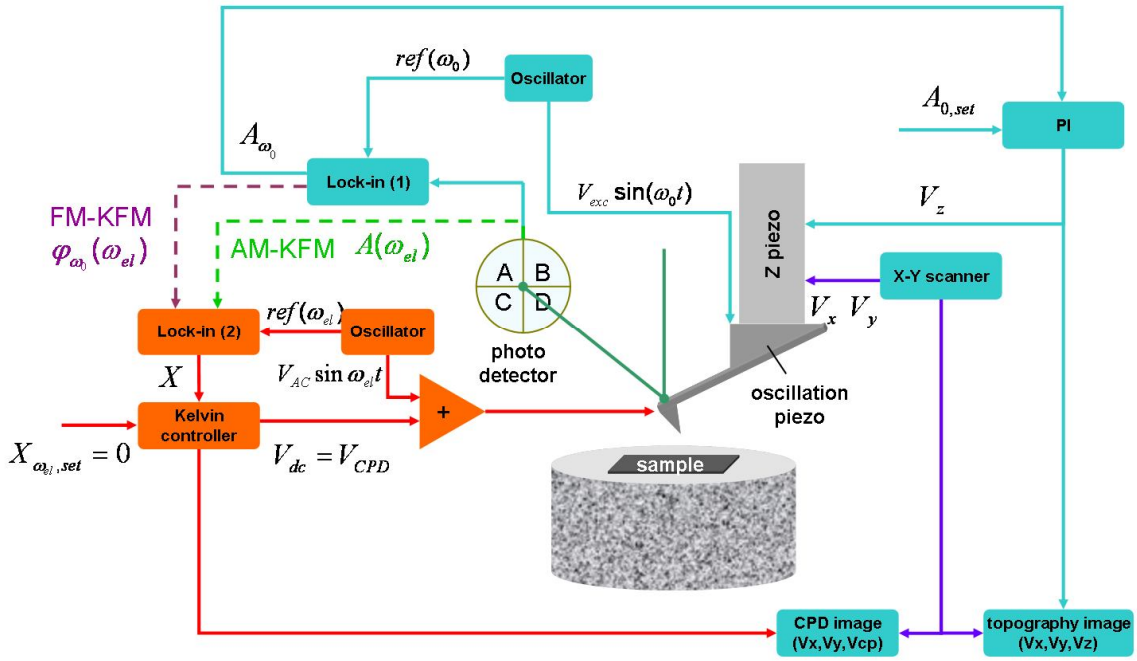

Fig. 2.1 The schematic setup of AM- and FM-KFM with the main electronic components. The blue lines represent the topography loop, while the red one corresponds to the CPD measurement. The violet lines are the common wires for both topography acquired in Tapping™ mode and electric loop.

[3] This part is presented and discussed in section 2.2.3.

USA) or MultiMode (Bruker, USA). When operated under UHV, a phase locked loop (PLL) [46,67,73] measures the real-time frequency shift of the cantilever which is then used for KFM measurements in FM mode. However, in this chapter all the results are obtained in Tapping™mode, and therefore the FM-KFM technique is performed by demodulating the mechanical phase.

2.1.2 Effect of the tip-sample distance

According to Eqs. (2.1) and (2.2), the ω_{el} component of the electrostatic force or gradient force is nullified when V_{dc} equals the CPD whatever the tip-sample separation is. However, experimental observations of the tip-sample distance dependence of the CPD have been reported on various kinds of samples and under various environmental conditions. [53,56,74] In fact, the measured V_{dc} voltage does not exactly match the CPD of a given location as it is a weighted average of all the local surface potentials below the tip apex. The weighting factor depends on the tip-sample capacitance gradient and so on the location of the tip on the sample surface. As presented by Jacobs *et al.*[49], the KFM technique can be modeled as a sample surface composed of n ideally conducting electrodes of constant potential V_i. In this case, the V_{dc} voltage applied to the tip in force sensitive detection mode can be written as:

$$V_{dc} = \frac{\sum_{i=1}^{n} \frac{\partial C_i}{\partial z}\Big|_{z_0} V_i}{\sum_{i=1}^{n} \frac{\partial C_i}{\partial z}\Big|_{z_0}}, \qquad (2.3)$$

where $\frac{\partial C_i}{\partial z}$ is the derivative of the capacitance between the tip and the location i on the sample at a distance z_0 from the sample surface. In the case of a force gradient sensitive detection, the same calculation leads to:

$$V_{dc} = \frac{\sum_{i=1}^{n} \frac{\partial^2 C_i}{\partial z^2}\Big|_{z_0} V_i}{\sum_{i=1}^{n} \frac{\partial^2 C_i}{\partial z^2}\Big|_{z_0}}, \qquad (2.4)$$

where $\frac{\partial^2 C_i}{\partial z^2}$ is the second derivative of capacitance between the tip and the area i on the sample located at a distance z_0 from the sample surface. Both Eqs. (2.3) and (2.4) demonstrate that the resolution and the accuracy in KFM are defined by the electrostatic

coupling between the tip and the different surface regions. It is worth noticing that, as in the force gradient sensitive detection, the electrostatic coupling from the cone and the cantilever of the tip is negligible compared to the force sensitive detection resulting in better CPD contrast and better spatial resolution.

2.1.3 Instrumental description

Dimension 3100 and Multi-Mode AFMs from Bruker

The Dimension 3100 AFM is an instrument capable of imaging specimens with a horizontal and vertical resolution down to the nanoscale at ambient pressure in air. Pictures of this AFM and of the tip holder for electrical measurements are shown in Fig. 2.2. Typically, the signal-to-noise ratio for topography measurements is equal to approximately 0.3 nm to 0.4 nm. The Dimension 3100 uses standard and advanced SPM imaging modes for measuring semiconductor wafers, lithography masks, magnetic media, biomaterials, optics and other materials. The sample stage allows large sample (up to a 150 mm wafer) to be analysed with a scan size up to 90 µm in the x and y axis and 6 µm in the z axis.

The MultiMode AFM has a high-resolution, low noise scanner (rms noise for topography measurements typically is around 0.1 to 0.2 nm). Pictures of this AFM and of the tip holder for electrical measurements are shown in Fig. 2.3. The maximum size of the samples which can be analyzed is approximately one square centimeter. This instrument has approximately one angstrom vertical resolution. Compared to the Dimension 3100, the Multimode is more compact and so is more resistant to thermal drift and more immune to mechanical vibration.

Vibration isolation system

Both the Multi-Mode and the Dimension 3100 systems are equipped with vibration

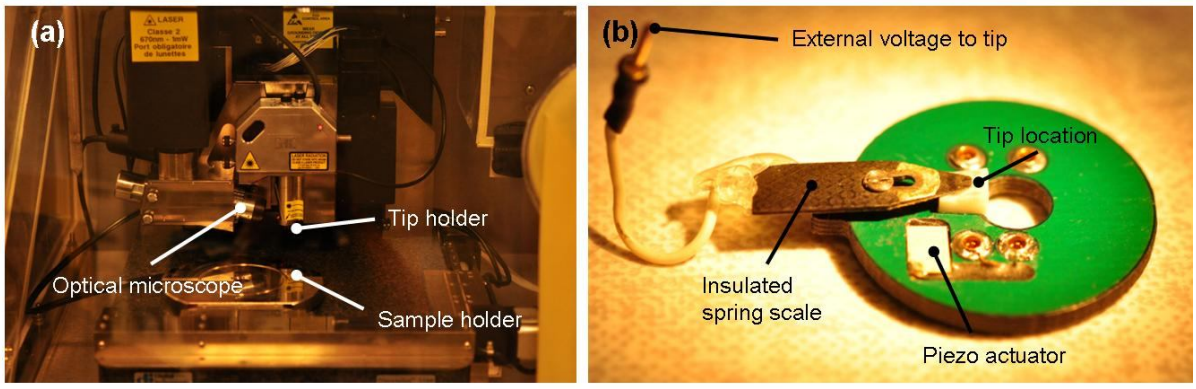

Fig. 2.2 (a) Dimension 3100 Microscope. (b) SSRM tip holder which allows an external voltage to be applied to the tip and to avoid the crosstalk from the all-in-one cable of the microscope.

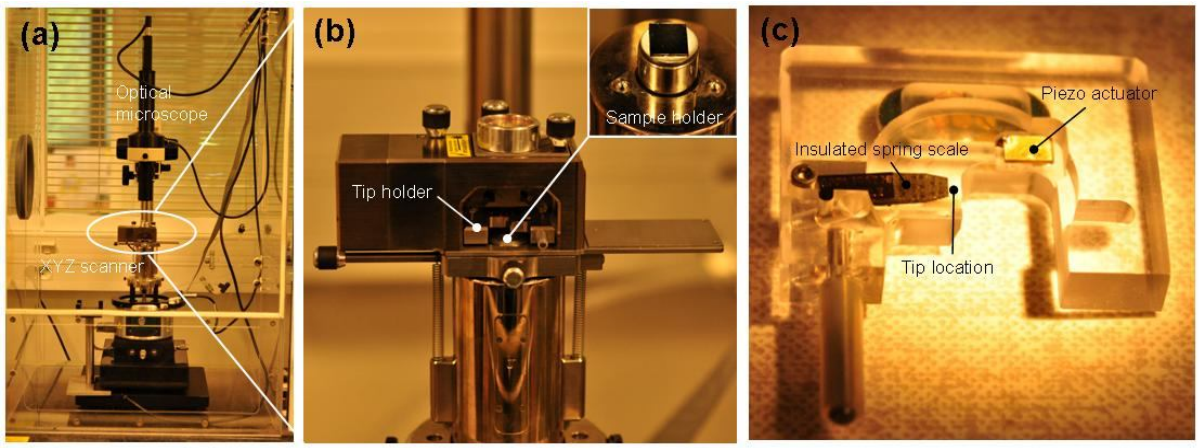

Fig. 2.3 (a) Overview of the MultiMode microscope. (b) Microscope head (upper inset is uncovered sample holder) (c) Insulated tip holder used for conductive measurements.

isolation systems. External parasitic perturbations come from acoustic and terrestrial vibrations. Acoustic vibrations are limited by using a box which can cover the whole microscope system. And the terrestrial vibrations are minimized by a damping system consisting of a marble platform with polymeric gel on top, supported by an air cushion structure.

Nanonis Dual-OC4 system

The Oscillation Controller (OC4) from Nanonis is used externally as a standalone version to perform KFM measurement both in AM and FM modes [see Fig. 2.4(a)]. It is in fact an "open"electronic having a lock-in amplifier, proportional-integral (PI) controllers and filters. With an analog bandwidth of 5 MHz, this electronic is well suited to operating at higher resonant modes without loss of signal quality. It performs the same functions as a high performance oscilloscope and a spectrum analyzer. The built-in demodulator even makes zoom-FFT possible, allowing quantitative thermal noise analysis and calibration of spring constant or amplitude.

Signal Access Module (SAM)

To connect the external electronics to the microscope, an access to different signals is needed. The SAM is a box connected between the AFM microscope and the AFM controller [see Fig. 2.4(b)], giving access to different signals such as the photodiode raw signal (INO output) or the mechanical phase signal (AUXB output), which are the two signals needed for KFM measurement. Although external signals such as ac and dc signals could be sent to the tip via the SAM box. However, in practice, due to a high level of noise introduced by crosstalk in SAM box, such signals are directly connected to the tip.

Tip holder for external electrical connection

When operating a Dimension 3100 AFM, a DTRCH-AM tip holder shown in Fig. 2.2(b) is currently used to connect the tip with the external electrical signal to avoid the noise

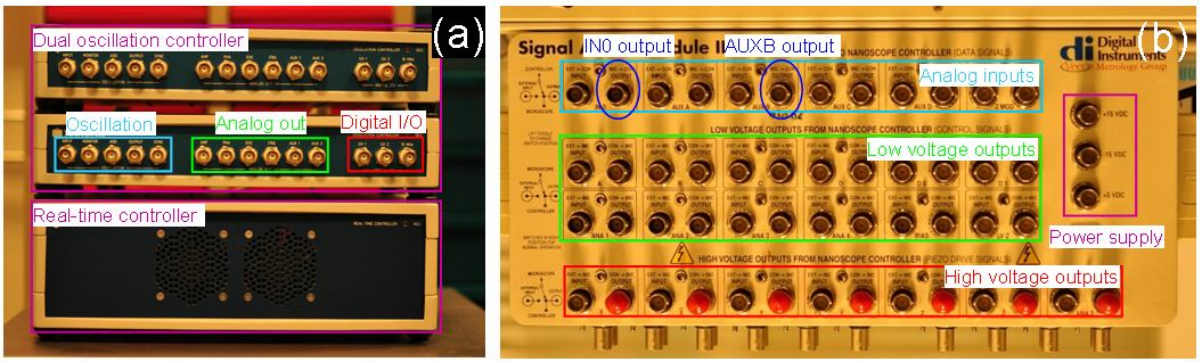

Fig. 2.4 (a) Nanonis Dual OC4 system. (b) Bruker Signal Access Module III (IN0 and AUXB outputs are indicated).

induced by the SAM box. In the same way, a MMTR-TUNA-CH tip holder is used on the MultiMode [Fig. 2.3(c)]. A homemade aluminum box (not shown here) can be fixed on the microscope head to connect the wires and avoid vibration induced by the connecting cables.

Schematic of connections

The original AFM (MultiMode or D3100) is used for the topography measurements while the Nanonis dual-OC4 only controls the KFM measurement. Electrical connections to do AM or FM-KFM are described in Fig. 2.5 and hereafter:

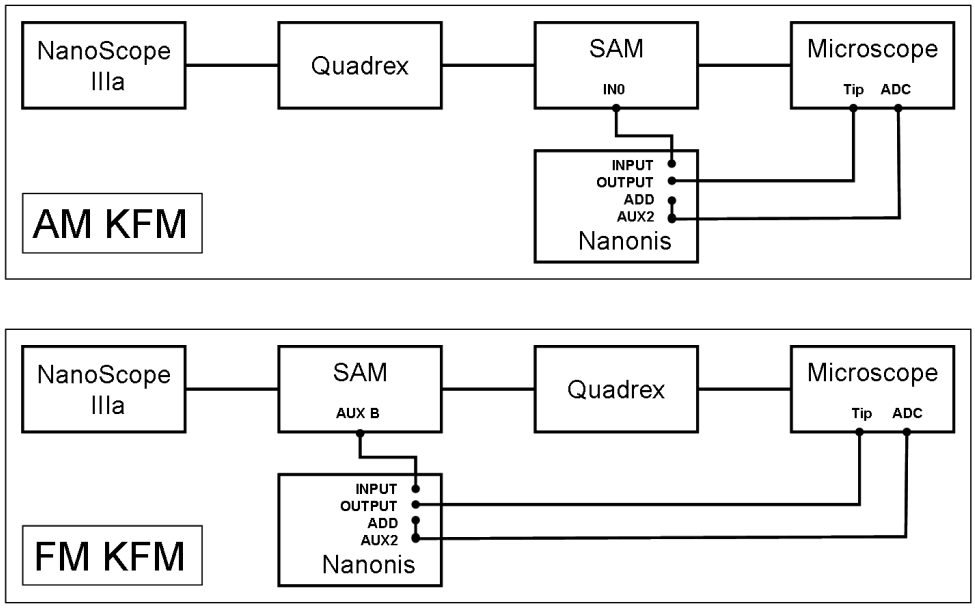

Fig. 2.5 Schematic of system connections. In the FM-KFM mode, the SAM box is connected between the Nanoscope IIIa controller and the Quadrex to extract the mechanical phase signal (AUXB output), while in the AM-KFM mode, the SAM box is placed between the Quadrex and the AFM to extract the photodetector signal (IN0 output). In both modes, the V_{dc} signal (AUX2) is summed with the signal $V_{ac}\sin\omega_{el}t$ via the ADD input and is sent to the tip via the OUTPUT. The V_{dc} signal (AUX2) is also sent to an ADC of Nanoscope IIIa controller in order to be simultaneously imaged with the topography.

i. In AM-KFM mode, the IN0 output from the SAM box corresponding to the photodetector raw signal is connected to the Nanonis "INPUT" in order to extract the ω_{el} component of the electrical force. The OC4 system extracts the ω_{el} component of the photodetector raw signal and the V_{dc} bias is adjusted to nullify it. The AUX2 output signal from Nanonis corresponding to the V_{dc} is fed to the ADD input in order to be summed with the $V_{ac}\sin(\omega_{el}t)$ signal and is applied to the tip via the tip holder (as mentioned above). In parallel, the V_{dc} also goes to the ADC input of the microscope controller to map the KFM image.

ii. The connections needed for FM-KFM mode are similar to the ones used for AM mode. However, the AUXB output of the SAM box corresponding to the mechanical phase is used as signal to extract the ω_{el} component of the electrical force gradient. The OC4 system extracts the ω_{el} component of the photodetector raw signal and the V_{dc} bias is adjusted to nullify it.

2.1.4 Experimental settings

In this chapter, we propose to compare experimentally the spatial resolution as well as the contrast obtained in KFM for three modes: AM-KFM in Lift-mode, AM-KFM in single scan and FM-KFM in single scan. The impact of the tip-sample separation will be also studied. An overview of each mode is presented hereafter:

1) In Lift-mode, an ac voltage with a peak-to-peak voltage ranging from 2 V to 10 V and a frequency equal to the one of the mechanical fundamental resonance (typically, around 70 kHz) is applied to the tip. During a first scan, the topographic height $h(y)$ is acquired using the Tapping™ mode. During the second scan, the KFM mode is activated. In this mode, to minimize the van der Waals interaction, the tip is moved away from the surface by applying a lift height h_0. Then, during the second scan the z-piezo imposes the height to equal $h_0 + h(y)$ or $h_0 + \langle h(y) \rangle$.

2) In single-scan AM-KFM, the CPD is measured by applying to the tip an ac voltage with a peak-to-peak value ranging from 1 V to 4 V and a frequency equal to the first harmonic of the mechanical resonance and nullifying the resulting mechanical oscillation by adjusting the V_{dc} tip bias. The topography is determined simultaneously in Tapping™ mode at the fundamental resonant frequency.

3) In single-scan FM-KFM, a higher ac voltage ranging from 2 V to 6 V is applied to the tip with an off-resonant frequency (typically between 500 Hz and 4 kHz). In contrast with the previous two methods, the mechanical phase instead of the electrical amplitude is used to access to the electrostatic force gradient, and so to measure the CPD. Therefore, a sensitive detection to the force gradient is expected. The topography is measured simultaneously in Tapping™ mode.

The resulting experimental settings are listed in Table 2.1.

Table 2.1 Main parameters of three common KFM techniques

	AM-KFM		FM-KFM
	Double-scan (Lift Mode)	Single-scan	Single-scan
Lift height	10-30nm	No	No
Mechanical oscillation	No	Yes	Yes
Amplitude of AC oscillation	2-10V	1-4V	2-6V
Frequency of AC oscillation	1st eigenmode (70KHz)	2nd eigenmode (440kHz)	off-resonance (0,5-4kHz)
Sensitive to	Force	Force	Force gradient
Tip	Conductive tip (Cr/Pt coating tip - Multi75E-G)		

Evaluation of the tip-sample separation

For reasons linked to the quality factor, the fundamental resonant frequency is commonly used to perform Tapping™ experiments. [75,76,77] The mechanical amplitude is closely related to the tip-sample separation. However, in order to convert the photodetector signal from volt to nanometer a calibration is required. To do so, while oscillating, the tip approaches an ideally not deformable sample [see Fig. 2.6(a)]. During this process the rms amplitude A of the mechanical oscillation ideally undergoes a linear decrease with a slope $\frac{dA}{dz} = -1$. Usually, this calibration is done with a silicon tip and a SiC sample (Young modulus $E = 450$ GPa). The driven frequency of the cantilever is set to 70 kHz with an amplitude of 80 nm. The method can be split in three stages:

i. In the stage 1, the tip is driven in oscillation at its free resonant frequency with maximum amplitude as no interaction force acts on the tip.

ii. While approaching the sample surface, the tip oscillation is more and more affected by the van der Waals force and, as a consequence, the oscillating amplitude of the cantilever keeps decreasing. If we assume that the deformation of tip and of the sample is negligible, it can be shown [78] that the decrease ΔA of the amplitude is equal to the Z-piezo extension increase Δz. In other words, the absolute value of the slope $\frac{\Delta A}{\Delta z}$ is equal to unity. Since the amplitude is measured in volts and the z-piezo extension is known, the calibration coefficient can be calculated using the linear part of the approach-retract curve. Using six different approach-retract curves we obtain a calibration coefficient equal to 26 nm/V with relative error of approximately 0.2 %.

iii. As the z-piezo keeps approaching the surface, the tip will finally jumps on the sample surface and stop oscillating.

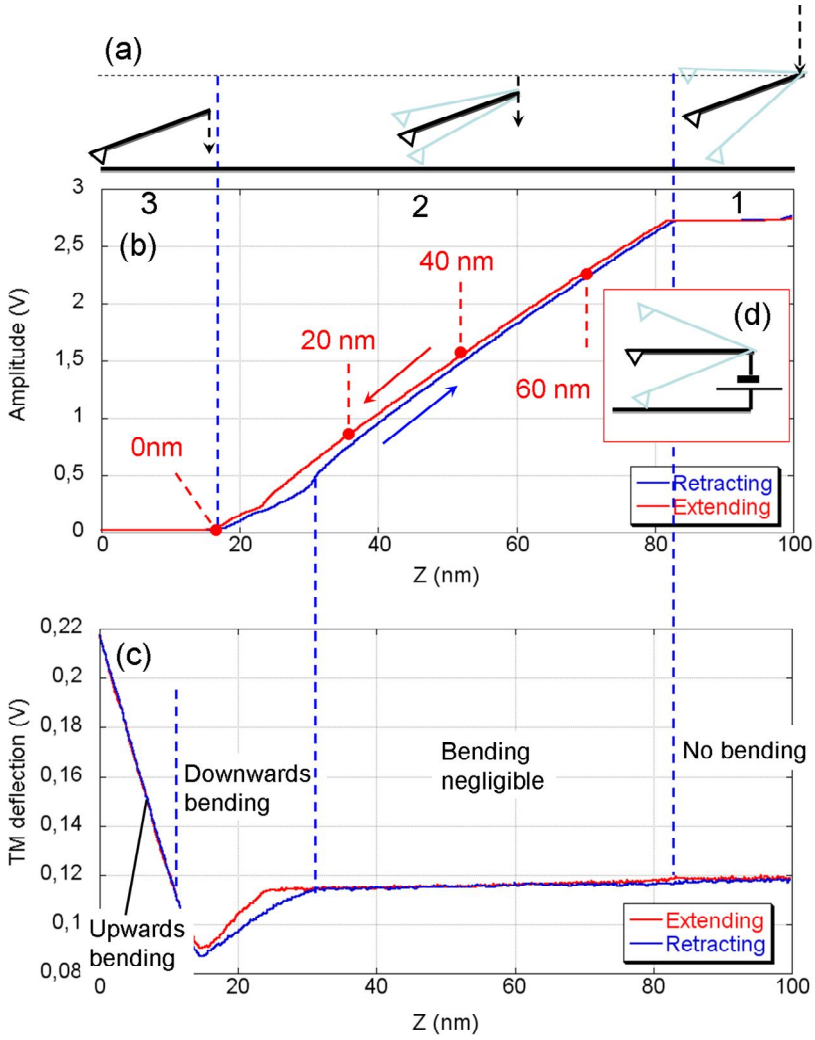

Fig. 2.6 (a) Schematic of an oscillating cantilever condition while approaching to a sample surface. (Detailed description of the 3 stages can be found in the text) (b) Amplitude evolution of (a). Since the Z piezo extending distance is known as well as the contact point (as indicated as "0nm") we can define the tip-sample separation by setting different amplitude setpoint. (c) Average TM deflection of the cantilever indicating three force regions. Not like the static force calibration curve, the "jump to contact" part and the "pull out" part are not obvious due to the oscillation.(d) Schematic of tapping tip.

We can also observe that the approach and the retract curves are not superimposed but are shifted [see Fig. 2.6(b)]. This shift is due to the hysteretic behavior of the Z-piezo, which exhibits a slight extension difference for the same applied bias during respectively the approach and the move away phases.

2.1.5 Tip and sample description

In this chapter, Pt/Ir coated silicon tips from "Budget Sensors" (Sofia, Bulgaria) are used. A thin Chromium adhesive layer is deposited between the silicon and the Pt/Ir coating. [79] The stiffness of tips is 3 N/m and the free resonant frequency of the cantilever is about 75 kHz.

To minimize the topographic artifacts, a flat sample with CPD contrast is needed. Epitaxial graphene on SiC(0001) suits this need as this sample has a very flat surface. The height of the steps between two terraces lies in the range of 1 nm to 2 nm. But the work function of a stack of few graphene layers (FLG) increases by approximately 100 meV for each additional layer. [80,81]

The SiC substrate, purchased from "Novasic", is n-doped (nitrogen) and the doping concentration is approximately $(2.5\pm0.5)x10^{17}$ cm^{-3}. The double-sided polished substrate is introduced in an induction furnace operating under UHV. Three heating stages have been applied. First, the sample is heated, at a temperature ranging between 200 °C and 300 °C, to clean and outgas the surface. Then, the sample is baked at a temperature of about 800° C for several hours and then at a temperature of 1400 °C (with vacuum down to 10^{-8} mbar) during 5 hours. Temperature ramps (up and down) are set to 50 °C/min. The growth of graphene layers is therefore achieved by solid state graphitization where Si atoms desorb at high temperature (approximately 1150 °C) and carbon in excess results in graphene layers. [82]

2.1.6 **Experimental results**

2.1.6.1 KFM with Multi-Mode AFM

Fig. 2.7(a) and (b) show respectively the topography and the CPD mapping of an epitaxial graphene on SiC (0001) substrate. The green line indicates the abrupt surface topography change of this sample but no CPD change is detected. This means that the obvious topography steps is induced by the SiC substrate but the number of graphene layer is the same. Another line in red shows the inverse situation, the CPD changed on the SiC terrace but no topography step is detected. This means that a new graphene layer starts to form on the same terrace of SiC. Although the graphene step is 0.33 nm [83] the height difference between 1 and 2 monolayers (ML) can be only 0.07 nm due to a 0.25 nm SiC layer step. [80] Line profiles at the indicated red line in Fig. 2.7(c) shows a CPD difference of 0.15 V with no obvious topography step. The histogram shown in Fig. 2.7(a) of the CPD mapping exhibits three peaks clearly belonging to three different stacks of graphene monolayers.

In order to evaluate the number of graphene layers present on this sample, filtered ultraviolet photoemission electron microscopy (UV-PEEM) has been used to characterize epitaxial graphene layers on SiC. To remove organic contamination, the sample is heated at 480 °C for 20 min under UHV. Then UV-PEEM analysis is done using a helium discharge lamp (He1 =21.2 eV) as excitation source. A series of images, for different photoelectron energy, are acquired in PEEM filter mode and then data processed to obtain a mapping of the surface work function.

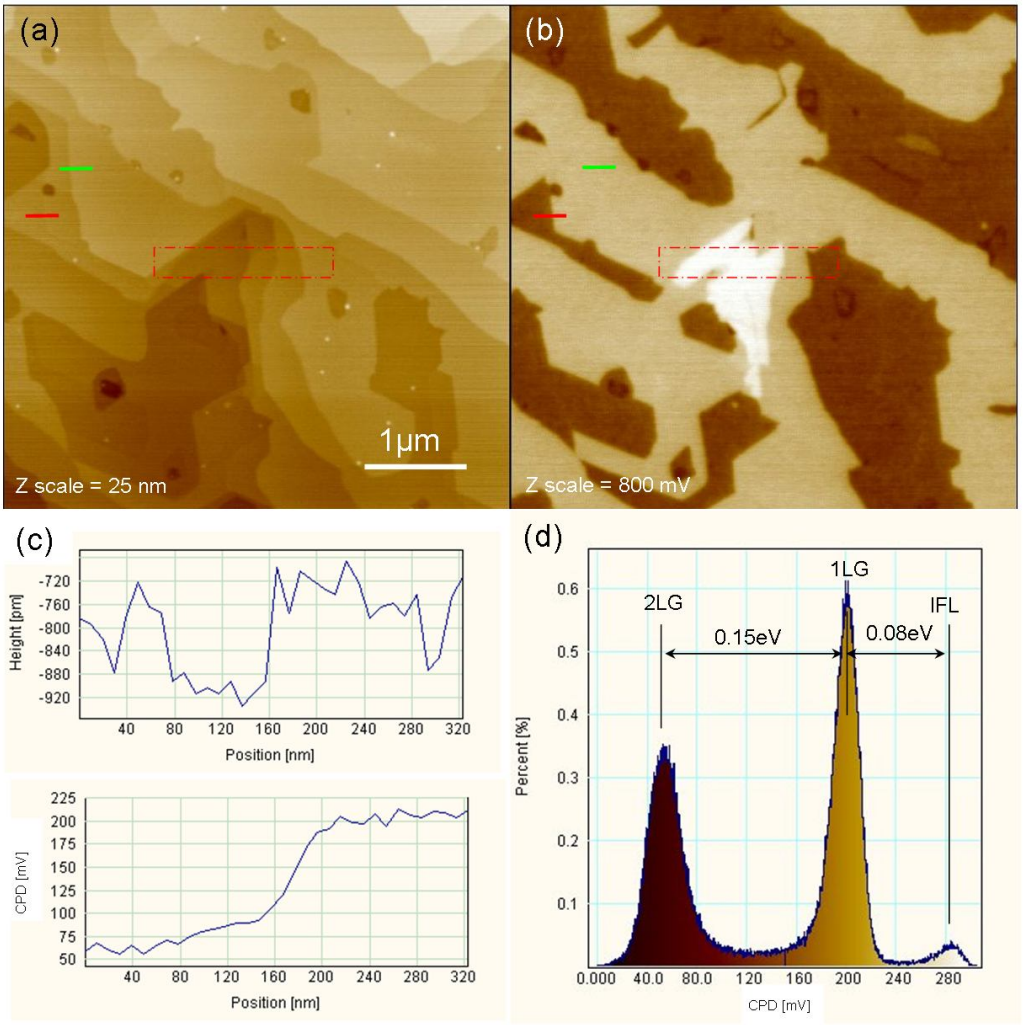

Fig. 2.7 Topography (a) and CPD (b) by AM-KFM in single scan of epitaxial graphene layers on SiC (0001). As indicated in the green line, the CPD has no change where an obvious topography step occurs. This step is due to the steps of the SiC substrate. Further zoom-in scan is indicated by the red box. (c) Line profiles at the red line respectively on topography and CPD. A 0.15 V CPD is visible between the dark and bright region. (d) Histogram of the CPD image. The work function difference between 1 ML and 2 ML is equal to 0.15 eV.

The work function mapping of our sample is presented in Fig. 2.8(a). The resulting histogram [Fig. 2.8(b)] shows that the work function value ranges from 4.20 eV to 4.46 eV, which corresponds to the presence of 0 ML,[4] 1 ML and 2 ML of graphene. Indeed, Hibino *et al.* have performed similar studies by PEEM technique and have shown that the work function of 0 ML, 1 ML, 2 ML and 3 ML is respectively equal to 4.18 eV, 4.33 eV, 4.4 eV and 4.52 eV [see Fig. 2.8(c)]. [84]

[4] No monolayer of graphene (O ML) corresponds to the carbon-rich interface layer between the SiC bare substrate and the first monolayer.

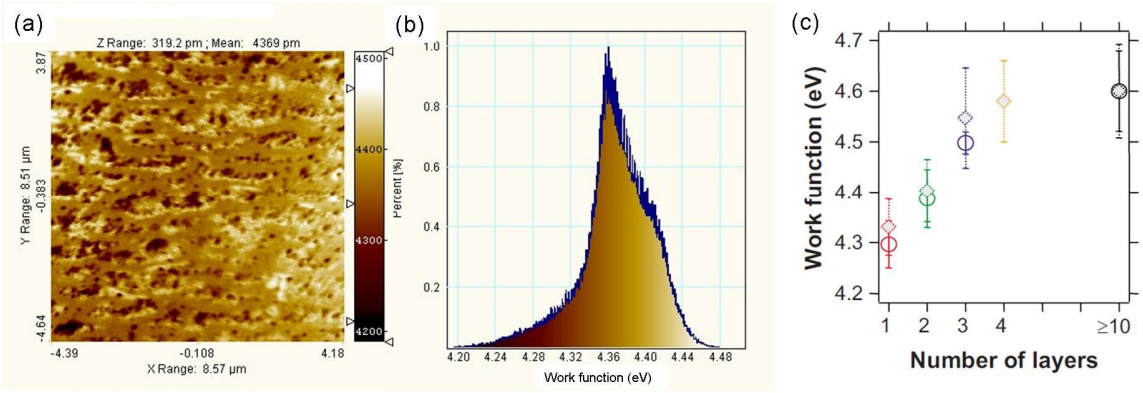

Fig. 2.8 (a) Quantitative work function mapping by filtered PEEM on epitaxial graphene on SiC. The exposition time is 5 min. And He-1 is used as excitation source. (b) Histogram of (a) shows the work function mainly distributed from 4.20 eV to 4.46 eV. (c) Work functions of 1 ML, 2 ML and 3 ML distributed narrowly at 4.32 eV, 4.4 eV and 4.5 eV measured by Hibino *et al.* [84]

This means that only a maximum of 2 ML of graphene has grown on our sample following this fabrication condition. Therefore, the three peaks found on the surface potential histogram in Fig. 2.7(d) are 0 ML, 1 ML and 2 ML. In KFM, V_{dc} compensates the potential differences between the tip and the sample, and if the tip work function Φ_t is known, the work function of the sample is given by the relationship $\Phi_s = \Phi_t - eV_{dc}$. The local variation of the work function, however, can be expressed independently of Φ_t using $\Delta\Phi_s = -e\Delta V_{dc}$. Therefore, with our optimized KFM under ambient atmosphere, the work function difference between 2 ML and 1 ML $\Delta\Phi_s^{(2-1)} = -e\Delta V_{dc}^{(2-1)} = 0.15$ eV is in quantitative agreement with those obtained using KFM under UHV [80].

Spatial resolution and contrast

Fig. 2.9 shows three series of CPD images obtained on the same area of a graphene sample [see the red box in Fig. 2.7(b)] by using three KFM acquisition modes. The tip-sample distance ranges between 80 nm and 3 nm. For the sake of clarity, all the images are presented with the same potential scale of 500 mV. In Lift-mode [Fig. 2.9(a)], blurred images of graphene layers are obtained for a large tip-sample separation and the contrast is strongly improved when this separation is reduced. For both AM and FM modes in single scan (SS), the tip-sample distance has less influence on the contrast, even if FM-KFM mode seems to give a better contrast [Fig. 2.9(c)], confirming that a detection sensitive to the force gradient is less affected by the tip cone and by the cantilever. [66]

Fig. 2.10(a) shows the surface potential contrast value with respect to the tip-sample distance for each acquisition mode. A slight increase of the contrast is observed for both Lift- and single scan-AM modes when the probe is close to sample surface. In FM-

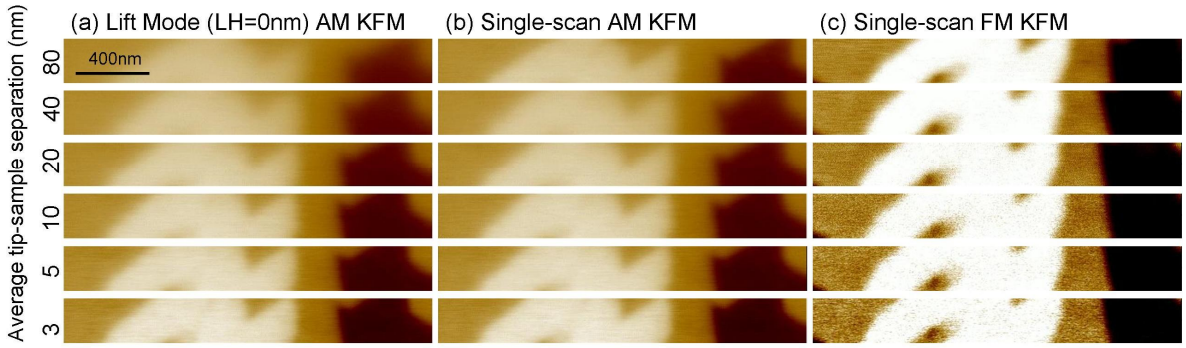

Fig. 2.9 CPD images in the zoomed area in Fig. 2.7 with Lift mode-AM, single scan-AM and single scan-FM KFM techniques in function of the tip-sample separation. Experiments are done with Multi-Mode AFM. The CPD scale is 500 mV for all the images. (a) AM-KFM in Lift-mode shows strong dependence with the tip-sample separation. (V_{ac}= 4 V, f_{elec}= f_0 = 67 kHz, scan rate= 0.1 Hz and lift height of 0 nm). (b) Single-scan AM-KFM shows less dependence on tip-sample separation but with lower contrast than (c). (V_{ac}= 4 V, f_0 = 67 kHz, f_{elec}= 429 kHz, scan rate= 0.1 Hz). (c) Single-scan FM-KFM exhibits the highest contrast and low dependence on tip-sample separation. (V_{ac}= 4 V, f_0 = 67 kHz, f_{elec}= 400 Hz, scan rate= 0.1 Hz).

KFM mode, the contrast is two times higher than the one obtained in AM-KFM. Furthermore, the FM-KFM contrast is independent of the tip-sample distance, which is in agreement with the results shown in Fig. 2.9.

Figure 2.10(b) shows, for each mode, the spatial resolution dependence with the tip-sample separation. ImageJ software is used to estimate the spatial resolution with a 16 %/84 % criteria. As being already observed on Fig. 2.9(a), the spatial resolution of the Lift-mode dramatically increases when the lift height decreases from 120 nm to 60 nm. In FM-KFM mode, the spatial resolution is not affected by the tip-sample distance, while a slight improvement is observed in AM-KFM mode. In the three modes, the spatial

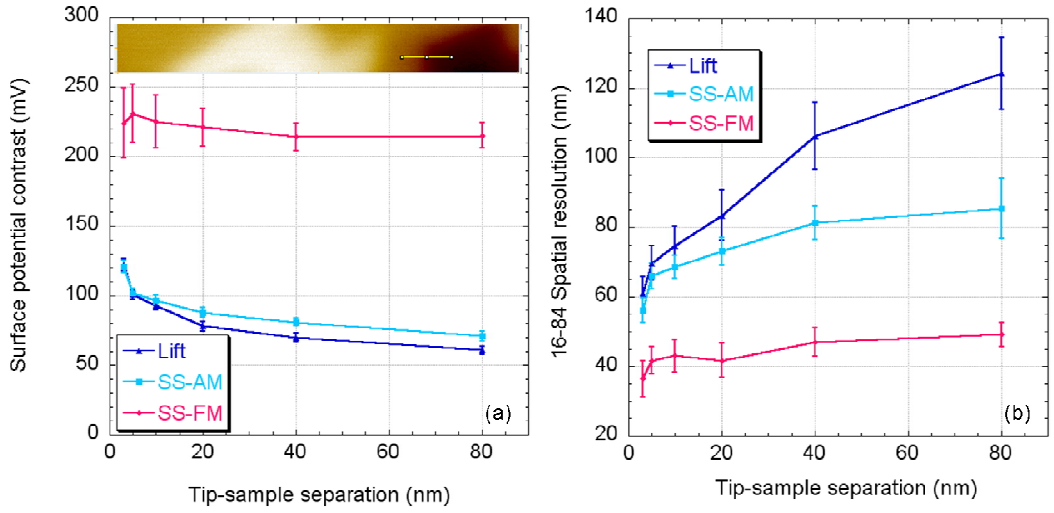

Fig. 2.10 Comparison for the three KFM acquisition modes (Lift-AM, single scan AM and FM) considering (a) the CPD contrast and (b) the spatial resolution versus the tip-sample separation. Measurements are done along the yellow line drawn in the inset.

resolution attains a value as good as 30 nm. We believe that this spatial resolution is limited by the topographical resolution and could be improved if sharper tips are used.

2.1.6.2 KFM with Dimension 3100 AFM

To check the results and to test the different parameters, measurements on the same samples have been done using the Dimension 3100 AFM. In this experiment, the FM-KFM drive frequency is increased to reduce the acquisition time, the AM-KFM drive amplitude is decreased as enough sensitivity can be achieved with a value of 2 V.

Figure 2.11 shows CPD images obtained on the same area of a graphene sample using the three KFM acquisition modes. The impact of the tip-sample distance on measured surface potential is analyzed. In this experiment, the tip-sample distance ranges between 48 nm and 2 nm. For the sake of clarity, the images are presented with the same scale bar with a maximum value of 500 mV. Fig. 2.11(b) shows surface potential images obtained by Lift- mode. We observe that: (i) large tip-sample distances lead to blurred images of the

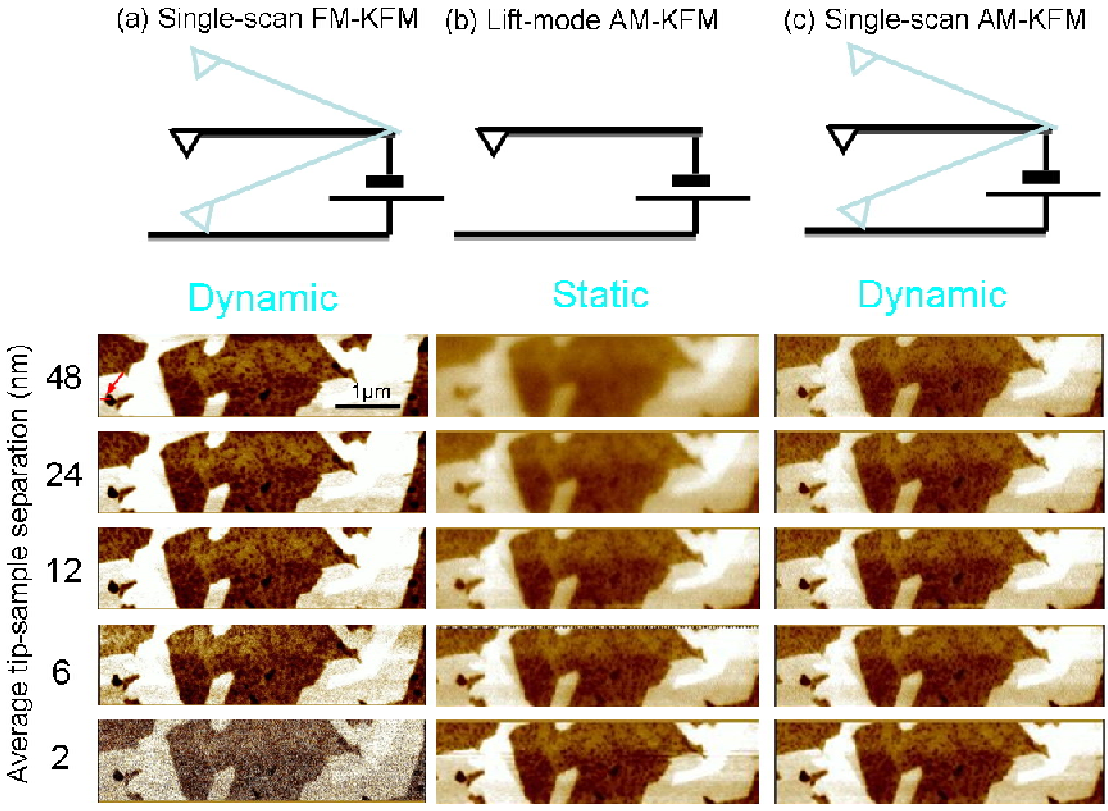

Fig. 2.11 CPD images on graphene sample with three common KFM techniques. Experiments are done with a D3100 AFM. The potential scale is 500 mV for all the images. (a) Single-scan FM-KFM exhibits the highest contrast (V_{ac}= 4 V, f_0 = 69 k Hz, f_{elec}= 900 Hz, scan rate= 0.4 Hz). (b) AM-KFM in Lift-mode shows strong dependence on tip-sample separation. (V_{ac}= 2 V, f_0 = f_{elec}= 69 kHz, scan rate= 0.4 Hz). (c) Single-scan AM-KFM shows less dependence on tip-sample separation but with lower contrast than (a). (V_{ac}= 4 V, f_0 = 69 k Hz, f_{elec}= 439 Hz, scan rate= 0.4 Hz).

surface potential; (ii) the contrast increases as the tip-sample distance decreases. For both SS-AM and FM modes, the tip-sample distance has less influence, even if a better contrast seems to be obtained in FM-KFM mode [Fig. 2.11(a)].

Spatial resolution and Contrast

To achieve a quantitative comparison of the images obtained using the three Kelvin modes, the contrast [Fig. 2.12(a)] and the spatial resolutions [Fig. 2.12(b)] are extracted along a line profile [red line in the inset of Fig. 2.12(a)]. Fig. 2.12(a) shows, for each acquisition mode, the variation of the contrast (obtained on one surface potential step on the graphene sample) with respect to the tip-sample distance. For both AM modes, a slight increase of the contrast is observed when the probe is approached closer to the sample surface. In FM-KFM mode, as in the previous experiments, the contrast is two times higher than the one obtained with AM mode and does not depend on the tip-sample distance (see also Fig. 2.11).

Fig. 2.12(b) shows that, in Lift-mode, the spatial resolution can be significantly enhanced by reducing the tip-sample separation. Indeed, the spatial resolution drops from 40 nm to 110 nm as the tip-sample separation goes from 12 nm to 50 nm. In the three modes, the highest spatial resolution (approximately 30 nm) is attained close to the sample surface. This value is limited by the use of a bulky Pt/Ir coated silicon tip which limits the topographic resolution. As a consequence, further significant improvement of the spatial resolution could be reached if sharper tips were used.

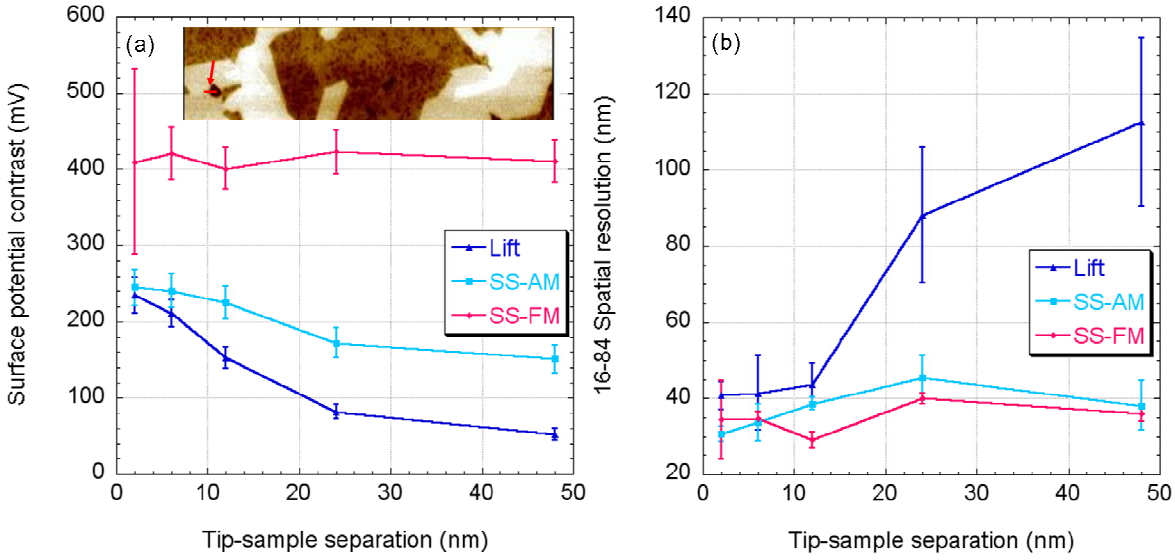

Fig. 2.12 Comparison between the three KFM acquisition modes (Lift-AM, single scan AM and single scan- FM) considering (a) the CPD contrast and (b) the spatial resolution versus the tip-sample separation. Measurements are done along the red line drawn in the inset.

2.1.7 **Discussion**

A simple qualitative interpretation can be made to explain the observed trend for the three acquisition modes. The main difference between both the single scan and Lift methods, independently of the force or force gradient detection used, is that the probe is mechanically driven in the single scan method. On the other hand, the z_0 tip-sample distance [see Fig. 2.11(b)] is constant in Lift-method during the CPD acquisition that is comparable to a "static" behavior of the probe. The measured V_{dc} voltage described in Eq. (2.3) is a weighted average of all the local potentials and therefore depends on the size of the feature on the surface sample as well as the probe geometry. In this case, the weighting factor corresponding to the gradient capacitance is a constant value taken at z_0 tip-sample distance. Thus, the resolution as well as the contrast become better when the tip-sample separation is reduced.

In the single scan method, the probe is mechanically driven during the CPD acquisition that is comparable to a "dynamic" behavior of the probe by analogy with the Lift-mode. As a consequence, the tip-sample separation z_0 is oscillating, which means that the weighting factor, which is respectively the first and second derivative probe-sample capacitance for AM-KFM and FM-KFM [Eqs. (2.3) and (2.4)], is averaged over one oscillation period. In this case, the probe reaches further into the surface sample leading to an effective probe distance smaller than the probe-sample distance. [85] As a consequence, CPD imaging in this condition is much less sensitive to the tip-sample distance and a stable resolution and contrast is expected over the total range (50 nm here).

The results presented in Fig. 2.9 and Fig. 2.11 are in agreement with this hypothesis. Nonetheless, FM-KFM mode appears to be more stable than the AM-KFM, where some slight changes are observed both on resolution and contrast. In force gradient sensitive detection, the electrostatic coupling between tip cone and the cantilever of the probe is very small. Thus, only the apex of the probe has a significant interaction with the sample surface, which results to a more local probing of the gradient force than in force mode where the cantilever and the cone plays a greater contribution when tip-sample distance is already more than 1 nm. [43]

2.1.8 **Summary and conclusion**

Lift-mode AM-KFM affords (i) a strong dependence of the CPD contrast on the tip-sample distance and (ii) a lower CPD contrast and spatial resolution than those obtained in other modes. The AM-KFM in single-scan has less dependence and better CPD contrast and spatial resolution than in Lift-mode mainly due to the higher weighted average on apex

with low separation. FM-KFM possesses both the highest CPD contrast and the highest spatial resolution regardless the tip-sample distance. Nevertheless, this mode requires higher AC bias to guarantee the stability while increasing the risk of tip-induced band bending in semiconductors.

2.2 Influence of experimental parameters in single scan FM and AM-KFM

In this part, we present the influence of the most important experimental parameters influencing the CPD measurement both in single scan FM and AM-KFM. The peak-offset, the driving amplitude V_{ac} as well as the driving angular frequency ω_{el} applied to the tip, and finally the phase reference are presented and studied.

2.2.1 Peak offset

In Tapping™ mode, the cantilever is not excited at the free resonant frequency f_0. Indeed, the drive frequency is chosen to maximize the sensitivity $\Delta A/\Delta f$ and this condition is met when the drive frequency is set at $f = f_0\left(1-\frac{1}{Q\sqrt{8}}\right)$. While approaching the sample, because of the attractive van der Waals force acting between the tip and the sample, the resonant frequency decreases. This results in a decrease of the cantilever amplitude from A_m away from the surface to A near the surface. The drive frequency is set in such a way that, while imaging, the oscillation amplitude A of the tip is set in the range between

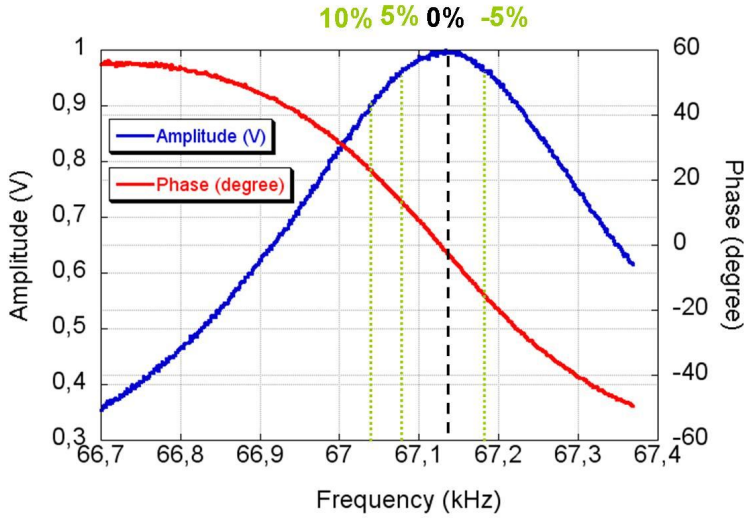

Fig. 2.13 The amplitude response of a cantilever around its resonant frequency. In the Veeco system, the peak offset percentage is defined as the decrease of the free resonant amplitude with respect to its maximum when the drive frequency is below or above the resonant frequency. The cantilever is excited at the corresponding frequency.

$0.9 \times A_m$ and $0.99 \times A_m$. The selection of the cantilever frequency plays an important role in the performance of the topography mapping although, as far as we know, this fact is not mentioned in the literature. As shown in Fig. 2.13, different offsets of amplitude ranging from 10 % to -5 % have been set in this experiment. The positive setting means a reduced frequency while the negative means the reverse way.

Fig. 2.14(a) presents the influence of the peak offset parameter on the topography and CPD images in FM-KFM of graphene sample. All the images have been acquired at the fundamental resonance; in these conditions, the amplitude setpoint is 1 V. However, the peak offset parameter induces a shift of the mechanical driving frequency as shown in Fig. 2.13. Thus, the resulting oscillation amplitudes are 0.95 V, 1 V, 0.95 V and 0.9 V respectively for -5 %, 0 %, 5 % and 10 % peak offset. After approaching, amplitude setpoints are respectively 0.7 V, 0.71 V, 0.71 V and 0.65 V.

The topography mapping shows that with the uncommon -5 % and 0 % settings, the results are noisier. Line profile of topography (Fig. 2.14(b)) enlightens this point: for settings of -5 % and 0 % the lines exhibit more errors in the flat area of the surface than with normal settings (5 % and 10 %). In theory, as the peak offset changes the drive

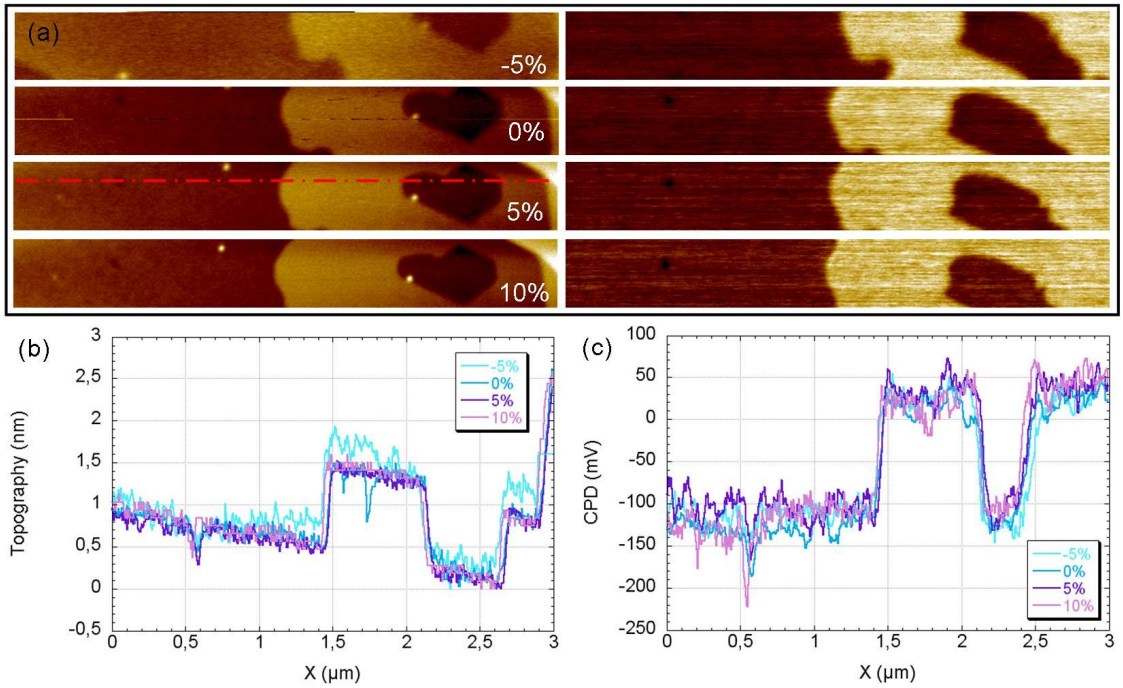

Fig. 2.14 Influence of the peak offset parameter on the topography and CPD images of graphene sample. (a) Left columns are topography ($\Delta z < 5nm$) images acquired in Tapping™ mode, while the right columns are CPD images acquired simultaneously in FM-KFM ($\Delta V < 400mV$). (b) Topography cross-section at the indicated location (red line) (c) CPD cross-section at the same place. In all experiments: target amplitude: 1 V, V_{ac}= 4 V, f_0 = 67 k Hz, f_{elec}= 400 Hz, scan rate= 0.1 Hz, BW= 1500 Hz, amplitude setpoints for topography measurement are 0.7 V, 0.71 V, 0.71 V, 0.65 V respectively for the peak offset -5 %, 0 %,5 %,10 %.

frequency, the slope of the phase is changed, and an influence on FM-KFM sensitivity is expected. However, the influence on the measured CPD value is not obvious [see Fig. 2.14(c)].

Similar experiment has been performed in AM-KFM. The influence of the peak offset parameter on the topography and CPD images is shown in Fig. 2.15. The target mechanical oscillation amplitude at the fundamental resonance has been set to 1 V in all the images. After approaching, amplitude setpoints are 0.7 V, 0.71 V, 0.71 V and 0.65 V, respectively for -5 %, 0 %, 5 % and 10 %. As observed in the previous case, a high level of noise is observable for peak offsets of -5 % and 0 % than with normal settings (5 % and 10 %). Line profile of topography shown in Fig. 2.15(b) enlightens this point. The reason of especially noisy topography at 0 % setting is not clear as the feedback parameters are optimized and the same amplitude setpoint is applied as in FM-KFM. However, the influence on KFM is limited as the rms noise level is 0.5 nm. The tip-sample separation dependence behavior of force sensitive detection can also be seen from the abrupt CPD variation in the slow scan axis due to the z-piezo height change in each line. The CPD contrast is extracted along the line profile used previously. Its estimated value is 100 mV, value to be compared with the 150 mV, obtained in FM mode.

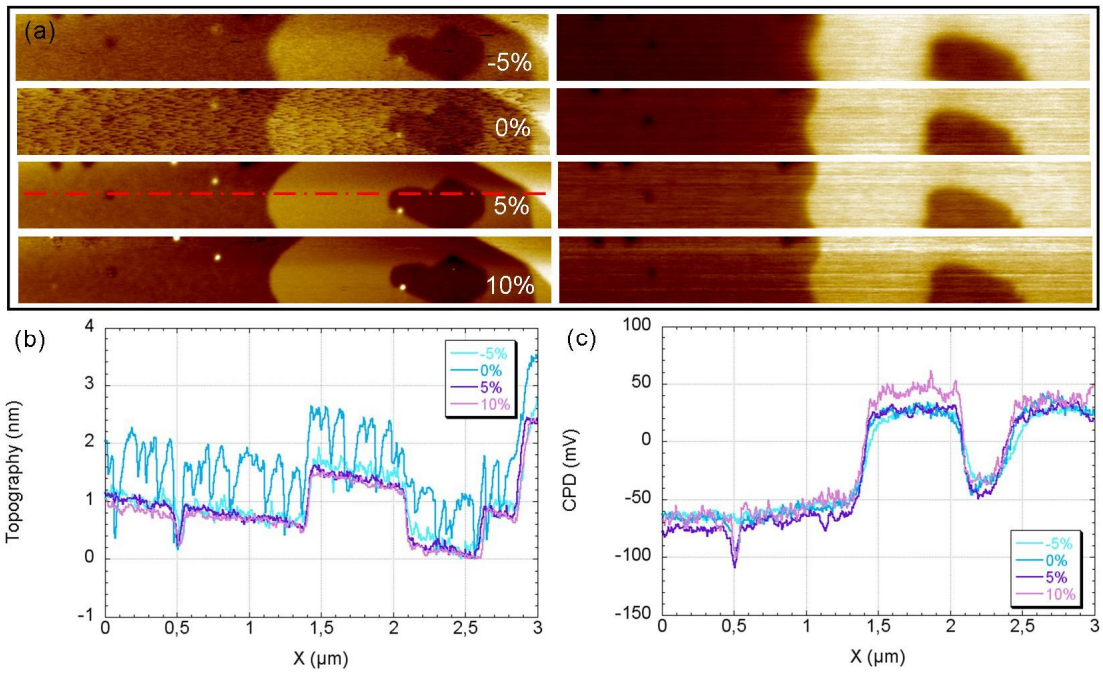

Fig. 2.15 KFM with different peak offsets. (a) Left columns are AM-AFM topography ($\Delta z < 5\,\mathrm{nm}$), while the right columns are AM-KFM CPD measurements ($\Delta V < 400\,\mathrm{mV}$) (b) Topography cross-section at the indicated location (red line) (c) CPD cross-section at the same place. In all experiments: target amplitude: 1 V, V_{ac}= 4 V, f_0 = 67 k Hz, f_{elec}= 423 kHz, scan rate= 0.1 Hz, BW= 1500 Hz, amplitude setpoints for topography measurement are 0.7 V, 0.71 V, 0.71 V, 0.65 V respectively for the peak offset -5 %, 0 %,5 %,10 %.

2.2.2 **Driving frequency**

As we mentioned before, two frequencies are superimposed in the single-scan FM-KFM mode. The first one is the mechanical oscillation often excited at the fundamental frequency of the cantilever (typically around 70 kHz for Pt/Ir coated silicon tips). In theory, higher eigenmodes can be used but the sensitivity decreases as the mode number increases. [86] Therefore, we always choose the fundamental frequency to drive the mechanical oscillation. The resulting mechanical phase used to detect the electrostatic force gradient is demodulated by a lock-in amplifier at the angular driving frequency ω_{el}. In FM-KFM, this angular frequency ω_{el} has to be in the range between a few hundreds of hertz and a few kilohertz. The upper limit is determined by the bandwidth of the lock-in amplifier used for amplitude and phase measurement of the mechanical oscillation [37] while the lower limit is set by a tradeoff between topographical crosstalk (noise level) and the scan speed.

Fig. 2.16 presents the amplitude of the mechanical phase modulation and the corresponding X component in function of the V_{dc} bias sweep and the influence of the angular driving frequency ω_{el}. These signals are measured by the second lock-in amplifier as shown in Fig. 2.1. As discussed above, we observed that, due to the bandwidth of the lock-in amplifier (fixed here at 777 Hz), the amplitude of the phase modulation decreases as the driving frequency increases. The signal intensity is 6 times higher at 500 Hz than at 4000 Hz, but the noise level does not change obviously. For these reasons, choosing the range of driving angular frequency between 500 Hz and 1000 Hz is a good compromise to optimize the bandwidth of the lock-in amplifier as well as the signal to noise ratio. However, we observe that for a driving frequency of 500 Hz, the amplitude is never zeroed even when the CPD is compensated. This is probably due to a crosstalk at low frequency in the mechanical phase signal. However, this influence is limited in our experiment as we nullify the monotonic X component signal instead of the amplitude. In addition, the dc bias voltage V_{dc} which have to be applied to nullify the signal shows a narrow distribution range smaller than 30 mV for all the tested driving frequencies.

As we will discuss in the next section, the intensity of the X component signal can vary not only with the phase offset between the ac driving signal applied to the oscillator piezo and the mechanical oscillation of the cantilever but is also proportional to the amplitude of the driving ac voltage V_{ac}.

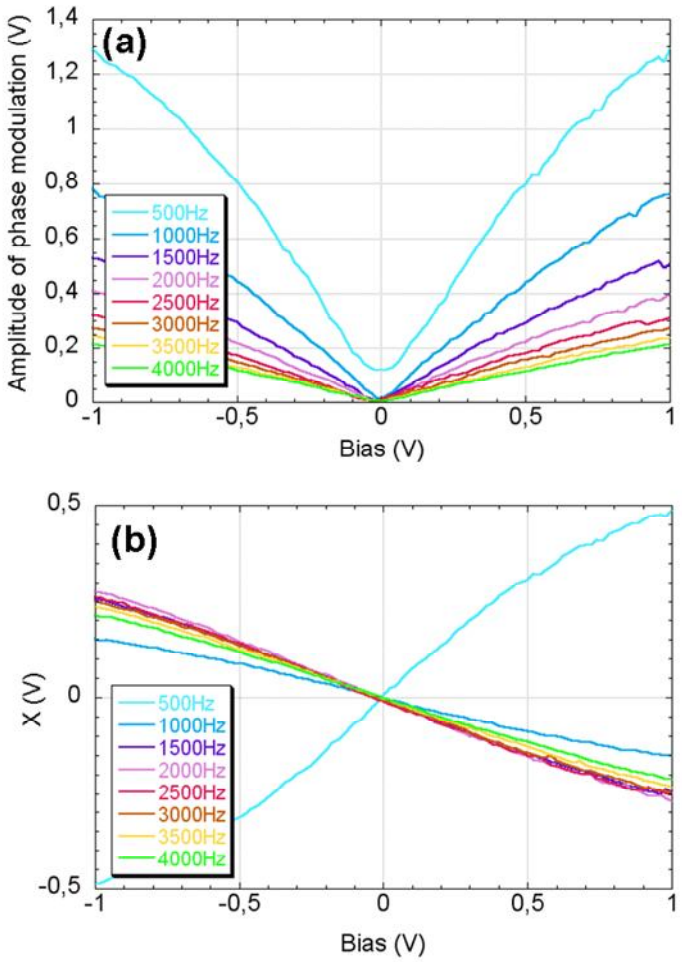

Fig. 2.16 Amplitude of the mechanical phase modulation (a) and the corresponding X component in function of the V_{dc} bias sweep and the influence of the angular driving frequency ω_{el}.

2.2.3 **Driving amplitude**

Usually, the ac driving amplitude V_{ac} setting used in FM-KFM mode is higher than the one used in AM-KFM mode. It is worth noting that higher amplitude can induce a band bending at the semiconductors surface. [87] Furthermore, the electrostatic interaction alters the topography measurement as shown below.

Before presenting the impact of the driving amplitude V_{ac} on the CPD measurements, we discuss its influence on the tip-sample separation while the z-feedback is on. In Tapping™ mode, the mechanical amplitude A_{ω_0} measured at the fundamental frequency is commonly used as feedback signal to control the tip-sample separation. The van der Waals force F_{vdw} as well as the electrostatic contribution F_{dc} have an impact on A_{ω_0}. In Tapping™ mode, the van der Waals force F_{vdw} is assumed to be constant if we work at the same tip-sample separation on the same region. However, the electrostatic contribution F_{dc} changes with the driving amplitude V_{ac}, following the relation:

$$F_{dc} = -\frac{\partial C}{\partial z}\left(\frac{1}{2}(V_{dc} - \Delta\Phi/q)^2 + \frac{1}{4}V_{ac}^2\right), \quad \textbf{(2.5)}$$

where $\Delta\Phi$ is the CPD between tip and the sample, $\frac{\partial C}{\partial z}$ is the capacitance gradient, which depends on the tip geometry and on the tip-sample separation. Hudlet *et al.* [88] calculated the capacitance gradient as a function of the radius *R* and the tip-sample separation z. If we neglect the contribution of the cone and if we consider the tip apex as a sphere of radius R located above an infinite plane we obtain [88]:

$$\frac{\partial C}{\partial z} = -2K\pi\varepsilon_0\left(\frac{R^2}{z(z+R)}\right), \quad \textbf{(2.6)}$$

where K is a positive constant and z the distance between the apex of the tip and the plane. By combining Eqs. (2.5) and (2.6), we obtain:

$$F_{dc} = \frac{R^2 K\pi\varepsilon_0}{z(z+R)}\left((V_{dc} - \Delta\Phi/q)^2 + \frac{1}{2}V_{ac}^2\right). \quad \textbf{(2.7)}$$

This equation shows that F_{dc} is a non-zero attractive force, which cannot be nullified. If we assume that other terms are constant, the increase of V_{ac} will enhance F_{dc} and therefore, the amplitude A_{ω_0} will decrease due to the higher attractive force. Finally, the z-piezo will retract a little (relationship between A_{ω_0} and the tip-sample separation *z* can be seen in Fig.2.6) to restore A_{ω_0} until it equals the amplitude setpoint A_{sp}. As a consequence, changing the driving amplitude V_{ac} while the z feedback is on has a direct influence on tip-sample separation.

Figure 2.17 shows the influence of the driving amplitude V_{ac} in FM-KFM. The amplitude of the mechanical phase modulation and the corresponding X component in function of the V_{dc} bias sweep are presented. When V_{ac} increases from 1 V to 2 V, the amplitude of the mechanical phase, modulated at the driving frequency ω_{el}, increases proportionally. This is in agreement with the fact that this amplitude is proportional to the electrostatic force gradient that is also proportional to the driving amplitude V_{ac} [see Eq. (2.2)]. However, we observe a non-linear slope on the curve at V_{ac} = 2 V, which is probably induced by the fact that the z feedback is on. Starting from 3 V, the effect of the z-piezo retraction discussed previously becomes more important, and we observe a decrease of the amplitude of the mechanical phase modulation. Indeed, as the tip-sample separation increases, the second derivative of the probe-sample capacitance $\frac{\partial^2 C}{\partial z^2}$ decreases [see Eq. (2.2)].

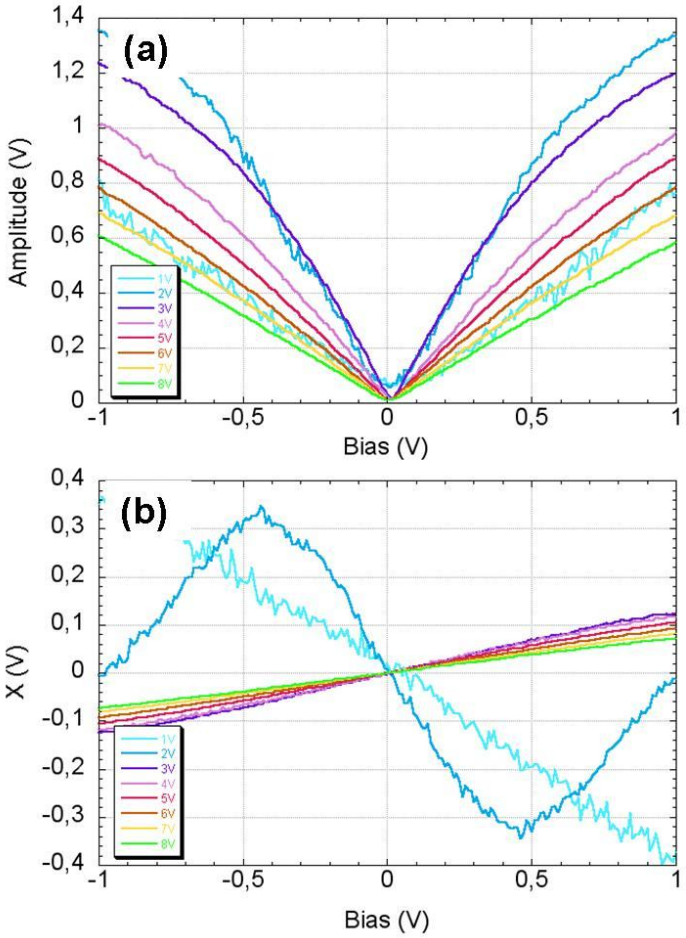

Fig. 2.17 Amplitude of the mechanical phase modulation and the corresponding X component in function of the V_{dc} bias sweep and the influence of the driving amplitude V_{ac}.

To check this assumption, we also did an experiment to monitor the mechanical phase signal and the z-piezo signal (topography) versus the dc tip bias while the z feedback is on. As known the mechanical phase is proportional to the force gradient and can be written:

$$\Delta\varphi \propto \frac{\partial F_{es}}{\partial z} = -\frac{1}{2}\frac{\partial^2 C}{\partial z^2}(V_{dc} - V_{cpd})^2 . \qquad \textbf{(2.8)}$$

In Fig. 2.18, the parabolic behavior of the mechanical phase induced by the sweep of the V_{dc} bias is clearly observed in the range between -2.5 V and 2.5 V while a slight variation of the z-piezo is also visible in this range. Outside this range, the mechanical phase presents a slow variation while the z piezo increases significantly, probably induced by the change of the second derivative of the probe-sample capacitance $\frac{\partial^2 C}{\partial z^2}$.

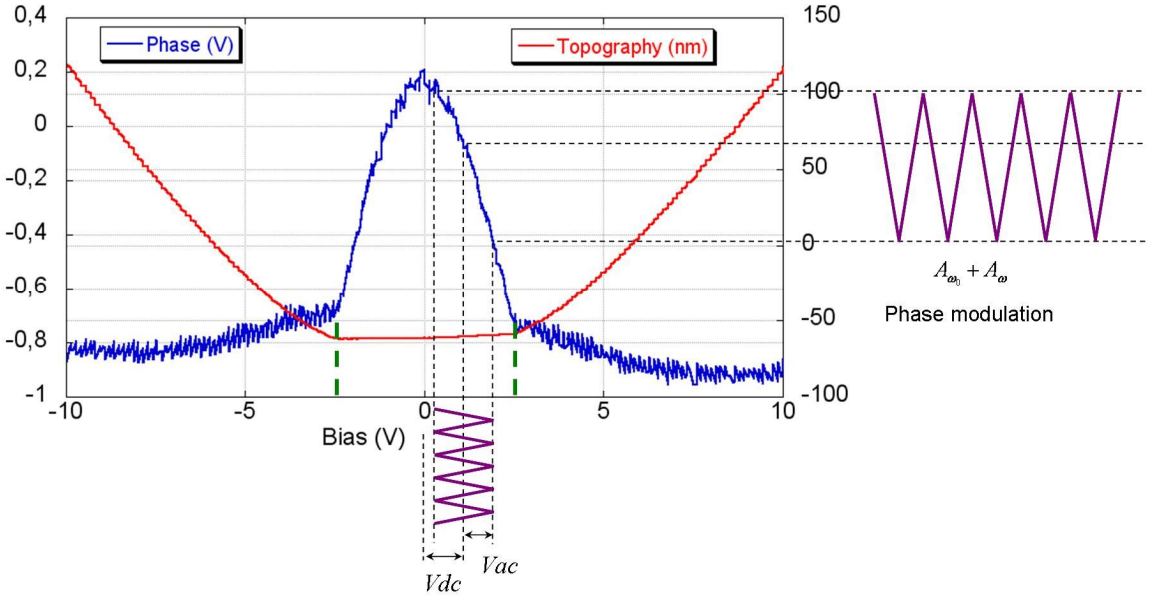

Fig. 2.18 Mechanical phase and z-piezo excursion as a function of dc tip bias. A parabolic behavior of the phase versus the dc tip bias is visible between the green dashed lines.

Following the previous observation, the variation of the amplitude of the mechanical phase modulated at the frequency ω_{el} can be explained. When the driving amplitude V_{ac} is increased, the part of oscillation entering in the "flat" region of the mechanical phase (Fig. 2.18) increases and leads to a decrease of the amplitude of the mechanical phase modulated at the frequency ω_{el}. In addition, we notice that the V_{dc} value read at X= 0, which corresponds to the CPD value, undergoes no obvious change when the driving amplitude V_{ac} is increased [Fig. 2.17(b)].

In AM-KFM, the second eigenmode of the cantilever is commonly used to separate the CPD measurement from the topographic measurement. It is reported that 2 V ac bias is sufficient to achieve comparable sensitivity. [42,89] However, due to the possible tip induced band bending [6,8] in semiconductors, one should avoid using high driving amplitude V_{ac}. Figure 2.19 shows the influence of the driving amplitude V_{ac} in the range of 1 V to 8 V. The oscillation amplitude at the second eigenmode of the cantilever as well as the corresponding X component in function of the V_{dc} bias sweep are presented.

Comparing with the results obtained in FM-KFM (Fig. 2.17), three main differences can be noticed:

i. Firstly, the resulting oscillation amplitude at the second eigenmode increases monotonically with the driving amplitude V_{ac}. This means that the V_{dc} bias has less influence on the ω_{el} component of the electrostatic force via the tip bending, as previously observed in FM-KFM.

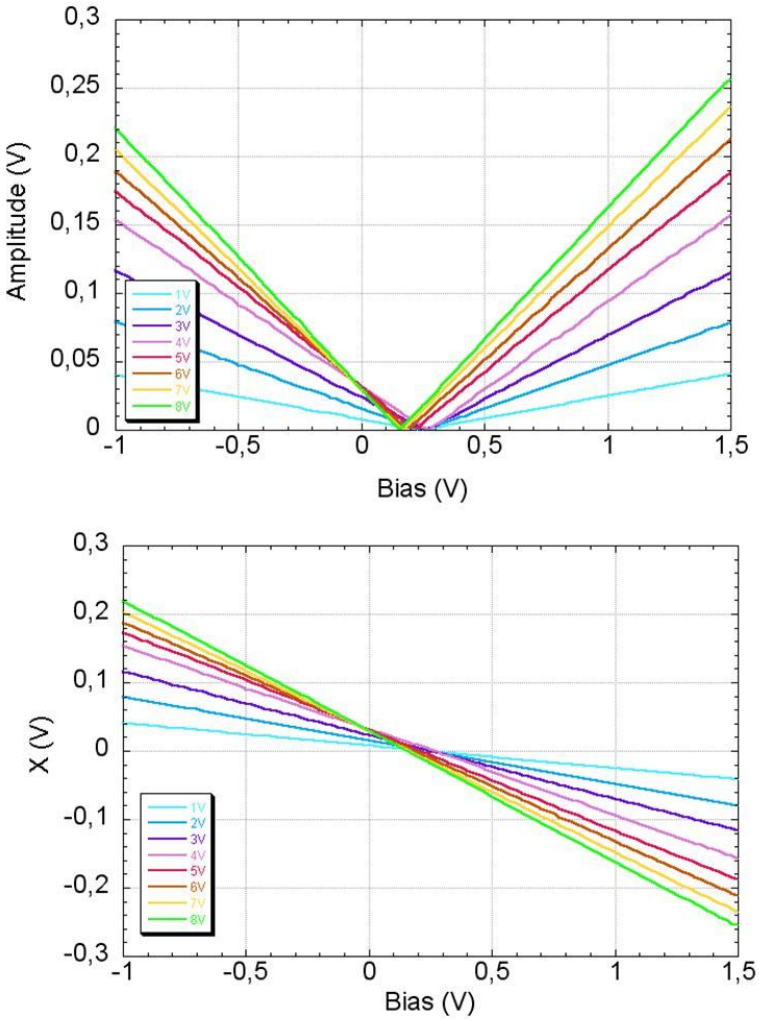

Fig. 2.19 Oscillation amplitude of the second eigenmode and the corresponding X component in function of the V_{dc} bias sweep and the influence of the driving amplitude V_{ac}.

ii. Secondly, the CPD value corresponding to the minimum of the oscillation amplitude decreases by approximately 200 mV from 1 V to 8 V ac tip bias amplitude. This indicates that the tip-sample distance or even the bending of the cantilever plays a role in the CPD measurement. As the cantilever is retracted, it averages larger area of the CPD and it reduces the measured value. [24,44,45]

iii. Thirdly, at fixed V_{ac}, the oscillation amplitude at the second eigenmode increases linearly with the $|V_{dc} - V_{cpd}|$, according to relation:

$$A_{\omega_{el}} \propto \left|F_{\omega_{el}}\right| = \left|\frac{\partial C}{\partial z}(V_{dc} - V_{cpd})V_{ac}\right|, \qquad \textbf{(2.10)}$$

where the $\frac{\partial C}{\partial z}$ is considered to be constant. Consequently, the $A_{\omega_{el}}$ is proportional to $|V_{dc} - V_{cpd}|$ and symmetric with respect to $V = V_{cpd}$.

2.2.4 Phase reference

In this part, the influence of the phase reference of the lock-in amplifier 2 (see Fig. 2.1) is analyzed. The reference phase has no influence on the output amplitude but since it offsets the output phase, it changes the intensity of the X component according to the relation:

$$X = A_{\omega_{el}} \cos(\varphi + \varphi_{ref}), \qquad \textbf{(2.11)}$$

where φ is the phase between the driving signal and the input signal, φ_{ref} is the phase reference that is used to change the intensity of the X output and $A_{\omega_{el}}$ is the amplitude of the input signal. In our case, $A_{\omega_{el}}$ refers to the oscillation amplitude at the second eigenmode in AM-KFM and to the amplitude of the mechanical phase modulated at the frequency ω_{el} in FM-KFM.

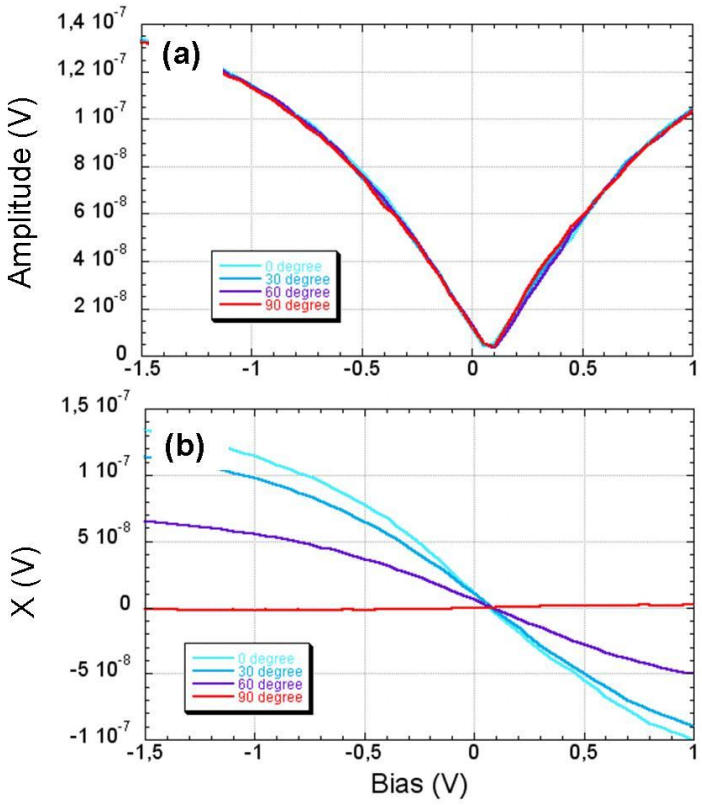

Fig. 2.20 Evolution of the mechanical phase modulated at the frequency ω_{el} in FM-KFM as well as the resulting X component in function of the V_{dc} bias for different reference phases.

Fig. 2.20 shows the behavior of the mechanical phase modulated at the frequency ω_{el} in FM-KFM as well as the resulting X component in function of the V_{dc} bias for different reference phases. The curves are similar than those observed in Fig. 2.17. As expected, no change is observed in the amplitude curves but we can notice that the amplitude is never zeroed due to the crosstalk induced in the SAM box (the driving frequency is fixed here at 500 Hz). However, it is worth noting that for each phase reference, the X component is always nullified for the same V_{dc} which means that the phase reference has no influence on the CPD measurement. We also notice the non-linear behavior of the amplitude and the X component when the condition $|V_{dc} - V_{cpd}| > 0.5\,\mathrm{V}$ is fulfilled. The interpretation of this, in fact is the same as we discussed in Fig. 2.17. As the z feedback is on, the static contribution of electrostatic force finally changes the $\frac{\partial^2 C}{\partial z^2}$ value by retracting the z-piezo if the DC bias increases. The consequent "flat" phase curve produced the non-linear behavior.

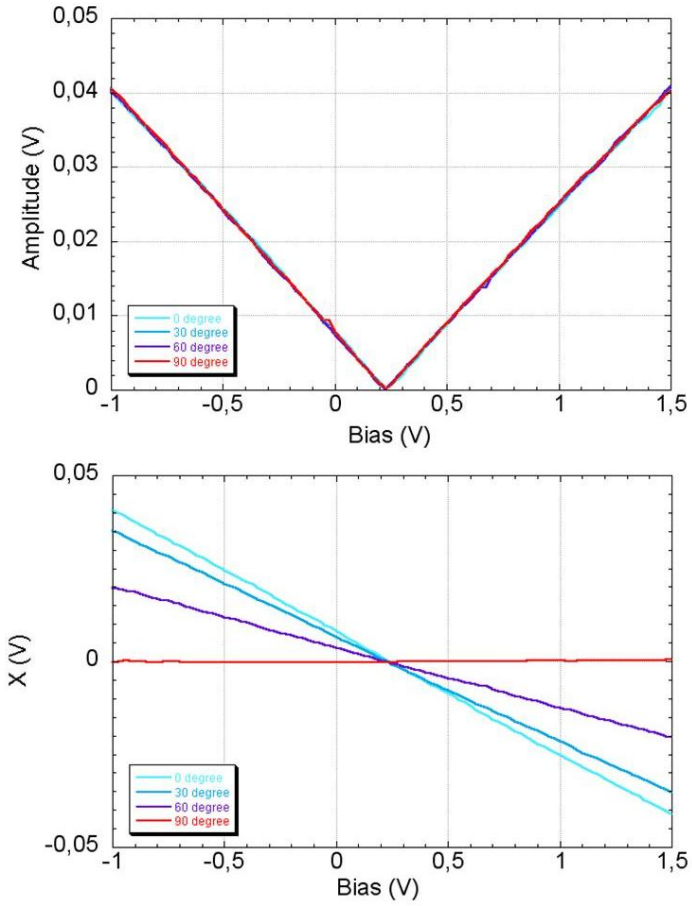

Fig. 2.21 Evolution of the oscillation amplitude at the second eigememode in AM-KFM as well as the resulting X component in function of the V_{dc} bias for different reference phases. (V_{ac}= 1 V, peak offset of 5 %)

Figure 2.21 shows the behavior of the oscillation amplitude of the second eigenmode in AM-KFM as well as the resulting X component in function of the V_{dc} bias for different reference phases. As expected, the oscillation amplitude does not change with different reference phase settings while the X component varies in agreement with the Eq. (2.11).

2.3 Summary and conclusions

As we discussed in the previous section, the long-range electrostatic force shows less dependence on the tip bending effect. The noise level is supposed to be the same with different reference phase settings. Therefore, the sensitivity depends on the slope of the X component of A_ω. In this chapter, KFM operating in ambient atmosphere is improved by developing KFM in a single-scan method using either frequency modulation (FM) or amplitude modulation (AM) mode. A comparative study between these two techniques and the common Lift-mode is done by imaging epitaxial graphene on SiC sample. The tip-sample separation effects on the surface potential spatial resolutions are discussed as well as experimental settings.

We can draw the following conclusions:

i. Using a sensitive detection to the electrostatic force gradient rather than to the electrostatic force provides a higher potential contrast regardless the tip-sample distance.
ii. KFM operated in dynamic mode (single-scan mode) shows less distance dependence than in static mode (double-scan mode).
iii. In all of these KFM modes, the spatial resolution and contrast of CPD imaging can be optimized as expected by working at a small tip-sample separation (typically a few nanometers).
iv. The influences of parameters such as peak offset, drive amplitude, drive frequency and phase reference are discussed in details.

Chapter 3

Surface potential imaging under secondary vacuum

This chapter deals with the development of the work function measurement by Kelvin probe force microscopy (KFM) under secondary vacuum. Indeed, working under secondary vacuum ensures a better control of the environment and therefore a better control of the sample surface. Moreover, the sensitivity is comparable to the one obtained under ultrahigh vacuum (UHV). In this chapter, we will provide the motivation to operate under vacuum and then, we will detail the instrumentation and its optimization. Finally, first KFM images will be presented and discussed. In conclusion, this technique will be compared to KFM operating under ambient atmospheres.

3.1 Motivation

3.1.1 Advantage of KFM under vacuum

The development of nanoscience makes the understanding of the electrical properties of nano-objects essential. The KFM is one of the most used techniques to image simultaneously, the topography and the contact potential difference (CPD) at the nanoscale. After about 20 years of development [38], KFM is mainly used in air, where semi-quantitative measurements with typical 40 nm resolution and 10 mV sensitivity can be achieved. [49,90,91,92,93] Moreover, KFM can be easily used to perform multiple comparative analyses. Accurate and reliable measurements can be achieved by working under UHV. [42,94,95,96,97] This technique is expensive and time consuming, but has nevertheless two advantages:

- Firstly, UHV provides better surface conditioning. In air, the work function of a sample depends on the quality of the surface, which can be heavily altered by the presence of a thin film of water and/or by the presence of a contamination layer. This affects both the contrast of the CPD images and the value of the work function. However, this

effect can be limited by a proper sample preparation such as cleaning protocols and by working in dry atmosphere.

– Secondly, under vacuum the quality factor Q increases dramatically. Typically, Q is greater than 30 000, a value up to 100 times more important than in air, which improves the sensibility of the force detection. Indeed, taking into account only the thermal noise and for signal-to-noise ratio of one, the minimum detectable force is [32,98]:

$$F_{\min} = \sqrt{\frac{4kk_BT}{\omega_0 Q}B}\,, \tag{3.1}$$

where k and k_B are respectively the spring and Boltzmann constants, B the bandwidth and ω_0 the resonant angular frequency. This equation shows that operating in vacuum results in a gain of at least one order of magnitude of the force detection sensitivity. The effects of other parameters are listed in table 3.1.

The effect of the pressure on the resonant frequency as well as on the quality factor is shown in Fig. 3.1. When operating in secondary vacuum in place of ambient atmosphere, the quality factor increases by a factor of about 100 due to the friction reduction. More specifically, Fig. 3.1(b) shows the dependence of the quality factor on the pressure: when operating in ambient atmosphere the quality factor is equal two a few thousands then it undergoes an abrupt increase as the pressure goes from 0.01 mbar to 10 mbar and reaches a plateau for pressure less than 0.01 mbar.

Table 3.1 Minimum detectable force limitation parameters and its influences

Parameters	Influences
k	Low stiffness causes “jump to contact”.
k_BT	Lowering the operating temperature from 300 K to 4 K increases the signal-to-noise ratio by at least of one order of magnitude.
B	Smaller bandwidth means longer scanning time.
ω_0	Defined by the geometry of the cantilever or use of the higher harmonics in the limit of cut-off frequency of photodetector.
Q	Increasing the Q factor (by going to high vacuum), one can achieve at least one order of magnitude for the detection of the force.

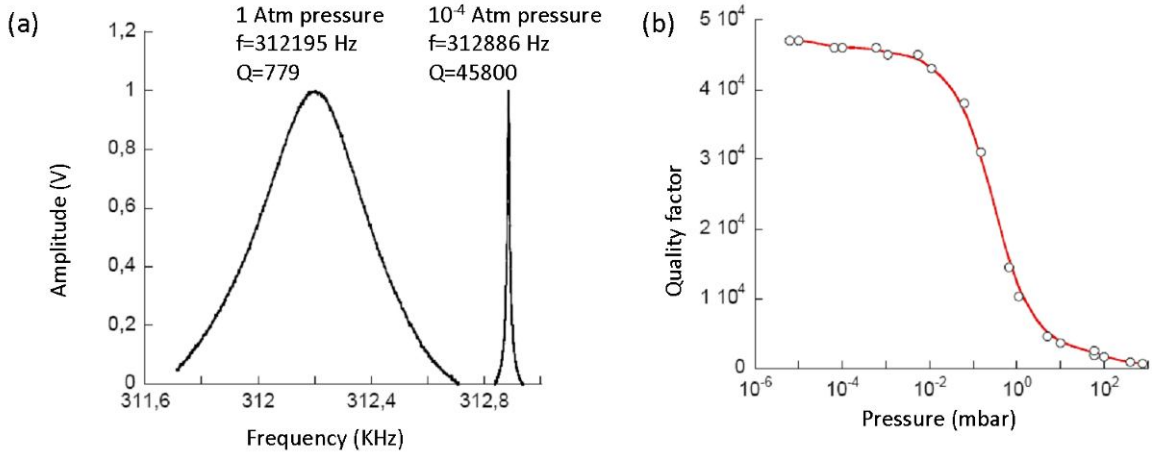

Fig. 3.1 (a) Resonant frequency at ambient pressure and at 10^{-4} mbar pressure (secondary vacuum). The quality factor roughly increased by two orders of magnitude. (b) Evolution of the quality factor with the pressure. A saturated region is observed below 10^{-2} mbar. [99]

In this chapter, we propose to develop and evaluate KFM operating under secondary vacuum. Indeed, operating under secondary vacuum ensures a better control of the surface in term of contamination allied. In addition, operating under secondary vacuum has the advantage of a high quality factor while keeping the ease of use and the low cost of an ambient KFM equipment.

3.1.2 **Why additional electronics is needed?**

In this experimental study, EnviroScope™ from Bruker Nano (Santa Barbara, USA) is employed as a microscope (see Fig 3.2). It is a multi-purpose platform for scanning probe microscopy (SPM) working under a variety of environments such as: (i) variable temperature (up to 300 °C in vacuum with a specific sample holder), (ii) variable pressure (up to 10^{-5} mbar), (iii) the choice of the ambient gas such N_2 or Ar. The vacuum is obtained by a two-step pumping system. The chamber is rough pumped from atmospheric pressure

Fig. 3.2 The standard connection of EnviroScope™ only enables amplitude modulated Tapping™ mode AFM and Lift-mode KFM. From left to right: EnviroScope™ AFM, Quadrex and NanoScope IIIa electronics.

to 10^{-3} mbar in approximately 10 minutes. Then, a turbo molecular pump (Varian V70LP) is used to obtain and maintain a secondary vacuum ranging between 10^{-4} and 10^{-5} mbar. The vacuum chamber hosts the atomic force microscope (AFM) which can operate in the so called KFM Lift-mode.

As mentioned in the previous section, a high quality factor decreases the minimum detectable force. However, in Tapping™ mode, a high quality factor dramatically increases the image acquisition time. Indeed, a time delay equal to the time constant [32]

$$\tau = 2Q / \omega_0 , \tag{3.2}$$

is necessary to achieve the steady state of the mechanical oscillator. As shown in the Table 3.2, the time needed to acquire one image increases by a factor of 100 when operating under secondary vacuum. This acquisition time is incompatible with the thermal drift which is approximately 600 nm/h. Therefore, the amplitude modulation mode is unsuitable when operating under vacuum.

On the other hand, the frequency modulation (FM) technique based on the real time detection of the resonant frequency is more appropriated in vacuum environment. In theory, the response of the system depends only on the resonant frequency. In practice, the response of the system is limited by the bandwidth of the close-loop control electronics which typically ranges between 1 kHz to 10 kHz, and leads to a time response similar to the time response achieved in AM mode. [32] Therefore, in order to perform measurement under secondary vacuum, the FM mode is required. In this study, an additional electronic from Nanonis (composed of real time controller and two oscillation controllers dual OC4) has been used in complement to EnviroScope™ electronic. The fundamental frequency of the cantilever is monitored in real time and a frequency shift setpoint is used in the z controller to maintain the tip-sample distance constant.

Table 3.2 Time constant compare between ambient atmosphere and vacuum

	In ambient atmosphere	**In secondary vacuum**
Quality factor (Q)	≈ 250	≈ 25000
Resonant frequency (f_0)	≈ 75 kHz	≈ 75 kHz
Time constant (τ)	1.06 ms	106 ms
Minimum time for 512x512 image (t)	0.146 h	14.6 h

3.2 Non-contact AFM under secondary vacuum

3.2.1 System connections

The Fig. 3.3 presents the general overview of the connections necessary to perform AFM in FM mode (also called non-contact AFM or NC-AFM). Two signal access modules (SAM) are connected on each sides of the Quadrex electronic: hereafter, we call SAM 1 the SAM located between the microscope and the Quadrex electronic and SAM 2 the SAM located between the Quadrex electronic and the Nanoscope electronic. SAM 1 is used to extract the photodetector signal via the IN0 output and to mechanically drive the cantilever via the ANA1 input. An ac voltage feeds the tip actuator through a BNC cable connecting the ANA1 input of SAM 1 to the Nanonis OUTPUT. The photodetector signal feeds the INPUT of the Nanonis electronic via the IN0 output of SAM 1. SAM 2 is used via the IN0 input as an input to feed the z feedback signal. The Nanonis electronic includes a lock-in amplifier and a PID controller to ensure to real-time measurement of cantilever frequency. The AUX1 output from the Nanonis electronics provides a dc signal, proportional to the difference between the real-time frequency shit Δf_0 and the frequency shift setpoint $\Delta f_{0,set}$, which, from that point on, will be named frequency shift difference. This dc signal is sent to IN0 input of SAM 2 and is used as the feedback signal by the z-controller in the Nanoscope IIIa electronic to maintain a constant distance between the tip and the sample.

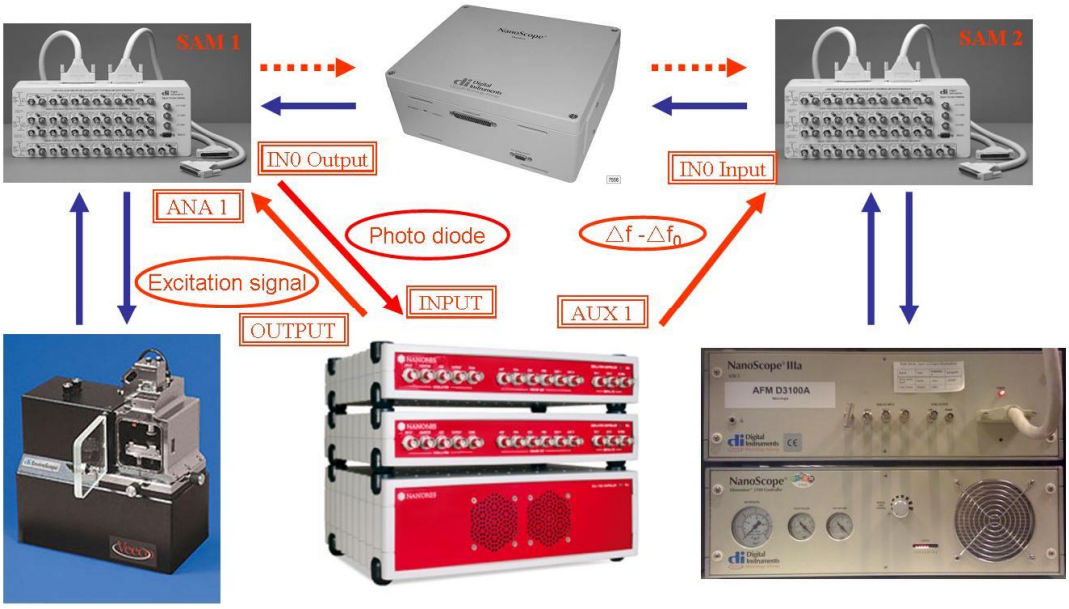

Fig. 3.3 Overview of the connections necessary to realize AFM measurement in FM mode (or NC-AFM) with an EnviroScope™ system working under secondary vacuum. Two SAM boxes as well as a Nanonis electronic are needed. The details about connections are given in the text.

Fig. 3.4 shows a more detailed schematic diagram of the setup. The blue and red parts correspond respectively to Nanonis electronic and to the EnviroScope™ AFM microscope including the Nanoscope controller and SAM boxes. In contrast to the Tapping™ AFM, FM technique is more suitable when operating under vacuum. In this mode, the cantilever oscillates always at its resonant frequency and, while scanning, the auto-oscillation of the cantilever is maintained. In our case, the amplitude and the phase are extracted from the photodetector signal by using the Nanonis lock-in amplifier. The amplitude is kept constant by using a feedback loop satisfying the Barkhausen stability criterion, which adjusts in real-time the mechanical driving amplitude V_{exc}. The phase signal is used by the digital phase-locked loop (PLL) included in the Nanonis electronic to measure the real-time resonant frequency of the cantilever. In fact, a feedback loop is used to maintain a zero phase. In practice, a frequency shift Δf_0 relative to the free resonant frequency f_0 is measured. A change in the gradient force between the tip and the sample results in a quasi-instantaneous change of the frequency shift Δf_0, which is negative in the case of attractive forces and positive for repulsive forces. The time response of the loop is fixed by the bandwidth of the PLL, which typically ranges between

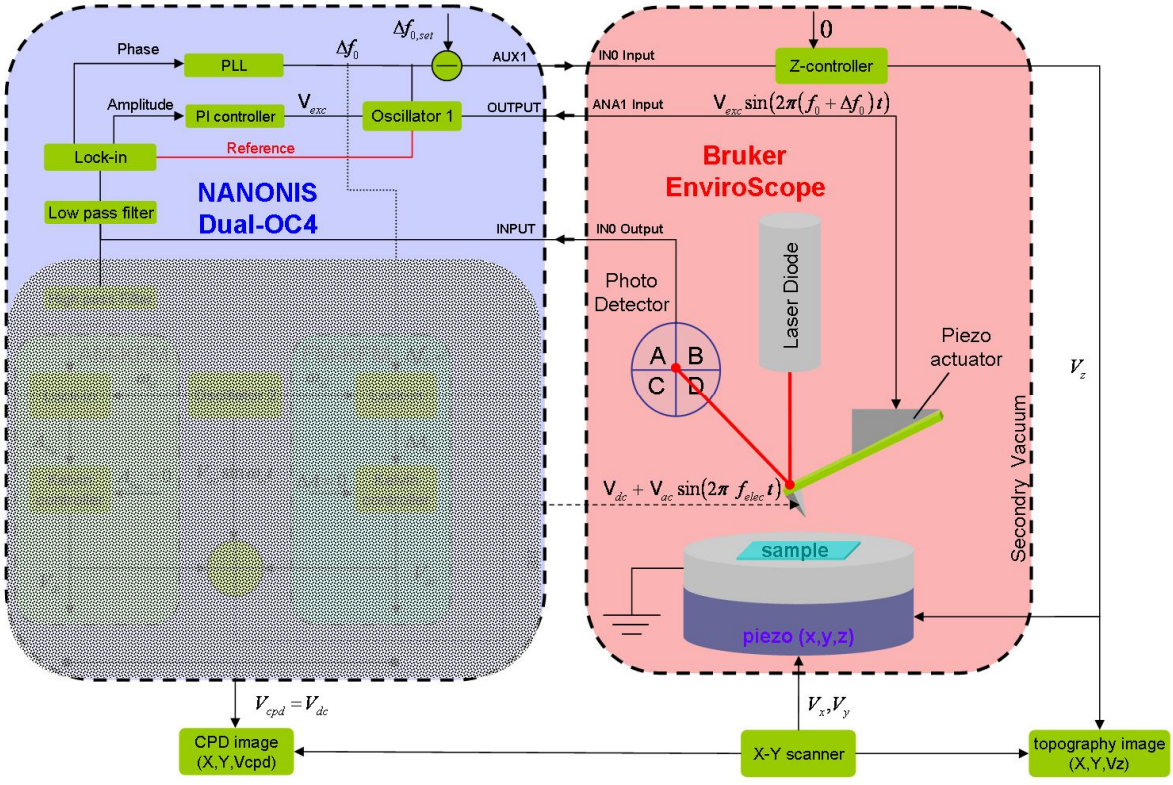

Fig. 3.4 Detailed setup of NC-AFM working under secondary vacuum. Nanonis electronic and Enviroscope™ are respectively represented in the blue part and red part. Details are given in the text. The shaded area corresponds to the KFM part and will be discussed after.

1 kHz to 10 kHz. As a consequence, the signal $V_{exc} \times \sin\left(2\pi\left(f_0 + \Delta f_0\right)t\right)$ is fed to the piezo actuator in order to excite the cantilever at its resonant frequency and at a constant oscillation amplitude. A frequency shift setpoint is defined to work at a constant tip-sample distance sample. The Nanonis electronic provides a dc signal proportional to the difference between the real-time frequency shit and the frequency shift setpoint, which is used by the Nanoscope IIIa controller as a feedback signal.

3.2.2 **Resonant frequency measurement**

Due to the high value of the quality factor under secondary vacuum, the acquisition of the resonance curve is more time-consuming than under ambient pressure condition. On the other hand, an accurate measurement is important to adjust the proportional and integral gains of the phase and amplitude feedback loops. Consequently, it is important to measure the resonance curve quickly and with accuracy. In the Nanonis software, the quality factor is automatically evaluated by fitting the phase curve near the resonant frequency. High quality factor results in a very sharp resonance curve and a very steep

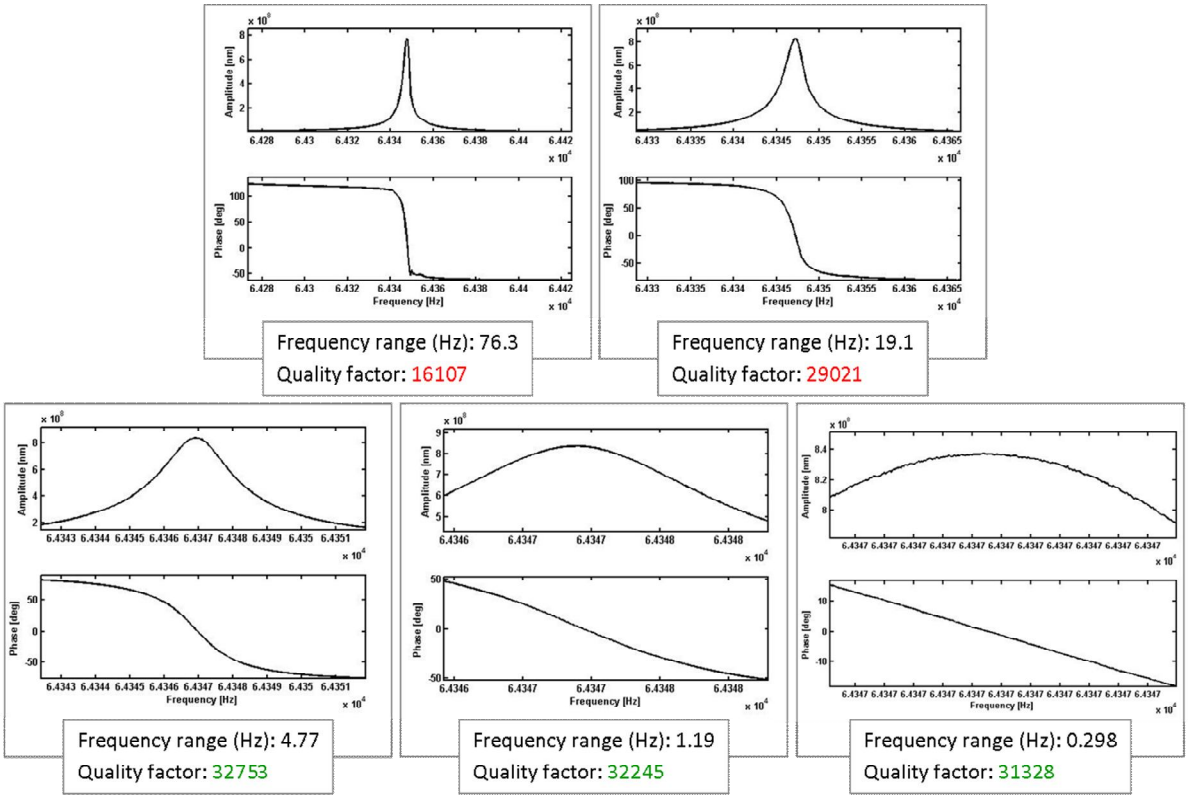

Fig. 3.5 Sampling rate effect on the accuracy of the estimation of the quality factor. 256 points are used for each frequency range. Result shows that 100 points inside the bandwidth of resonance curve guarantee quality factor measurement with a standard deviation below 3%. Details can be found in the text. Experimental settings: drive amplitude of 10 mV, pressure of 10^{-4} mbar, time interval of 300 ms.

phase curve near the resonant frequency. More specifically, the bandwidth is proportional to the inverse of the quality factor:

$$\Delta f = \frac{f_0}{Q}. \tag{3.3}$$

Typically, the fundamental resonance of our Pt/Ir coated silicon tip (Nanosensors, Neuchatel, Switzerland) is approximately 65 kHz with a quality factor of about 32000 under secondary vacuum resulting in a bandwidth of approximately 2 Hz and in a time constant τ calculated from Eq. 3.2 of about 157 ms, which defines the minimum time interval required to sample the resonance curve.

The Fig. 3.5 presents the sampling rate effect on the accuracy of the quality factor determination. The sampling rate is defined as the interval in Hz used between each data acquisition. In this example, 256 points have been used for each resonance curve. Moreover, a period of $300\ \mathrm{ms}$, which is two times higher than the time constant τ, is used to ensure that the steady-state regime of the cantilever oscillation is attained. As we can see the estimated quality factor exhibits a strong deviation when the sampling rate is too high (typically around 16 000 for a sampling rate of 0.3 Hz) and becomes more precise when the frequency range decreases. With a frequency range below 4.77 Hz, the quality

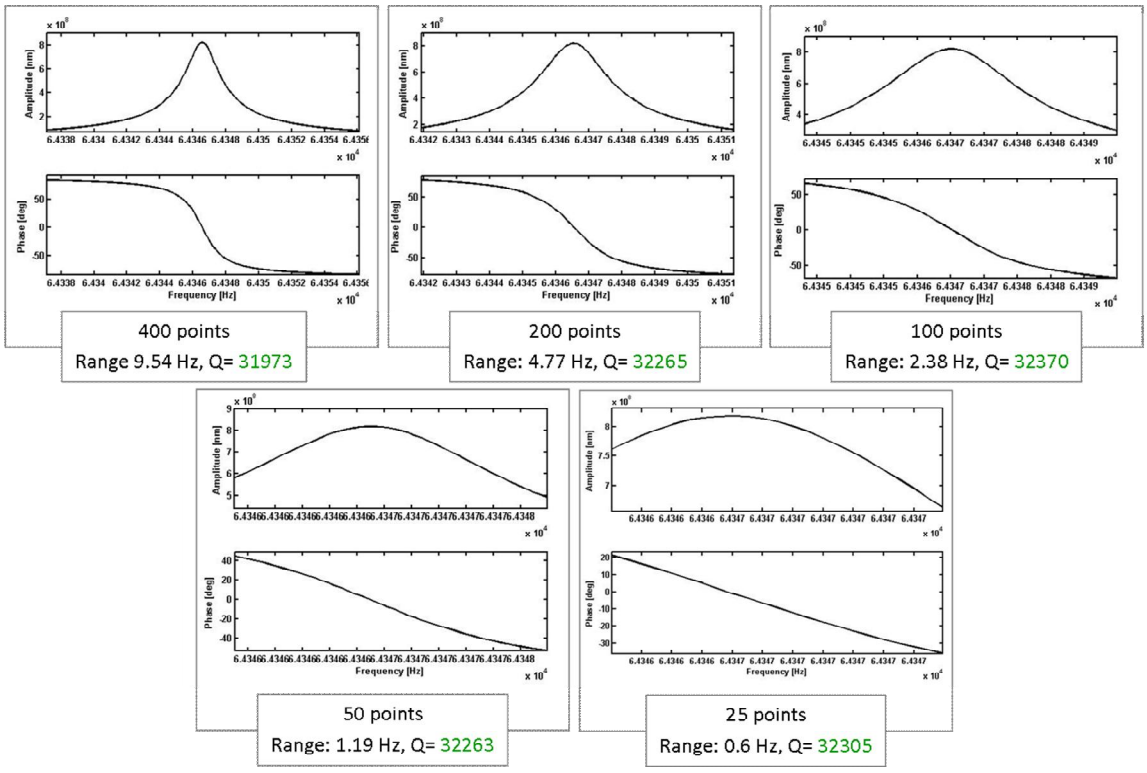

Fig. 3.6 Resonant frequency sweeps at constant sampling rate of 23 mHz. Results show that the quality factor measurement is accurately estimated with a standard deviation below 1%. Experimental settings: drive amplitude of 10 mV, pressure of 10^{-4} mbar, and time interval of 300 ms.

factor deviation is less than 3 %. Let's take the frequency range of 4.77 Hz as an example, the number of measurement points within the bandwidth is $256/4.77\ \mathrm{Hz}\times 2\ \mathrm{Hz}\approx 100$. This indicates more generally that when the sampling rate is higher than $\Delta f/100$, the quality factor estimation done by the Nanonis software is guaranteed with accuracy.

In order to confirm this observation, different sweeps at constant sample rate of 23 mHz have been performed as can be seen in the Fig. 3.6. In this case, the sweeping time is increased when the frequency range is increased. For each curve, the time interval is above the time constant τ. Results show that the quality factor measurement is accurately estimated with a standard deviation below 1 % even when 25 points are used corresponding to a sweeping range of about 0.6 Hz.

3.2.3 **Noise consideration of the system**

Due to the rubber seal this system can only hold a pressure lower than 10^{-4} mbar less than 3 minutes after the pump has been switched off. To maintain a vacuum in AFM chamber in the range of 10^{-5} to 10^{-4} mbar we must keep pumping. The position of roughing and turbo pumps can be seen in Fig. 3.7. The EnviroScope™ is placed on a vibration isolation

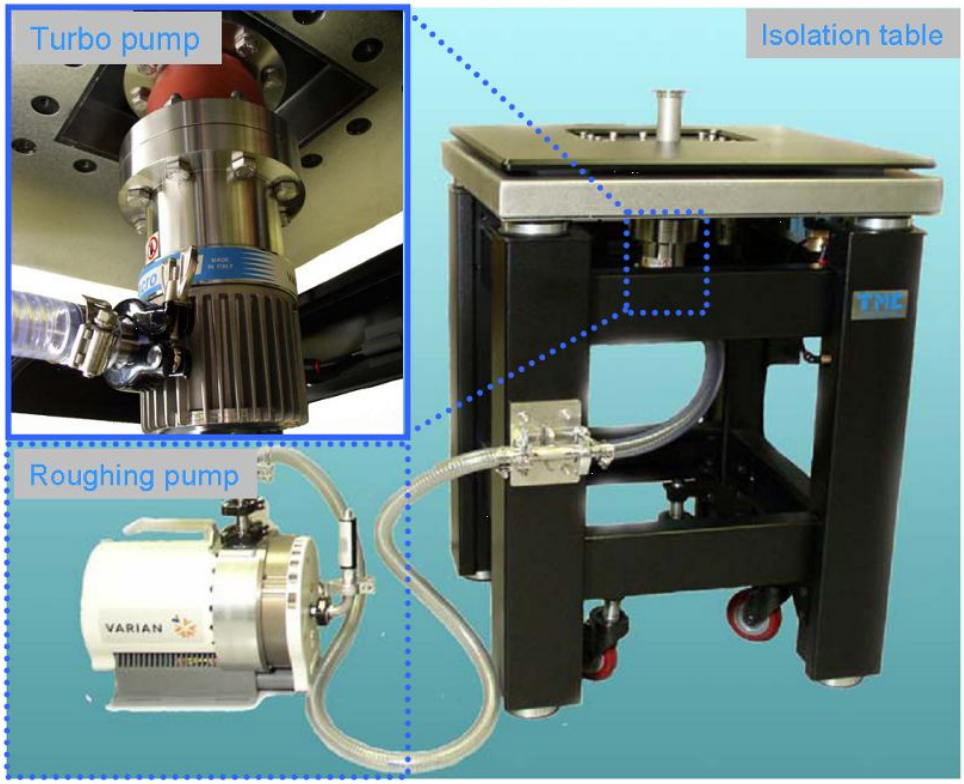

Fig. 3.7 The connection of roughing and turbo pumps to the isolation table. The roughing pump has a long tube connection but the vibration influence is reduced by fixing the tube on the isolation table, while the turbo pump has a direct link to the microscope vacuum chamber. Modified images extracted from EnviroScope™ user manual.

table, which limits the mechanical vibrations thanks to a damping system. In addition, an acoustic hood improves isolation from the environmental noise.

Tapping™ mode AFM has been performed in ambient atmosphere to evaluate the influence of the pumps vibration on the "quality" of the topography images and to evaluate the benefits of the noise isolation cover. To do so, the valve between the turbo pump and the AFM chamber is closed. Thin polysilicon film deposited on silicon has been used for the test. The Fig. 3.8 shows both topography and error signal[5] images. The rms roughness of the topography is used to evaluate the influence of the pumps vibration.

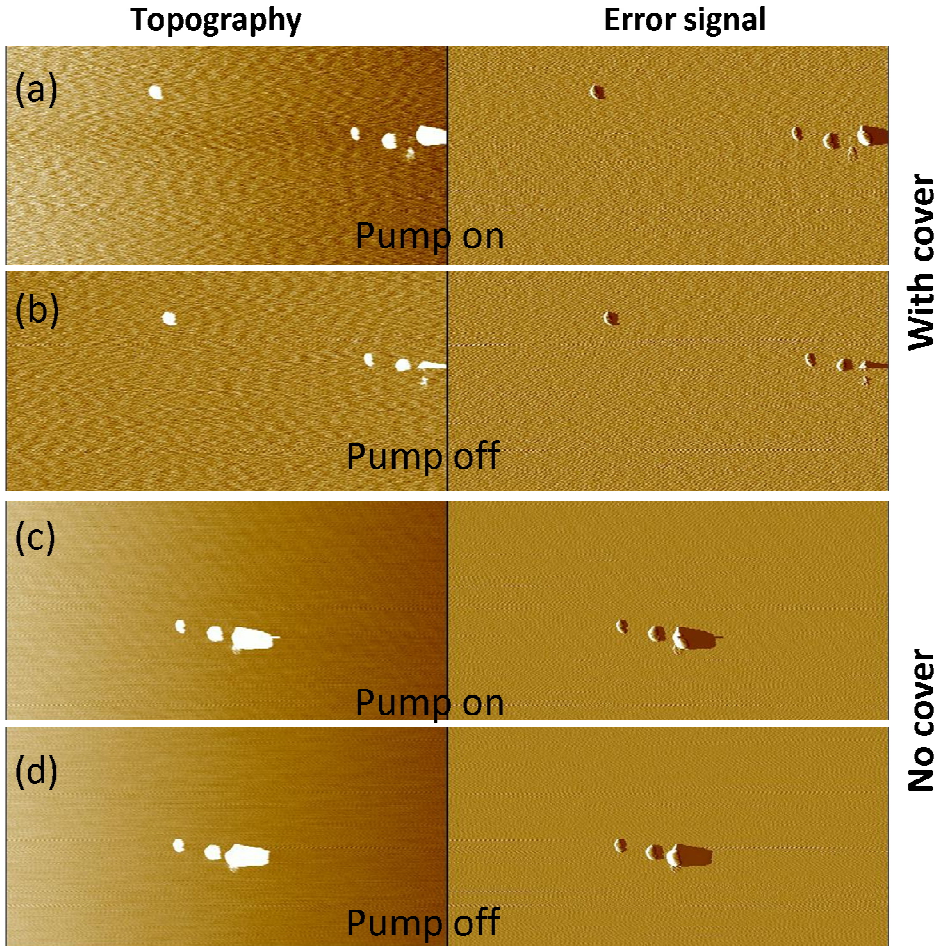

Fig. 3.8 Noise test experiments regarding to the vacuum pumps and noise isolation cover. AFM images are performed on polysilicon layer using a silicon tip. The topography scale is 30 nm and the error signal scale is 500 mV. The rms roughness is respectively 1.08 nm (a), 1.10 nm (b), 0.36 nm (c) and 0.33 nm (d). The related rms roughness of amplitude is respectively 21.0 mV, 22.9 mV, 11 mV and 9.6 mV. Experimental settings: A= 21 nm, image size of 5 µm x 3 µm and scan rate of 1 Hz.

[5] The resulting error signal is the difference between the amplitude setpoint and the real-time value.

Fig. 3.8(a) and (b) show no significant change in the roughness with or without the pump working. Fig. 3.8(c) and (d) show that operating with the noise isolation cover increases the rms roughness by a factor three. A possible explanation can be that the heavy cover makes the noise isolation less functional (i.e. the gas in the damper is compressed more, as well as the silica gel), which facilitates the noise propagation from the floor.

3.2.4 **Photodetector calibration**

To measure the oscillation amplitude of the cantilever a calibration of the photodetector is necessary. The aim of the calibration procedure is to convert the quadrant photodiode signal from volts into nanometers. The calibration coefficient can be found by making tip-sample approach-retract curves in contact or dynamic mode. Depending on the chosen mode different parameters can be measured. Respectively, for the contact and dynamic mode, the cantilever deflection and the cantilever oscillation amplitude in function of the tip-sample distance should be characterized. In this section, we explain the calibration method using the deflection measurement. We want to point out that, the calibration value can be influenced by several parameters, such as (i) the position of the laser on the cantilever, (ii) the sample stiffness and (iii) the laser position on the photodetector. In this section, we look into these factors one by one.

In the Fig. 3.9, five different stages of the approach-retract procedure in contact mode are presented. During stages A and B the tip is approaching to the surface, while during

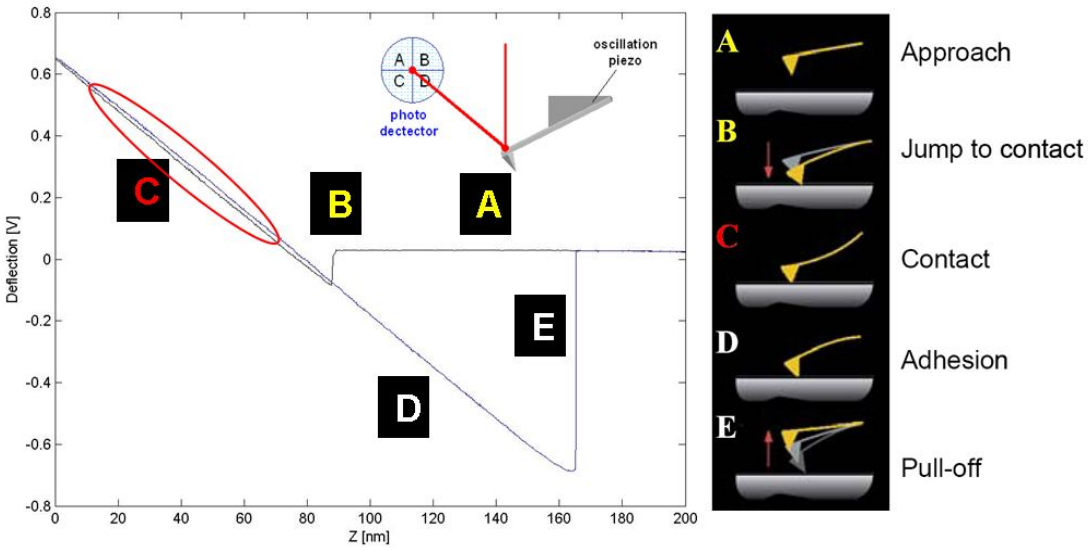

Fig. 3.9 Approach-retract curves in contact mode and related tip locations at each stage. A: The tip is approaching to the sample surface, no deflection on the photodetector. B: The tip jumps to contact, abrupt change in deflection. C: The tip is in contact with the sample surface, the slope of the deflection provides information on the hardness of a sample (see details in text). D. The tip stays in contact with the sample surface due to adhesive force(s) E. The tip is suddenly pulled off, so the deflection makes huge change but the z-piezo remains the same.

stages D and E the tip is retracting from the surface. Additionally, during the stage C the tip is in contact with the sample surface. Moreover, at this stage the tip is firstly pressed to the surface and secondly pulled from the surface. Taking into account the linear behavior in the stage C, it is possible to measure the z displacement of piezoelectric in nanometer and equivalent cantilever deflection in volts. If the sample surface is considered to be not deformable, the ratio of z-distance and the cantilever deflection gives the calibration value.

Tests of laser positioning on the cantilever have been performed and the results are shown in Fig. 3.10. In this experiment, flat silicon sample is used. The laser is placed in three different positions on the Pt/Ir coated silicon cantilever. We can see that calibration factor undergoes an increase of about 36% when the laser position is moved from the end to the middle of the cantilever. This means that, the z piezoelectric displacement required for different deflection voltages can vary and depends on the laser location on the

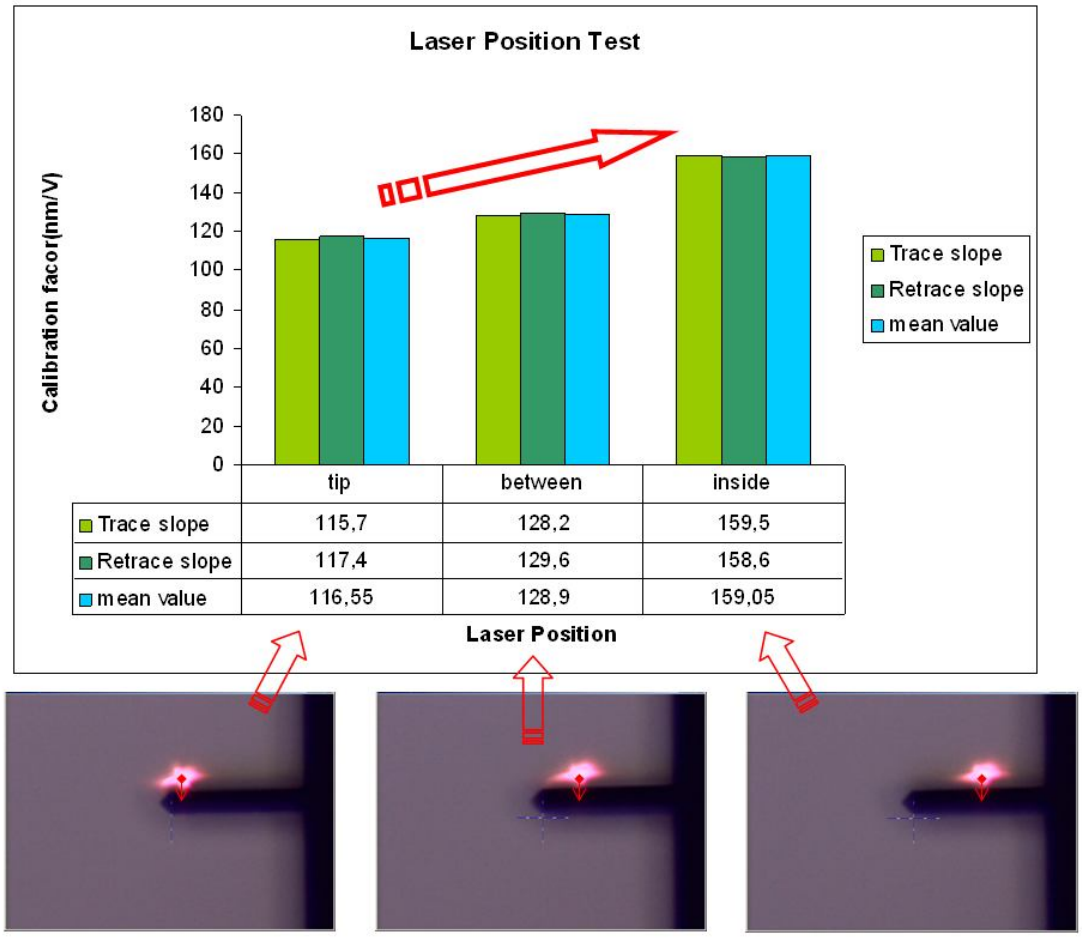

Fig. 3.10 Influence of the laser positioning on the cantilever on the calibration factor. "Trace slope" and "retrace slop" here means the approach and retract curve, respectively. Due to the hysteresis effect of the piezo, a small difference can be found in these two values. Therefore, an average value is calculated.

cantilever. In other words, moving the laser position towards the anchoring point decreases the sensitivity of photodetector due to the reduced displacement at the laser spot.

As the position of the laser spot on the cantilever can dramatically change the calibration factor, we have estimated, through the calibration factor, the reproducibility of the repositioning of the laser spot at the end of the cantilever. In this experiment, the laser spot is moved out of the cantilever and then replaced at the end of the cantilever. A standard deviation of about 3.7 % of the calibration factor has been computed using ten successive alignments as shown on Fig. 3.11.

The calibration method supposes that both the sample and the tip are infinitely rigid. Silicon sample usually used possesses a high Young modulus (E = 150 GPa). In order to estimate whether silicon is hard enough in the range of applied force (typically, 0.1 µN to 1 µN), SiC (E = 450 GPa) is used as a reference sample. The mean value of the calibration factor has been extracted from three measurements on SiC and from two measurements on Si. As shown on the Fig. 3.12, an increase of 8 % of the calibration factor is observed on the SiC, which suggests that the Si sample have been subjected to small deformations. The penetration distance δ of the substrate can be estimated using the classical Hertz contact formula

$$F \approx E_{sub}\delta^{3/2}R^{1/2} \tag{3.4}$$

where E^*_{sub} is the reduced Young's modulus, R is the radius of the tip apex and F is the force applied to the tip. Using the Eq. (3.4) the penetration depth in a silicon sample

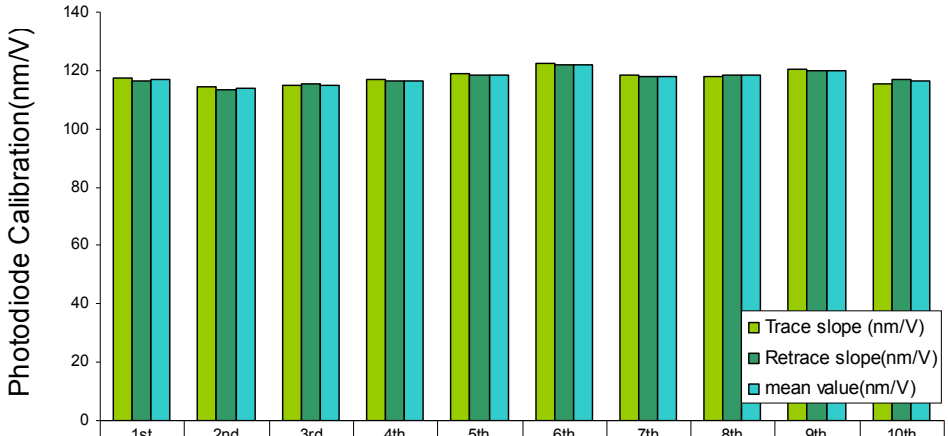

	1st	2nd	3rd	4th	5th	6th	7th	8th	9th	10th
Trace slope (nm/V)	117,3	114,3	114,9	116,7	118,7	122,3	118,4	117,9	120,3	115,6
Retrace slope(nm/V)	116,3	113,6	115,3	116,2	118,3	121,8	117,9	118,5	119,9	116,8
mean value(nm/V)	116,8	113,95	115,1	116,45	118,5	122,05	118,15	118,2	120,1	116,2

Fig. 3.11 Calibration factor calculated after 10 successive alignments of the laser spot at the end of the cantilever. The laser spot is removed and moved back before each test. It is done with Pt/Ir coated silicon tip on a silicon sample. The mean value of the calibration factor equals to 118.5 nm/V with a standard deviation of 3.7 %.

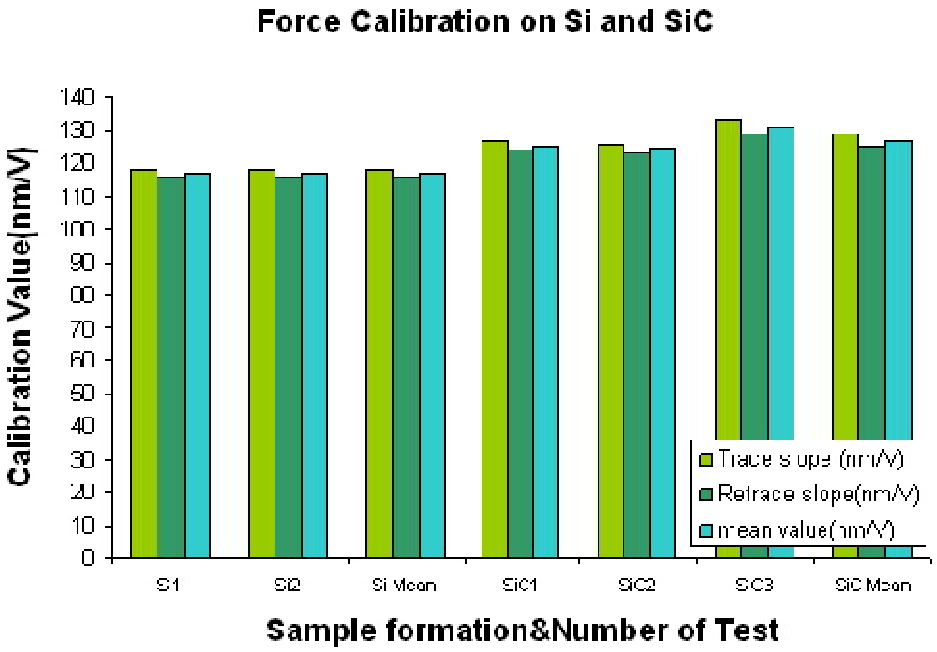

Fig. 3.12 Comparison of calibration factors obtained on Si and on SiC. In the test, trace, retrace and mean value of calibration value have been calculated. An increase of 8% of the calibration factor is observed on the SiC, which means that small deformations have been created on Si sample.

ranges from 0.3 nm to 1.6 nm when the applied force varies from 0.1 µN to 1 µN. The penetration depth is less than 1 % of the z piezo displacement (>100 nm).

The effect of the location of the laser spot on the photodetector has also been analyzed. In order to understand the non-linearity behavior of the quadrant photodetector, we first remind how it works. The blue inset in the Fig. 3.13 shows the schematic diagram of the quadrant photodetector. The voltages V_y and V_y generated respectively by a vertical deflection and a horizontal deflection are calculated according to the following relations:

$$V_y = C \times \frac{(I_A + I_B) - (I_C + I_D)}{I_A + I_B + I_C + I_D}, \tag{3.5}$$

$$V_x = C \times \frac{(I_B + I_D) - (I_A + I_C)}{I_A + I_B + I_C + I_D}, \tag{3.6}$$

where C is a constant; I_A, I_B, I_C and I_D are the photocurrent intensity of the four photodiodes. Due to the round shape of the laser spot and the gaussian distribution of the intensity, the derivative $\frac{\partial V_y}{\partial y}$ is not constant along the vertical axis.

The Fig. 3.13 shows the experimental results. As we expected, the calibration factor has a nonlinear behavior when the reflected spot "moves away" from the central position. This factor is lower while the reflected laser spot is in the center (corresponding to V_x and V_y equals to zero) but increases towards to the edge (corresponding to V_y equal to 10 V or -10 V). For a V_y range of -3 V to 2 V, the spreading of the calibration factor is less than 4 % while this spreading is medium from -6 V to 5 V. Outside this region, the calibration factor changes comparatively fast.

3.2.5 **Compatibility issues**

In order to perform a "soft" approach, the approaching speed has been set at a very low value with a motor step equal to 0.2 µm. In addition, a typical frequency shift of -5 Hz is set to ensure that a security clearance, between the tip and the sample, is left at the end of the motor-driven engagement. The Table 3.3 lists parameters well-suited for a "soft" approach. However, a warning window ("Engage failed: Bad RMS amplitude") pops up while engaging. The tip engagement consists in four steps: (i) pre-engage check, (ii) pre-engage, (iii) moving to slow engage position and (iv) approaching surface. Unfortunately, the role of each stage is not clear and not sufficiently documented and this prevented us from correcting ill-behaved engagement which cannot even pass the "Pre-engage Check" stage. To get round this issue, different methods have been tried including changing the amplitude setpoint, amplitude or frequency shift setpoint and, unfortunately, none of them work. Finally, this compatibility issue has been solved by using the original Tapping™ loop in the first three stages and by switching to Nanonis loop in the last stage.

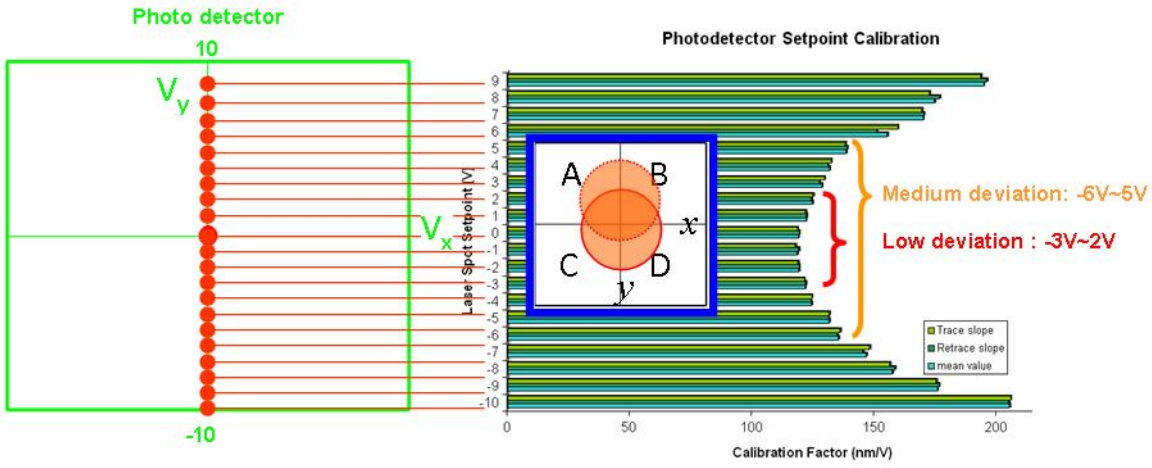

Fig. 3.13 Non-linear response of the calibration factor versus the vertical position of the reflected spot. The green square, which is the schematic of the vision system window in "Nanoscope" software, shows photodetector output voltage. The resulting calibration factor can be seen on the right. The blue squared inset in the middle shows the laser spot on four photodiodes in photodetector (See details in the text).

Table 3.3 List of parameters for safe tip engagement

Nanonis settings		**EnviroScope™ settings**	
Oscillation amplitude (nm)	20	I/P gain	0.1/0.1
Calibration value of $\Delta f_0 - \Delta f_{0,set}$ (Hz/V)	30	SPM sample clearance (µm)	200
		SPM safety (µm)	200

3.2.6 **Non-contact imaging under secondary vacuum**

Preliminary NC-AFM images obtained on epitaxial graphene on SiC are presented in Fig. 3.14. As no parameters have been optimized, these images only permit to prove the feasibility of non-contact AFM operating under secondary vacuum. During these preliminary experiments, different frequency shifts have been tested and as a result, NC-AFM is more stable when using -10 Hz and -15 Hz frequency shift setpoint.

As the control of the tip-sample distance is a key point to perform KFM measurements in good conditions, the first step has been to optimize NC-AFM imaging parameters. [46]

Among the various parameters to be optimized, we only discuss three experimental parameters and their influences on the NC-AFM imaging:

- the frequency/voltage converting factor used to provide the frequency shift difference $\Delta f_0 - \Delta f_{0,set}$ (see Fig. 3.3 for more details);
- the oscillation amplitude of the cantilever;
- the frequency shift Δf_0.

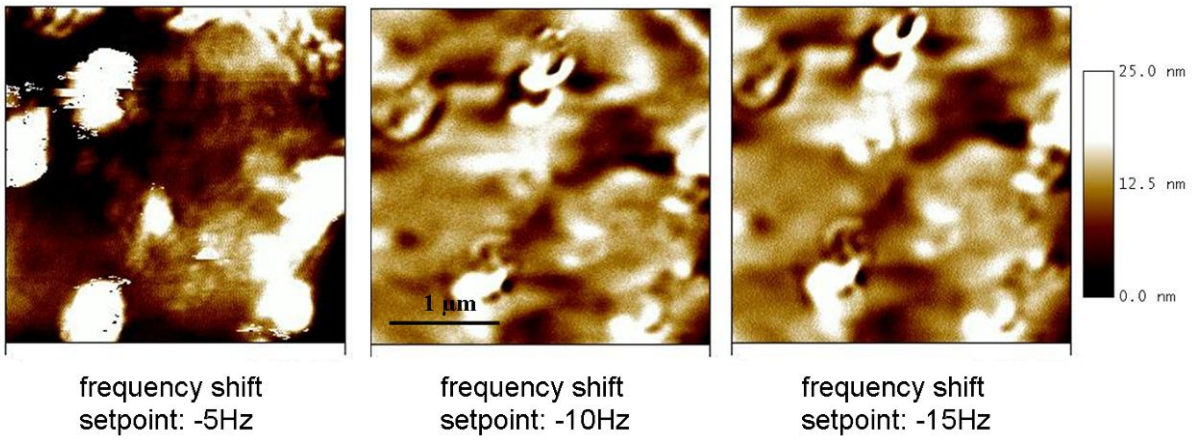

Fig. 3.14 Preliminary NC-AFM images of epitaxial graphene on SiC in function of three different frequency shift setpoints. Pr/Ir coated Si tip has been used.

The frequency to voltage converting factor K_{fv} is a parameter defined by the following relation:

$$\left(\Delta f_0 - \Delta f_{0,set}\right)[\mathrm{V}] = \frac{1}{K_{fv}} \times \left(\Delta f_0 - \Delta f_{0,set}\right)[\mathrm{Hz}] \qquad (3.7)$$

Put into words, this parameter allows the value $\Delta f_0 - \Delta f_{0,set}$ to be converted from hertz to volts. It is worth noting that the frequency shift difference expressed in volts is inversely proportional to K_{fv} and therefore high value of K_{fv} leads to small value of the output. The Fig. 3.15 shows the influence of different K_{fv} on NC-AFM images. A highly oriented pyrolitic graphite (HOPG) sample and a Pt/Ir coated Si tip have been used. No obvious influences are visible on the topography image when the factor K_{fv} increases. However, we can notice a significant decrease of the rms roughness on the frequency shift difference $\Delta f_0 - \Delta f_{0,set}$ image when the factor K_{fv} increases. As expected, the noise level of the frequency shift difference signal is enhanced when the converting factor K_{fv} is decreased, which results in an increase of the rms roughness of the amplitude signal. However, this does not mean that a high converting factor gives a better topography image. In practice, a high value setting leads to a low output voltage of frequency shift difference. Consequently, with the same PI gains, the reaction of the z piezo would be less abrupt and it produces a more "flat" topography image.

In NC-AFM imaging, the oscillation amplitude of the cantilever is generally one order smaller than in Tapping™ mode to keep the tip moving in attractive force region. [76,100]

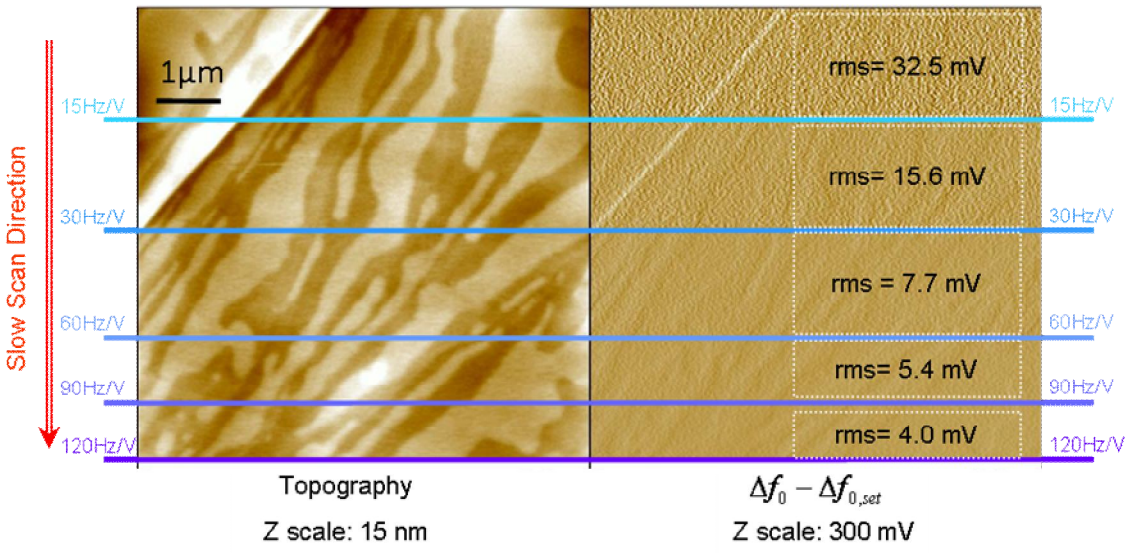

Fig. 3.15 NC-AFM imaging on HOPG sample realized for different converting factors K_{fv}. A Pt/Ir coated Si and a frequency shift setpoint of -20 Hz have been used. The rms roughness is indicated on each image.

In Fig. 3.16, cantilever oscillation amplitudes in the range of 1 nm to 8 nm have been tested on HOPG sample with a Pt/Ir coated Si tip. It is worth noticing, that for the sake of safety, it is impossible on the EnviroScope™ to engage the tip with oscillation amplitude smaller than 3 nm, this value is locked by the Nanoscope Software. This limit corresponds to a minimum amplitude signal of 0.1 V and cannot be modified in the Nanoscope software. In practice, to get around this limitation, the tip is engaged with this minimum amplitude of 3 nm and then the amplitude is reduced to a lower value (down to 1 nm). As we can see in Fig. 3.16, both in the topography and the frequency shift difference $\Delta f_0 - \Delta f_{0,set}$ images, the noise level is clearly visible for sub-3 nm amplitude values. Both 4 nm and 8 nm amplitudes provide less noisy images. The corresponding rms roughnesses are indicated in Fig. 3.16.

The NC-AFM works in the attractive region of the van de Waals force, which results in a non linear decrease of the frequency shift Δf_0 as the tip approaches the sample [28] and, for a fixed amplitude of oscillation, the smaller the tip-sample distance is, the larger the frequency shift is (see Fig. 3.17). If a frequency shift setpoint $\Delta f_{0,set}$ is set to a value greater than the one of the turning-point, the tip will keep on approaching the surface and will finally crash.

The Fig. 3.18(a) shows a topography image, in which the frequency shift setpoint $\Delta f_{0,set}$ has been changed from -10 Hz to -60 Hz. This image is done on a freshly cleaved HOPG sample. The slow scan direction is from the top to the bottom. Within the region scanned with a frequency shift setpoint of -10 Hz, some irregular features are visible.

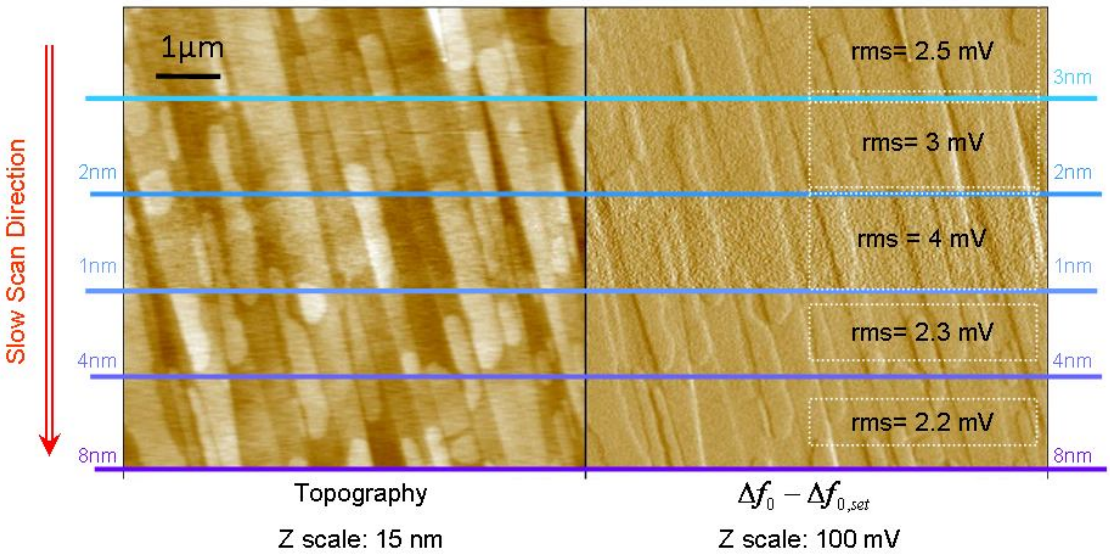

Fig. 3.16 Non-contact AFM imaging on HOPG sample realized with oscillation amplitudes in the range of 1 to 8 nm. A Pt/Ir coated Si and a frequency shift setpoint of -5Hz have been used. The rms roughness is indicated on each image.

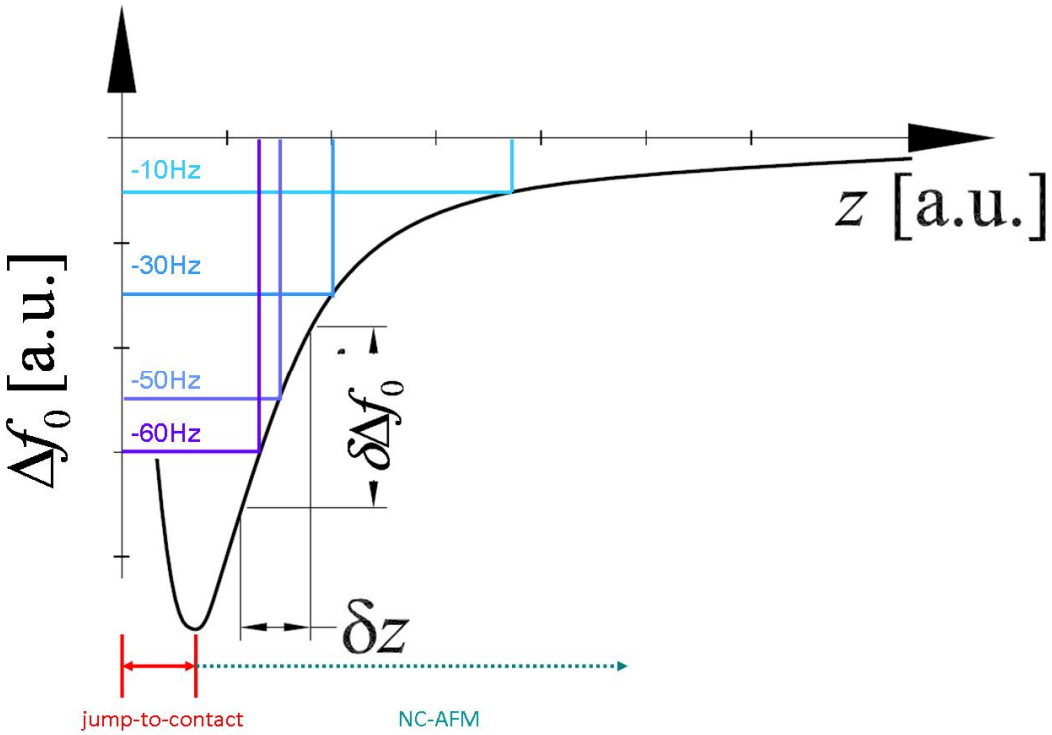

Fig. 3.17 Schematic plot of the frequency shift Δf_0 as a function of the z tip-sample distance. The is extracted from the reference [25] and modified.

As the frequency shift setpoint is increased, the irregular features disappear and topography steps between graphite terraces are clearly visible. On Fig. 3.18(b), a complete topographical image at a frequency shift setpoint of -20 Hz is shown on the same area and is used as a reference. In spite of a strong vertical drift, we can distinguish the same features. Some of them are evidenced by a colored frame. Within the red and the orange frames, the irregular features are more contrasted when larger tip-sample distance are used. Within the yellow frames, the features are equally contrasted when the same tip-sample distance is used but the contrast almost disappears for smaller distance.

On Fig. 3.18(a), within the green box, begins to show the graphite step while the one on Fig. 3.18(b) only shows irregular features. As the electrostatic force can spread out over a range of tens to hundreds of nanometers, [5,101,102] for large tip-sample distances, the tip senses more the electrostatic force than the short range van der Waals force. Then, the irregular features are more representative of the electrostatic property of the sample surface. As the tip approaches the sample surface, the van der Waals force increases much faster than the electrostatic force and eventually overpasses the electrostatic force. When the van der Waals force is dominant topography details, such as graphite steps, can be revealed and the irregular features disappear.

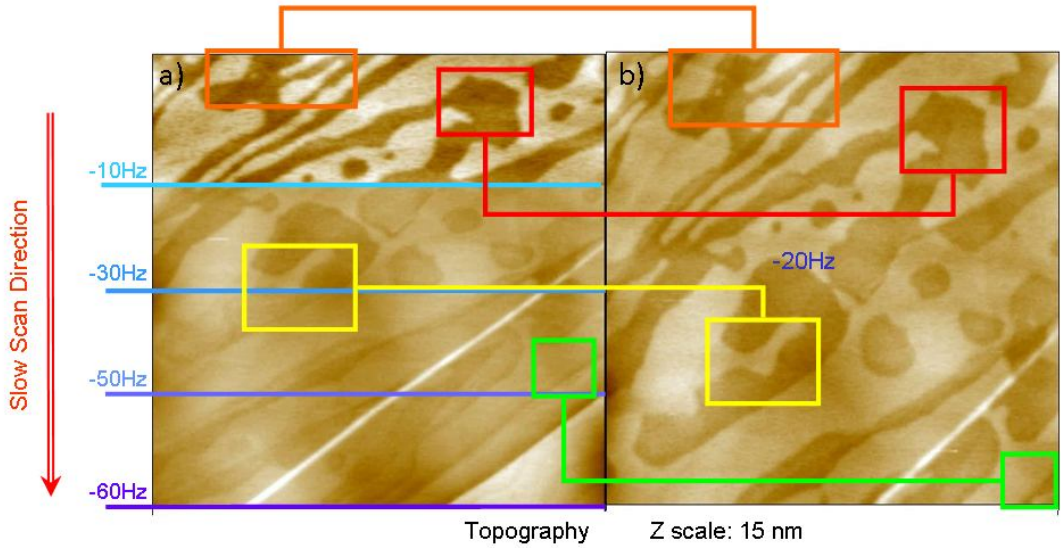

Fig. 3.18 (a): Topography image in non-contact imaging mode on a freshly cleaved HOPG sample realized at different frequency shift setpoint: -10 Hz, -30 Hz, -50 Hz and -60 Hz. (b) Topography image of the same area at -20 Hz frequency shift setpoint. Squares in same color indicate the same region of sample. The imaging experiments are done with Pr/Ir coated silicon tip with oscillation amplitude of 4 nm.

3.3 Optimization of KFM measurement under secondary vacuum

In this section, we present the development of the KFM operating under secondary vacuum. More specifically, we discuss the work done to optimize the KFM measurement using both amplitude modulation (AM-KFM) and frequency modulation (FM-KFM) modes.

3.3.1 System connections

The general implementation of KFM measurement on EnviroScope™ is presented in Fig. 3.19. The sample is placed on a grounded sample plate and the $V_{ac}\sin\omega_{el}t + V_{dc}$ voltage is sent directly to the tip [see Fig. 3.20(a)]. Two different modes of KFM are presented separately:

- In AM-KFM, which is based on force sensitive detection, ω_{el} is commonly set to the second resonance of the cantilever in order to separate the topography measurement of the surface potential measurement. Due to the contact potential difference V_{CPD} between the tip and the sample, the cantilever has a resulting oscillation at ω_{el}. A dc bias voltage V_{dc} is sent to the tip and adjusted in real-time until the oscillation amplitude at ω_{el} is nullified. In this case, the V_{dc} value is equal to the CPD.

– In FM-KFM, which is based on force gradient sensitive detection, ω_{el} is chosen in a range of several hundred to several thousand Hertz. The FM-KFM method, makes use of the fact that the oscillating electrostatic force gradient leads to a modulation of the resonant frequency ω_0 of the cantilever, giving rise to a sideband at $\omega_0 + \omega_{el}$. Demodulation by a lock-in technique of the frequency shift signal Δf_0 at ω_{el} frequency delivers a signal that is proportional to the force gradient rather than the force. This signal is then nullified by adjusting the dc bias voltage V_{dc}.

In both techniques, the resulting V_{dc} gives the KFM image. Before imaging the surface potential of the sample, a V_{dc} bias sweep analysis is systematically done in order to check the behavior of the oscillation amplitude at ω_{el}, which is related to the electrostatic force. This analysis is performed very close to the sample surface to ensure a good probing of the electrostatic force. In practice, this bias sweep is done while the z feedback is on. In Fig. 3.20(b), a typical bias sweep is shown with a standard connection via the SAM 1 (see Fig. 3.3). The electrical driving signal $V_{ac}\sin\omega_{el}t + V_{dc}$ from Nanonis feeds to the ANA2 input

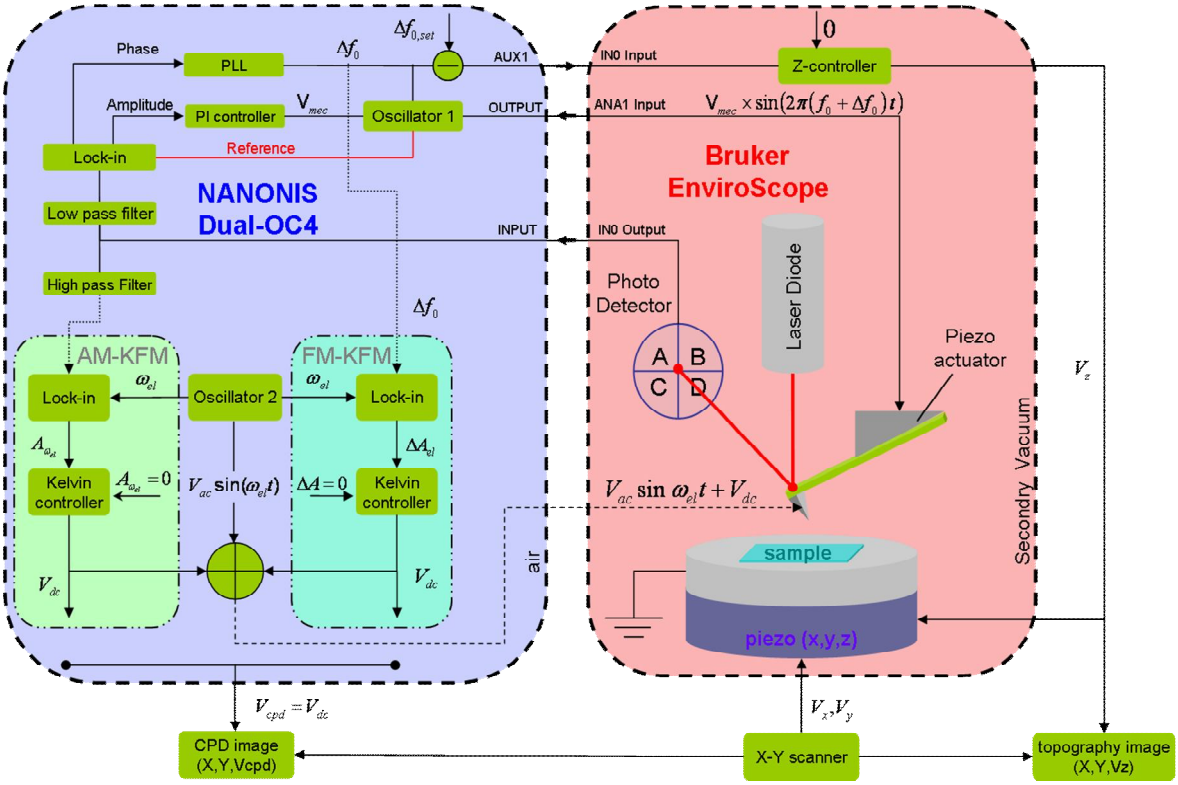

Fig. 3.19 Detailed setup of KFM loop (in both AM and FM modes) under 2nd vacuum. Nanonis electronics and EnviroScope™ are respectively represented in the blue part and red part. Details are given in the text.

of SAM 1 box, which connects electrically the tip. As we can see, the measured oscillation amplitude at ω_{el} is very noisy and does not reach zero when V_{dc} equals V_{CPD}. We suppose that this phenomenon is mainly induced by crosstalk in the electrical lines of the Veeco electronic. Indeed, both low and high voltage cables are integrated into one cable between SAM box and microscope. Under secondary vacuum, the amplitude of the ac voltage V_{ac} is often one order smaller than under ambient atmosphere. The V_{ac} is typically in the range of 1 mV to 1 V, which is likely to suffer from crosstalk from high voltage cables. In order to overcome this problem, homemade connection has been developed. The electrical driving signal $V_{ac}\sin\omega_{el}t + V_{dc}$ provided by the Nanonis electronic feeds directly to the tip via a vacuum feedthrough, which has been fixed on one of the chamber wall.

A SSRM tip holder[6] is used in order to have a direct electrical connection to the tip inside the vacuum chamber. Moreover, a piece of glass electrically isolates the sample from the sample holder connected to the ground of the Nanonis electronics [red wire in Fig. 3.20(a)]. The resulting bias sweep curve obtained with this connection can be seen in Fig. 3.20(c). As we can observe, the noise level is very low and the electrical oscillation amplitude reaches zero when V_{dc} is equal to V_{CPD}.

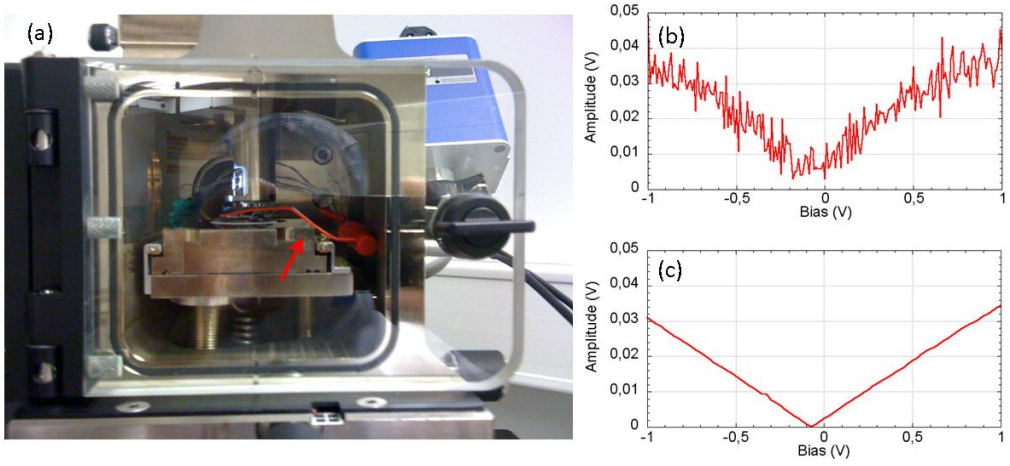

Fig. 3.20(a) Homemade connection realized via a vacuum feedthrough. The sample is insulated from the sample stage with a piece of glass and is connected to the red wire (as indicated) which is finally conducted to outside BNC cable. Bias sweep acquisition is shown when the electrical driving signal $V_{ac}\sin\omega_{el}t + V_{dc}$ feeds via the SAM 1 via the ANA1 input (b) or feeds directly to the tip (c). Experiment is done with Pr/Ir coated silicon tip on HOPG with oscillation amplitude of 10nm. The frequency shift septoint is fixed to -35 Hz.

[6] More details can be found in Chapter 2.

3.3.2 Kelvin controller adjustment

As presented in the previous section, the electrical oscillation amplitude $A_{\omega_{el}}$ is nullified when V_{dc} voltage equals V_{CPD}. Thus, in order to map the sample surface potential, the V_{dc} bias voltage is adjusted while imaging, to nullify the electrostatic force. The $X_{\omega_{el}}$ component representing the electrical oscillation signal as a vector relative to the lock-in reference oscillator is preferred as feedback signal because of the monotonic variation. As shown in Fig. 3.21, the minimum oscillation amplitude of the cantilever is found by searching $X_{\omega_{el}} = 0$.

In the next step, the procedure to set the proportional-integral (PI) controller parameters is described. Instead of optimizing the PI gain of the Kelvin controller as well as the bandwidth of the lock-in amplifier while scanning, a pre-optimization in static mode is done using the power spectral density (PSD) of the V_{dc} signal versus the frequency.

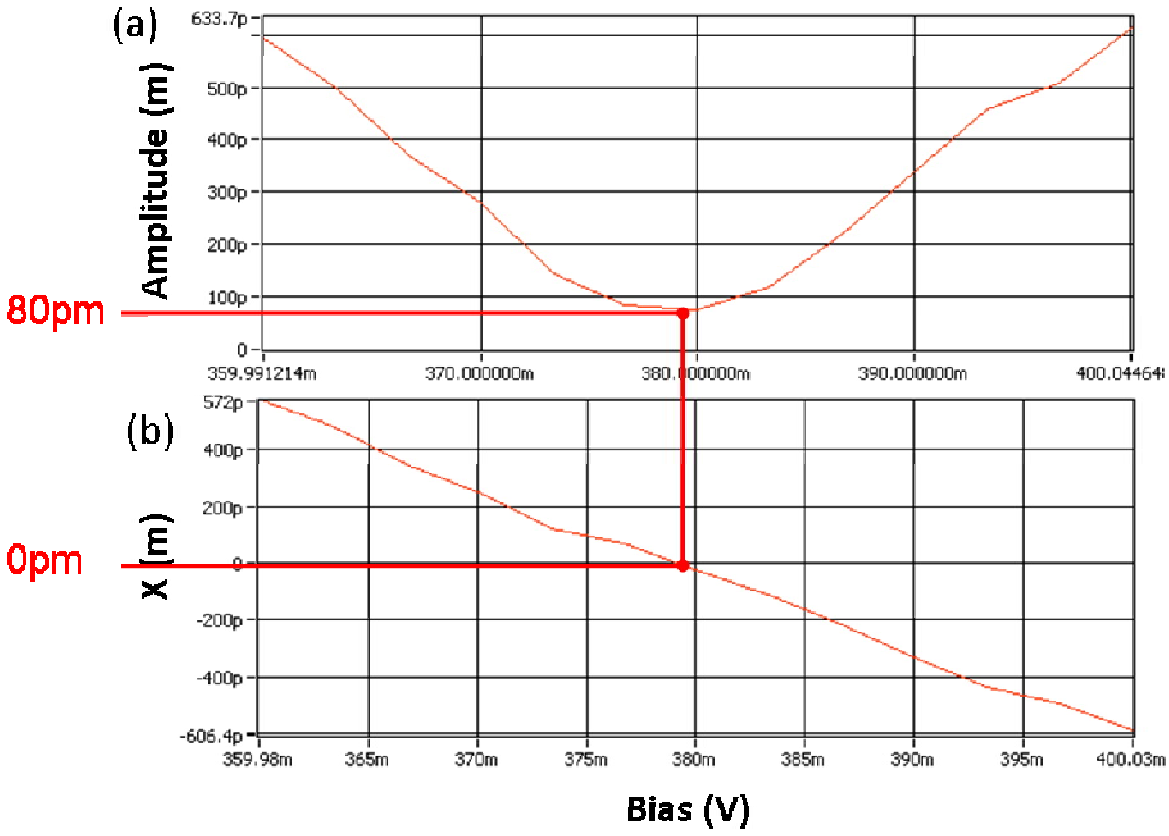

Fig. 3.21 (a) Oscillation amplitude $A_{\omega_{el}}$ electrostatically excited against V_{dc}. (b) Corresponding component $X_{\omega_{el}}$ representing the electrical oscillation signal as a vector relative to the lock-in reference oscillator. Experiment is done with a Pr/Ir coated silicon tip on HOPG with oscillation amplitude of 10 nm. Frequency shift setpoint is set to -35 Hz.

PSD allows the noise level to be finely adjusted while tuning the PI gains and the bandwidth. In Fig. 3.22(a), a typical PSD of the V_{dc} signal (in red) before optimization is presented. On this plot we can see a background noise level around 10 µV·Hz$^{-1/2}$ above the bandwidth (defined here at 500 Hz) as well as two peaks at about 50 Hz and 310 Hz. As the normal scan rate is 0.4 Hz (1024 points), these two peaks generate periodic patterns on the surface potential image (not shown here). After optimization of the PI gains and adjustment of the bandwidth, we conclude from the yellow curve that the background noise level is reduced by one order of magnitude (~1 µV·Hz$^{-1/2}$) above the bandwidth (defined here at 500 Hz) and the 50 Hz peak is smoothed. In the Nanonis controller, the user can choose to adjust the proportional and integral gains (P/I) or the proportional gain and the time constant (P/T).

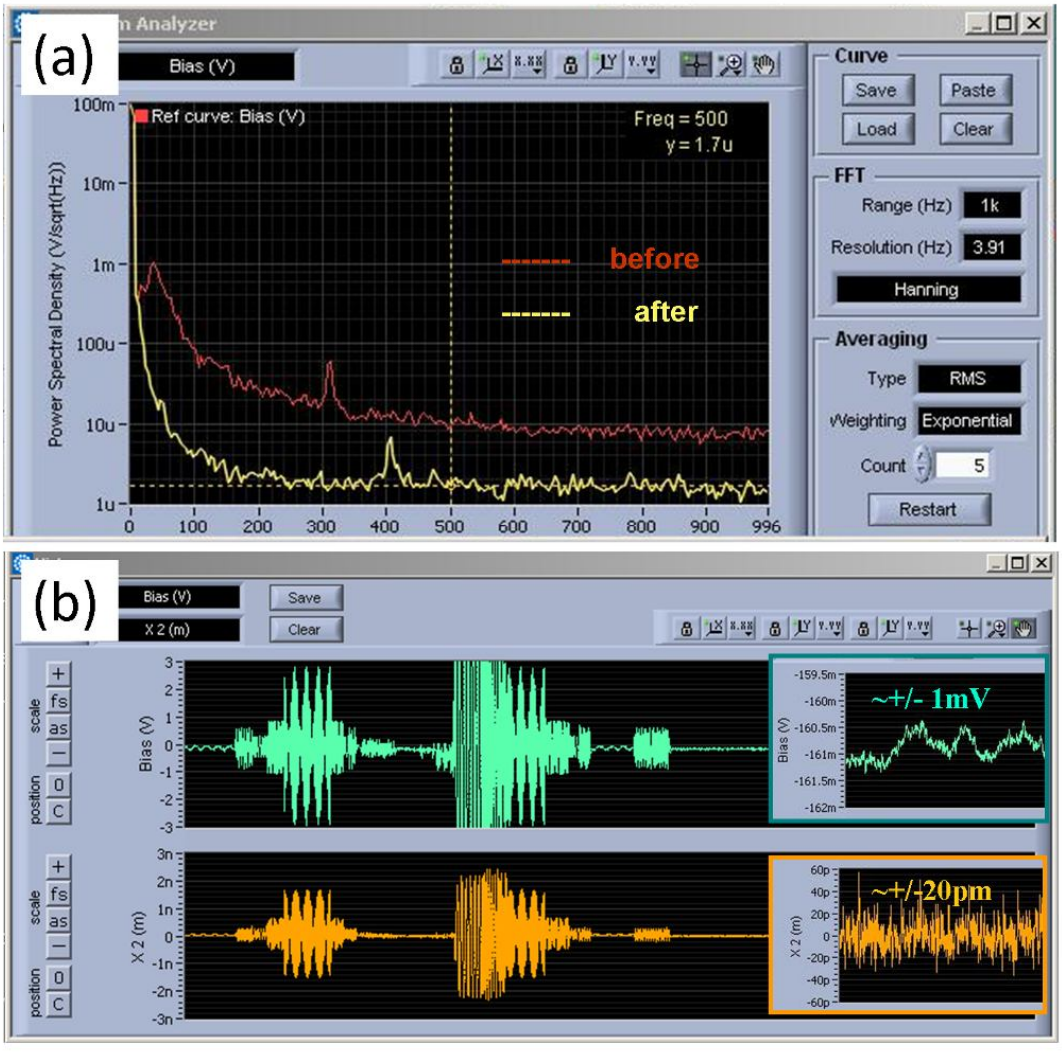

Fig. 3.22 Parameters such as proportional gain, time constant and bandwidth can have direct influence on (a) bias spectrum and (b) noise level of X and bias. After our optimization, the dc bias component can be 5 orders higher than background noise. The bias noise is about 1 mV and the X noise is about 20 pm.

The integral gain and time constant are related as follows:

$$I = \frac{P}{T}. \tag{3.8}$$

This couple of gains (P/I or P/T) gains are adjustable over a wide range (more than 20 orders). The dc output voltage provided by the PI controller is proportional to the error $e(t)$ and the integral of the error $e(t)$ as follows:

$$V_{dc}(t) = Pe(t) + I\int_0^T e(\tau)d\tau = Pe(t) + \frac{P}{T}\int_0^T e(\tau)d\tau, \tag{3.9}$$

where *e(t)* is the difference between real-time component $X_{\omega_{el}}$ and the setpoint fixed at zero to nullify the electrostatic force. A high P gain results in a large change in the output V_{dc} for a given change in the error *e(t)*. If the P gain is too high, the loop becomes unstable and the noise level is also increased. In contrast, a small gain results in a small output response to a large input error, and a less responsive or less sensitive controller. If the proportional gain is too low, the control action may be too small when responding to system disturbances. Typical values in the range between 1 and 100 V/m has been determined as good imaging conditions. The contribution from the integral term is proportional to both the magnitude and the duration of the error *e(t)*. In other words, the integral term in Eq. (3.9) is the sum of the instantaneous error *e(t)* over time and gives the accumulated offset that should have been corrected previously. A low time constant setting improves the response speed of the system towards the setpoint value and eliminates the residual steady-state error. However, since the integral term responds to accumulated errors from the past, it can bring about overshoot of the setpoint value. In practice, we put this value less than the time needs for each pixel to make sure that averaging effects are present. As an example, the temporal response of the V_{dc} as well as the error signal *e(t)* are represented in Fig. 3.22(b), while the P gain and time constant T are adjusted. As we can see, the noise level can be significantly reduced, down to 1 mV for the V_{dc} signal and 0.2 mV (calibration value of 100 nm/V applied) for the error signal *e(t)*.

3.3.3 KFM imaging under secondary vacuum

After an optimization of all the operating parameters, the KFM imaging is working under secondary vacuum. Depending on force sensitive or gradient force sensitive detection, two mains KFM techniques can be defined: amplitude modulation (AM) or frequency modulation (FM). In the next part, the results of the two techniques are described.

3.3.3.1 AM-KFM results

In our system under secondary vacuum, the fundamental frequency (or first eigenmode) of the cantilever (around 65 kHz) is always used for topography measurement in non-contact mode. For AM-KFM, the tip is electrostatically excited at the second eigenmode of the cantilever (around 365 kHz) by applying a driving signal $V_{ac}\sin\omega_{el}t + V_{dc}$. Due to the CPD between the tip and the sample, the cantilever is driven in oscillation by a periodic electrostatic force. By sending a dc signal to tip, the electrical oscillation can be nullified when the following condition is satisfied: $V_{dc}=V_{CPD}$.

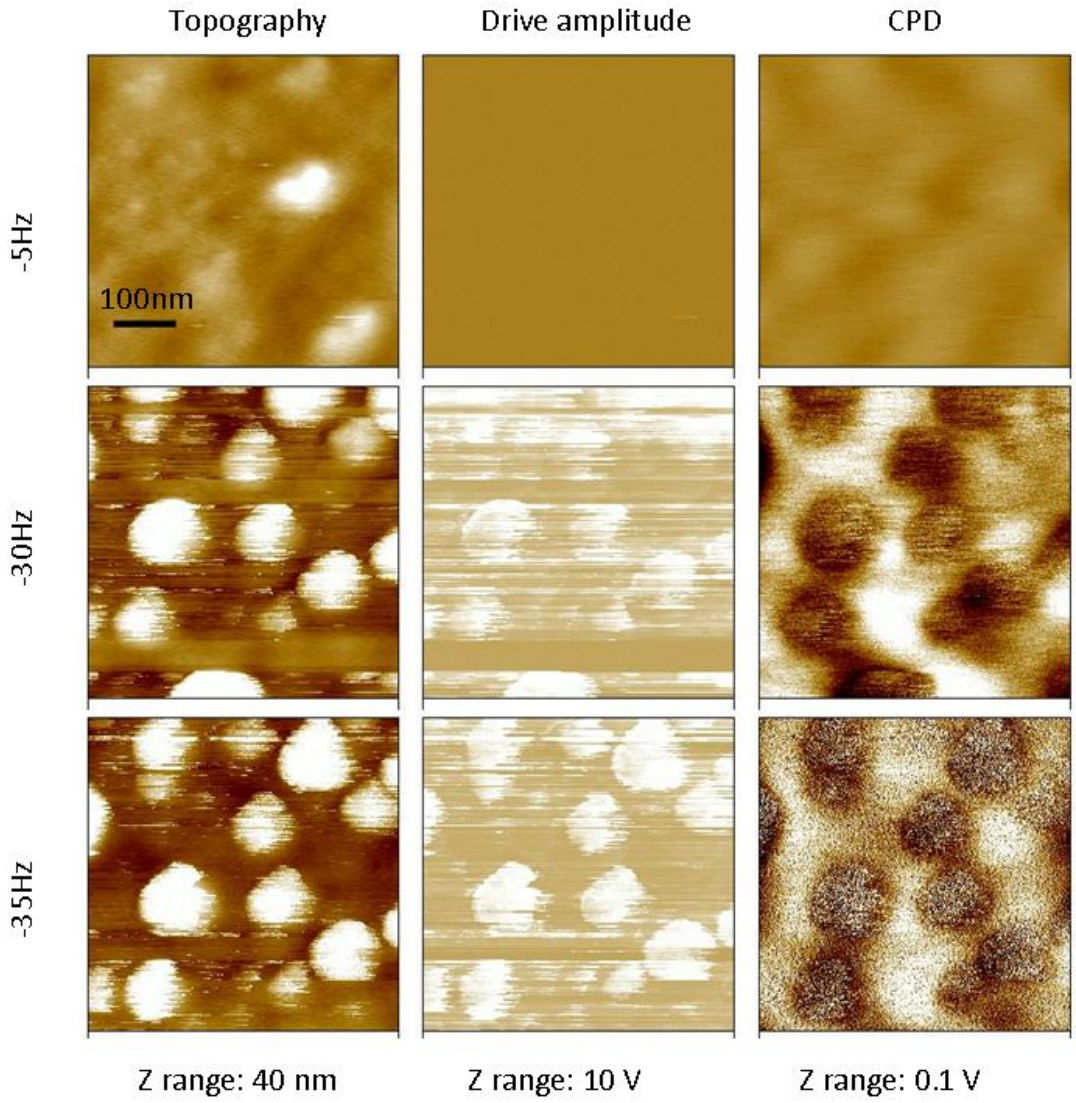

Fig. 3.23 First AM-KFM images on platinum sample under secondary vacuum with different frequency shift setpoints as indicated in the figure. Three channels are collected: topography, mechanical drive amplitude and the CPD. The same type of data with different frequency shift setpoints has the same z scale. Pr/Ir coated Si tip has been used. Experimental parameters: *A*= 8 nm, *V_{ac}*= 50 mV*.

In Fig. 3.23, the first KFM images can be seen where three frequency shift setpoints are set. Topography, mechanical driving amplitude as well as CPD channels are mapped. With a frequency shift of -5Hz the topography is not clear as the tip-sample distance is too large and the short range van der Waals force influence is very limited. However, topography is significantly improved by working with a frequency shift of -30 Hz and -35 Hz because the tip-sample distance is smaller. In both cases, dots on the platinum surface are clearly visible, which could be some contamination or aging effect on the 5-year old sample. Similarly, the V_{DC} mapping is also significantly improved with -30 Hz and -35 Hz settings. While scanning, the mechanical drive amplitude V_{exc} has been mapped (see Fig. 3.23).

For -30 Hz and -35 Hz settings, large variations of the drive amplitude are seen over the dots, which means the feedback loop is not perfectly adjusted. The CPD contrast in -30 Hz and -35 Hz is possibly due to the capacity gradient change in the topography and not well controlled tip-sample distance. In order to eliminate the topography artefacts, a flat sample with low roughness is needed.

Other imaging tests have been done on a chemical mechanical polished (CMP) polycrystalline copper sample, which presents a flat surface (rms roughness about 4.2 nm) and exhibits work function variations due to different orientation of grains. Typical topography and surface potential mappings are presented in Fig. 3.24. During the experiment, a mechanical oscillation of 8 nm and a frequency shift setpoint of -25 Hz are

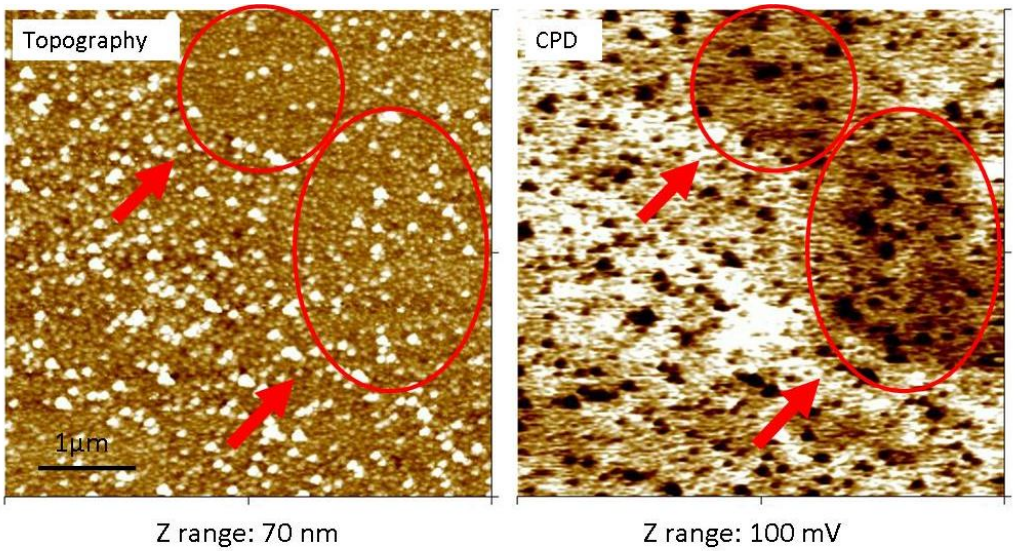

Fig. 3.24 AM-KFM images on polished polycrystalline Cu sample. Dots visible on topography image are probably induced oxidation of the surface (CuO). The CPD contrast shows work function variations between copper grains as indicated in red circles. Pt/Ir coated Si tip is used for the experiment. Experimental parameters: *A= 8 nm, V_{ac}= 100 mV, Δf_0= -25 Hz, f_0= 71* kHz and *f_{el}= 442* kHz.

used for stable NC-AFM imaging (see Fig. 3.16). The V_{ac} amplitude for the electrical oscillation is set to 100 mV. The influence of this parameter will be discussed later. The copper is very reactive to the oxygen present in air and as we can see, the topography image shows some oxidized dots CuO on the flat and homogeneous surface. In the CPD image, the CuO dots present a darkest contrast related to a work function. Work function differences of different grains can be also distinguished on the CPD image. In the red circle, two obvious contrasts are visible without sudden variations in the topography image. This two images show the system has the capability to work in AM-KFM.

3.3.3.2 FM-KFM results

In this work, KFM in FM mode has been also developed. Unlike AM-KFM, FM-KFM is based on force gradient sensitive detection. An electrical driving signal $V_{ac}\sin\omega_{el}t + V_{dc}$, where the ω_{el} frequency is chosen in a range between several hundred to several thousand hertz, is sent to the tip which results to a modulation of the mechanical phase. In other words, this method makes use of the fact that an oscillating electrostatic force gradient leads to a modulation of the resonant frequency ω_0 of the cantilever, giving rise to a sideband at $\omega_0 + \omega_{el}$. The resulting amplitude modulation in the frequency shift signal Δf_0 (see Fig. 3.19) is demodulated by a lock-in amplifier at ω_{el} frequency and delivers a signal that is proportional to the electrostatic force gradient. Finally, the Kelvin controller(see section 3.3.2) nullify the component $X_{\omega_{el}}$ in order to reach the V_{CPD}. [46,72]

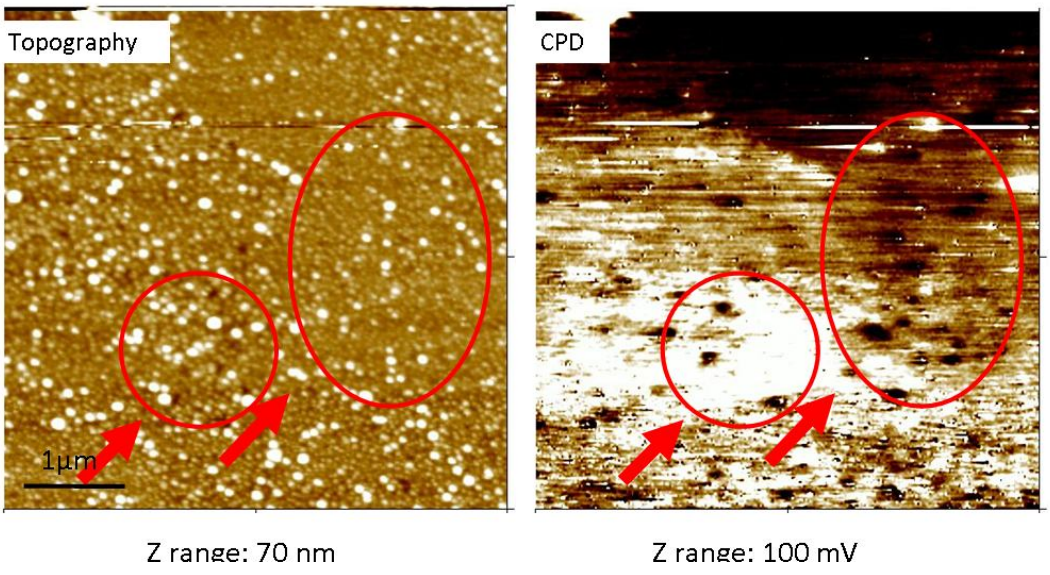

Fig. 3.25 FM-KFM on polished polycrystalline Cu sample. Dots visible on topography image are probably induced oxidation of the surface (CuO). Pt/Ir coated Si tip is used for the experiment. Experimental parameters: *A= 8 nm*, V_{ac}*= 1 V*, Δf_0*= -25 Hz*, f_0*= 71* kHz and f_{el}*= 1* kHz.

The FM-KFM is much more difficult to operate than AM-KFM. However, a higher contrast is expected due to low averaging effects (see details in chapter 1, section 0). Fig. 3.25 shows FM-KFM image obtained on the previous CMP polycrystalline copper sample. During the experiment, the oscillation amplitude and the frequency shift are set respectively to 8 nm and -25 Hz. The V_{ac} and the frequency ω_{el} are set to respectively 1 V and 1 kHz. The influence of theses parameters will be discussed later. The topography image shows CuO dots on the sample surface and the CPD mapping shows contrast related to different grain orientations (see the red circle). Comparing with the AM-KFM image (see Fig. 3.24), the CPD image in FM-KFM is really more unstable.

3.3.4 Further optimization and understanding of the parameters

The capability of KFM operating under secondary vacuum in both AM and FM modes has been shown in previous section. A CPD variation correlated to the topography has been evidenced. A question is to know if the CPD contrast is dominated by the capacitance effects. This part presents a KFM study done on a very flat surface sample. Then the influence of some experimental parameters on AM-KFM imaging is discussed.

3.3.4.1 HOPG as a reference sample

To achieve this goal, a flat sample is needed to diminish the topography influence on CPD mapping. In addition, the sample must be easily refreshed to avoid contamination which can induce abrupt change in topography. Among different choices, highly ordered pyrolytic graphite (HOPG) has been chosen due to its flatness (with steps less than 10 nm over a 10 µm scan) and to its ability to be refreshed easily with the scotch method.

HOPG sample from SPI Supplies (West Chester, USA) with ZYH grade has been chosen[7]. Fig. 3.26 shows a typical topography and corresponding AM-KFM images obtained under secondary vacuum. The steps between graphite terraces are clearly seen on the topography image. In the CPD mapping [Fig. 3.26(b)], variations of the work function can be observed even within the same graphite terrace. In Fig. 3.26(c), the red profile shows very clear graphite steps. The green line mainly shows two values of CPD and no link between topography and CPD can be found.

[7] The "mosaic spread" term defines the grade or the perfectness of HOPG. This term originates from X-ray crystallography. HOPG samples are polycrystals and looks like mosaic of microscopic monocrystal grains slightly disoriented with respect to each other. There are several grades of HOPG. Notations developed by Advanced Ceramics Corporation, the leading company in HOPG production are used. The ZYH Grade has a mosaic spread of 3.5°±1.5°. The grain size is in the range of 30-40 nm.

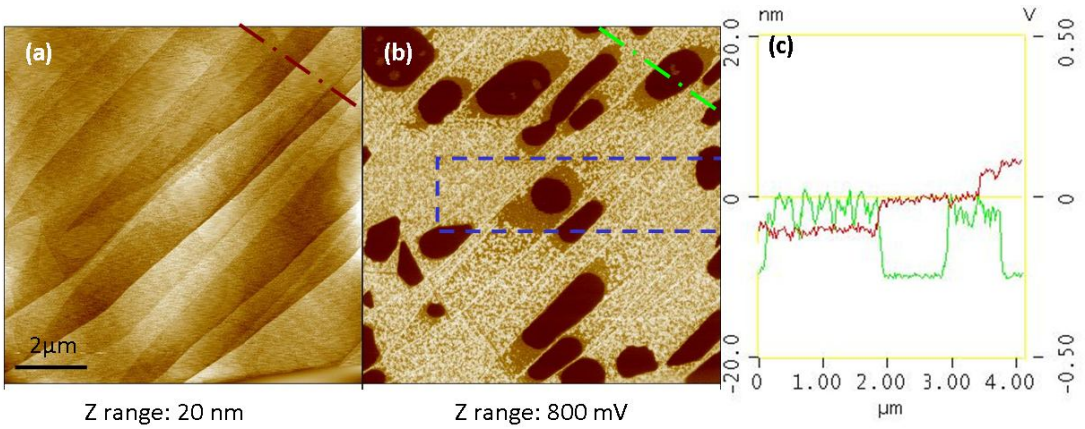

Fig. 3.26 AM-KFM imaging on HOPG sample under secondary vacuum. (a) Topography, (b) CPD, and (c) cross section on indicated location (red and green). The blue box indicates the KFM area shown in Fig. 3.29. Pr/Ir coated Si tip is used. Experimental parameters: A= 5 nm, V_{ac}= 300 mV, Δf_0= -60 Hz, f_0= 67 kHz and f_{el}= 427 kHz.

XPS experiments were performed on the HOPG surface to investigate the chemical composition of the "patch" observed on CPD image. Measurements were carried out with a monochromated AlKα source (hv = 1486.6 eV). Photoelectrons were collected at a take-off angle of 35° with respect to the sample surface, yielding to a sampling depth of 5 nm and an energy resolution of 0.7 eV. Results are shown in Fig. 3.27. As expected, the survey spectrum exhibits carbon and oxygen characteristic peaks (C1s and O1s). The charging effect is estimated via the shift observed on the C1s peak (1.4 eV), compared to the referenced value of 284.7 eV for hydrocarbon contamination. [103,104] The oxygen (O1s) and tin (Sn $3d_{5/2}$) peaks are corrected from this energy offset. The O1s binding energy is

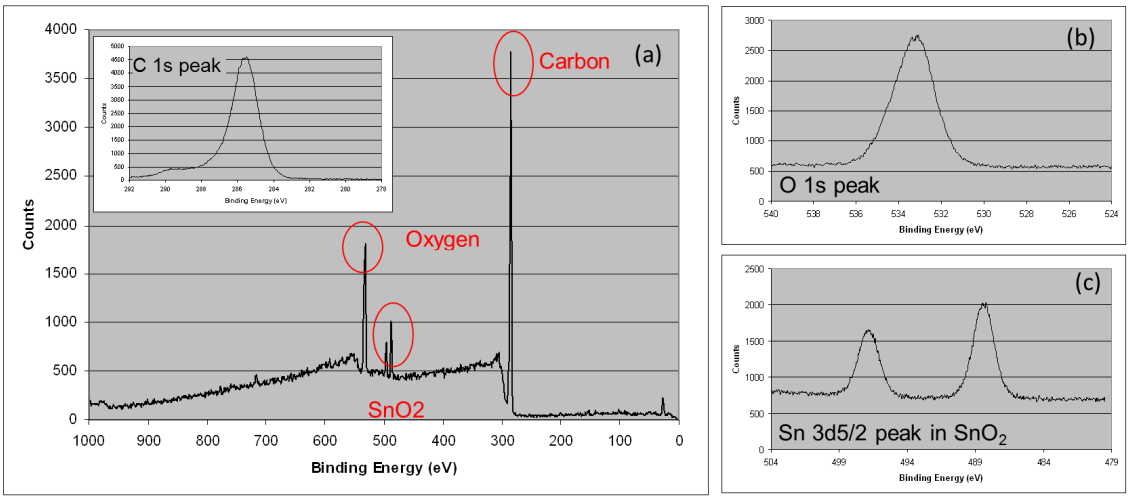

Fig. 3.27 XPS results on the HOPG after wire soldering [red wire in Fig. 3.20 (a)]. Full spectrum (b) high resolution oxygen peak (c) high resolution Sn peak.

531.8 eV and matches with the referenced value of 531 eV for SnO_2. This is consistent with the Sn $3d_{5/2}$ peak position found at 486.8eV, corresponding to the referenced position of 486.7eV for SnO_2. Some contamination is presumably introduced during wire soldering [red wire in Fig. 3.20(a)]. As a consequence, the presence of this SnO_2 "patch" inside the HOPG sample explains the surface potential variation observed in Fig 3.27.

3.3.4.2 Effect of the frequency shift setpoint on KFM imaging

In order to increase the spatial resolution, the use of large frequency shift is necessary. As we discussed previously, a more negative frequency shift reduces the tip-sample distance (see Fig. 3.17) and so higher spatial resolution is expected. As a consequence, the optimization of the frequency shift setpoint parameter has been performed on HOPG sample, which presents a very flat surface and a high CPD contrast, as shown in Fig. 3.28.

In this part, we firstly present the influence of the factor K_{fv} [see Eq. (3.7)], which converts the frequency shift difference between the real-time value and the setpoint into

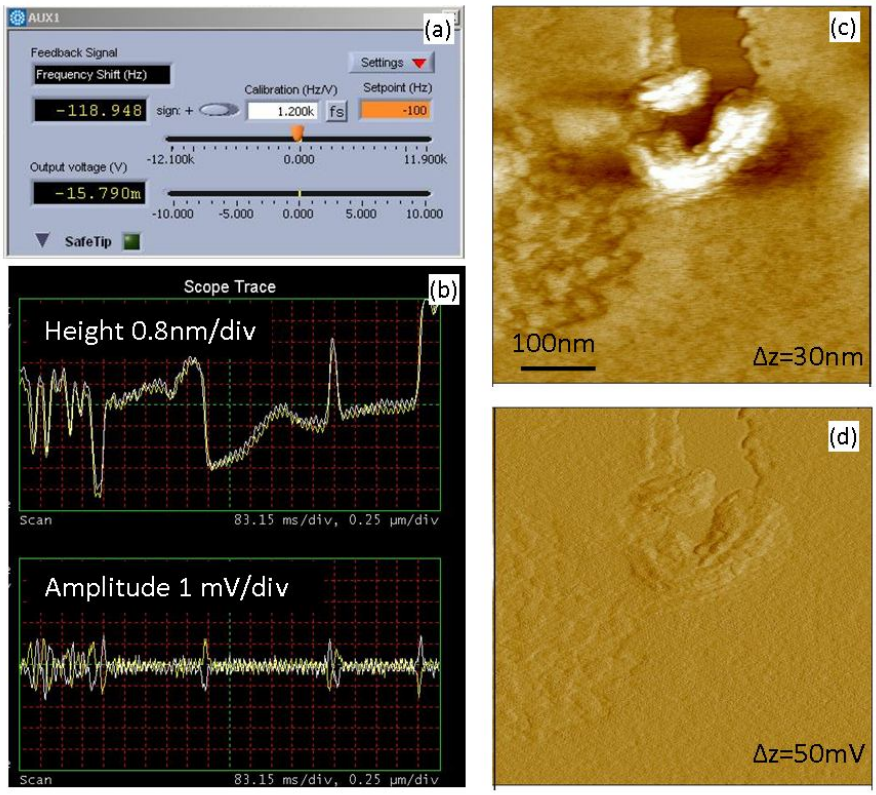

Fig. 3.28 (a) Overview of the window in the Nanonis software, which allow to parameter the K_{fv} factor. The output voltage $\Delta f_0 - \Delta f_{0,set}$ is inversely proportional to this factor. (b) Overview of the scope window in the Nanoscope V5.3 software showing that trace and retrace curves matches well even with a -180 Hz frequency shift setpoint. (c) Topography of HOPG sample with frequency shift setpoint of -300Hz and the corresponding $\Delta f_0 - \Delta f_{0,set}$ image in (d).

volt (see Fig. 3.28(a)). In previous experiments (see Fig. 3.18), this value was set to 30 Hz/V. Here, value up to 1000 Hz/V has been used, which results in a low variation of the $\Delta f_0 - \Delta f_{0,set}$ feedback signal when an abrupt change occurs. In this case, the z-piezo is more stable and the tip crash chance is tremendously reduced. For example, stable imaging can be performed at -180 Hz using a scan rate of 0.5 Hz (the san rate effect is discussed in section 3.3.4.3) on HOPG sample [as in Fig. 3.28(b)]. However, by changing the K_{fv} factor, the I and P gains need to be adjusted. Figs. 3.28(c) and (d) show respectively topographical and $\Delta f_0 - \Delta f_{0,set}$ images with a frequency shift setpoint of -300 Hz, which results in observation of fine features on HOPG.

By adjusting the K_{fv} factor, we demonstrated the possibility to acquire NC-AFM image with frequency shift setpoint value up to -300 Hz. Such frequency shift setpoint value is only accessible if the mechanical oscillation amplitude is properly adjusted. In this part, we observe the impact of the frequency shift setpoint in the range of -5 Hz to -130 Hz regarding to the CPD imaging. The results are presented in Fig. 3.29. By reducing the frequency shift setpoint, the tip-sample separation is reduced, which improves the topography measurement, as previously observed (see Fig. 3.18). As we can see in the topography images in Fig. 3.29, when the tip-sample separation is reduced, the topography images are sharper. The similar trend is also visible for the CPD contrast. The small features visible in the CPD images are also "sharper" as the frequency shift is reduced. This result show qualitatively that imaging closer to the sample surface improves both topographical and CPD resolution.

3.3.4.3 Scan rate comparison

In the Nanoscope software, the scan rate parameter defines the frequency of one line scan. In other words, one over this value gives the time setting for one line scan (including trace and retrace). This parameter can greatly influence the image quality and have to be properly optimized by taking into account the response of the cantilever as well as electronic controller. In Fig. 3.30, AM-KFM imaging under secondary vacuum on HOPG with different scan rates is presented. The results show good stability even with a scan rate of 1.5 Hz. However, more details on topography and CPD images are showed up as scan rate slows done. Both 0.3 Hz and 0.1 Hz scan rate exhibits images with good quality. The red circle marked in Fig. 3.30 shows the lack of retention time behavior in 1.5 Hz scan and the red arrows indicates the 2D artificial "wave" after the abrupt change in CPD.

To understand this result, we consider the time constant defined in Eq. (3.2). In AM-KFM, the second resonant frequency of the cantilever is used for CPD measurement and the quality factor is much lower than this of the fundamental resonance. In results presented in Fig. 3.30, the quality factor Q is about 4800 and the second resonance is

approximaly 427 kHz. According to the Eq. (3.2), the time constant is about 3.5 ms. Therefore, the fast enough usable scan rate is: $SR = \frac{1}{\tau \times 2 \times 512} = 0.27\ \mathrm{Hz}$ (as we have 512

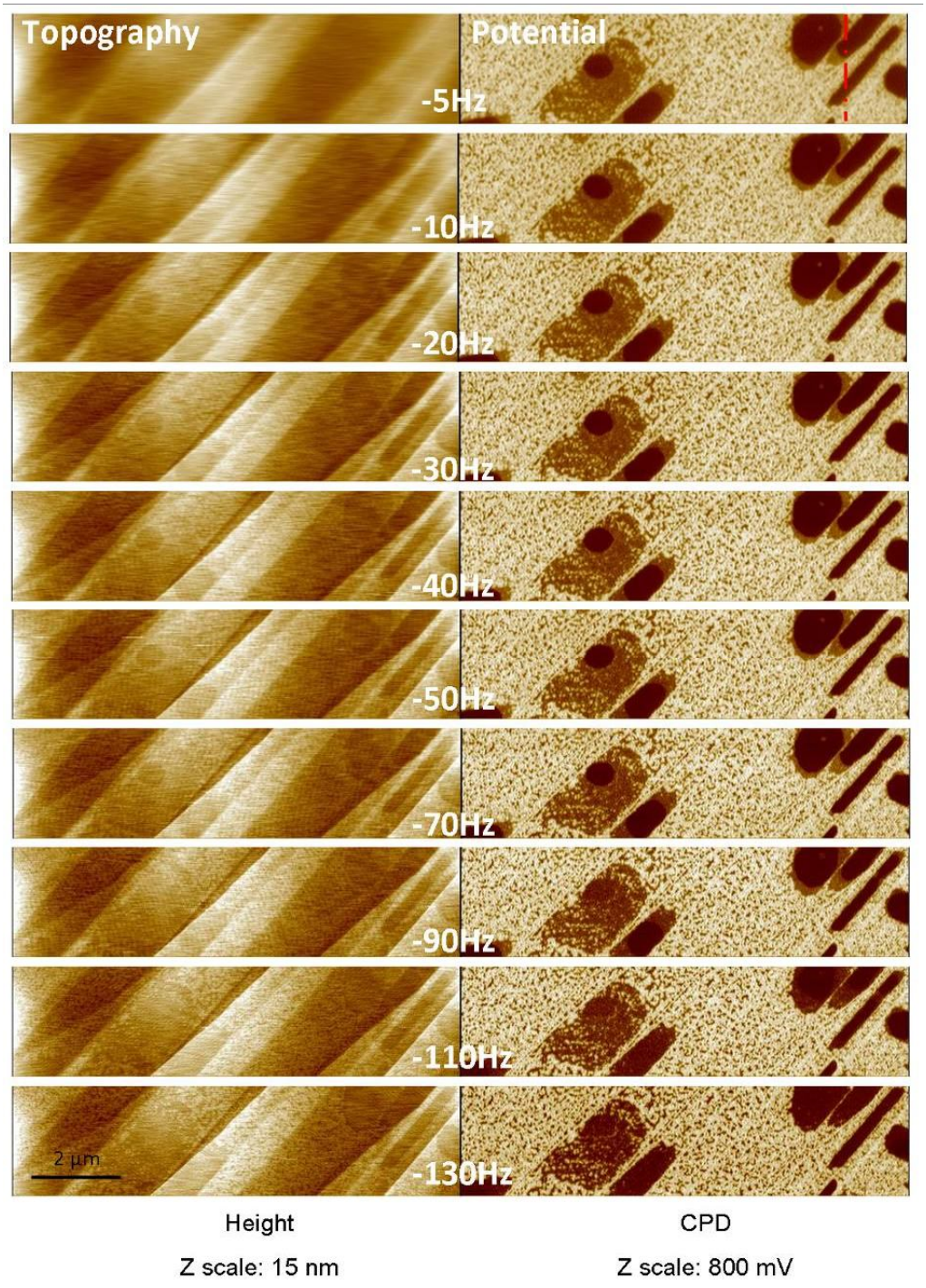

Fig. 3.29 Topography and CPD mapping obtained on the HOPG sample under secondary vacuum for various the frequency shift setpoint, which vary in the range of -5Hz to -130Hz.

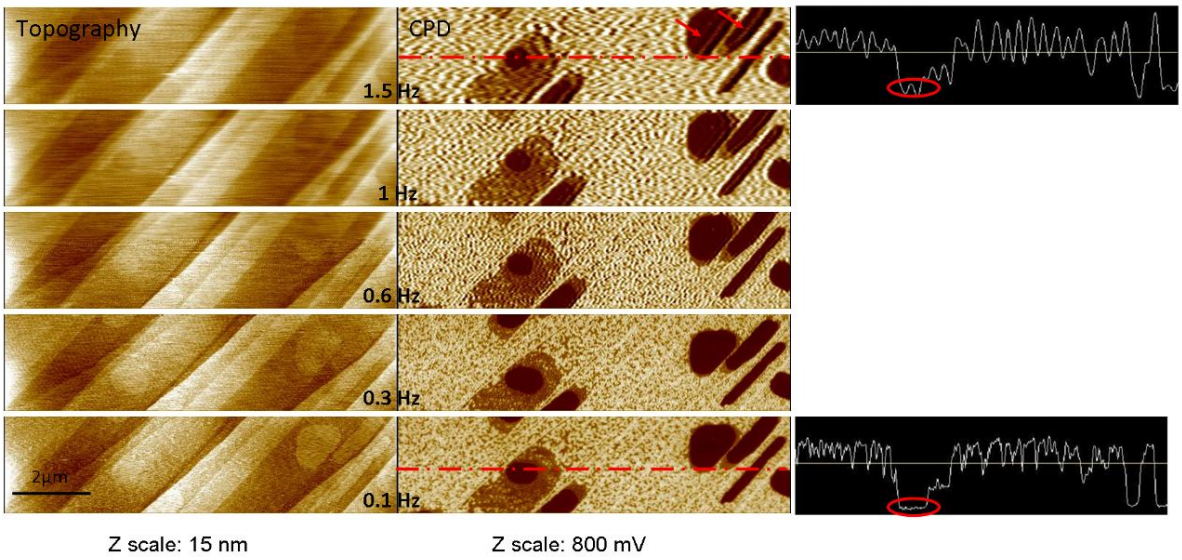

Fig. 3.30 Topography and CPD (in AM-KFM) images on HOPG under secondary vacuum with different scan rates. (*A= 5 nm, V_{ac}= 400 mV and Δf_0= -30 Hz). The* cross-sections on indicated location shows strong artifacts on 1.5 Hz than 0.1 Hz scan (marked in red circle and arrows).

points on each line and scan in both ways), which is just 10 % slower than 0.3 Hz scan. As a conclusion, high scan rate up to 1.5 Hz can be used for fast imaging in order to find good area for analysis. However, fine measurement is only possible by adjusting properly scan rate in function of the number of pixels as well as the time constant of the system.

3.3.4.4 AC drive amplitude comparison

Due to two orders higher quality factor, the ac driving voltage V_{ac} is significant smaller in vacuum than in ambient atmosphere. It also plays an important role in KFM, as it is the balance of tip-induced band bending and sensitivity. However, the main problem of high V_{ac} is not only the tip-induced band bending as in air but also the instability of the non-contact imaging. In Fig. 3.31, different V_{ac} have been tested in AM-KFM. Typically, the tip is crashed when V_{ac} value of 3.2 V is used. The experiment is carried out on HOPG sample with a Pr/It coated Si tip. The features indicated in red box are shown on the right in In Fig. 3.31. With a V_{ac} below 100 mV (labeled ① in the Fig. 3.31), the resulting features appear mainly blur due to an insufficient sensitivity. Between 200 mV and 800 mV (labeled ② in the Fig. 3.31), we observed a good compromise between sensitivity and stability. Above 800 mV (labeled ③ in the Fig. 3.31), the comparably high V_{ac} reduces the topography contrast in comparison to the one obtained with a V_{ac} less than 400 mV. As the topography measurement is not accurate enough, the CPD results suffer. We see the decrease of the sharpness of CPD in group ③.

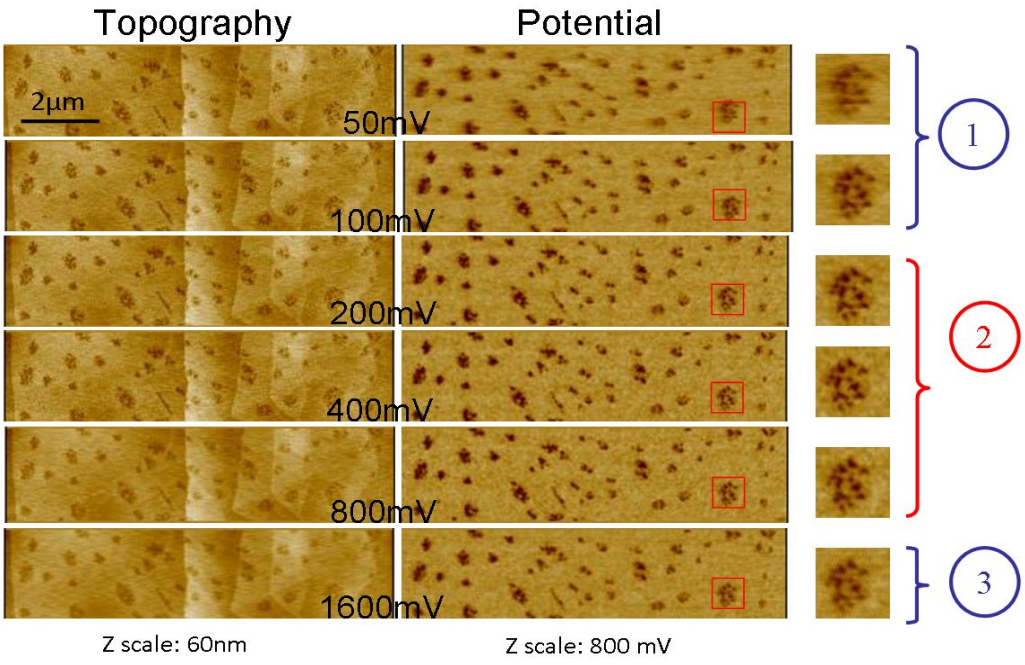

Fig. 3.31 Influence of different V_{ac} drive amplitudes in AM-KFM under secondary vacuum. The zoomed area can be described as 3 groups. Group 1: Low drive amplitude has the bottle neck of photodetector sensitivity. Group 2: Good compromise between sensitivity and stability. Group 3: High drive amplitude leads to the instability of topography loop (i.e. higher electrical amplitude than mechanical amplitude). The tip is crashed on sample during the next drive amplitude setting of 3.2 V.

3.4 Comparison of KFM with other environmental conditions

3.4.1 Comparison of KFM in air and nitrogen

In order to assess the effect of environmental conditions on KFM measurement, KFM in Tapping™ lift mode is performed both in air (with a relative humidity of 21 %) and under N_2 (with a relative humidity close to 0 %). Common KFM settings are applied in these two experiments: oscillation amplitude of 25 nm, lift height of 15 nm and V_{ac}= 6 V.

The experiment is carried out on HOPG sample with a Pr/It coated Si tip. Fig. 3.32 shows that operating under these two environments, similar KFM results have been obtained. KFM sensitivities in air and nitrogen, as extracted from equivalent line profile, are respectively equal to 22.5 mV and 24 mV.

The KFM image under secondary vacuum is given as a reference in Fig. 3.32(c) on the same sample. With the similarity in topography, the KFM contrast has a significantly

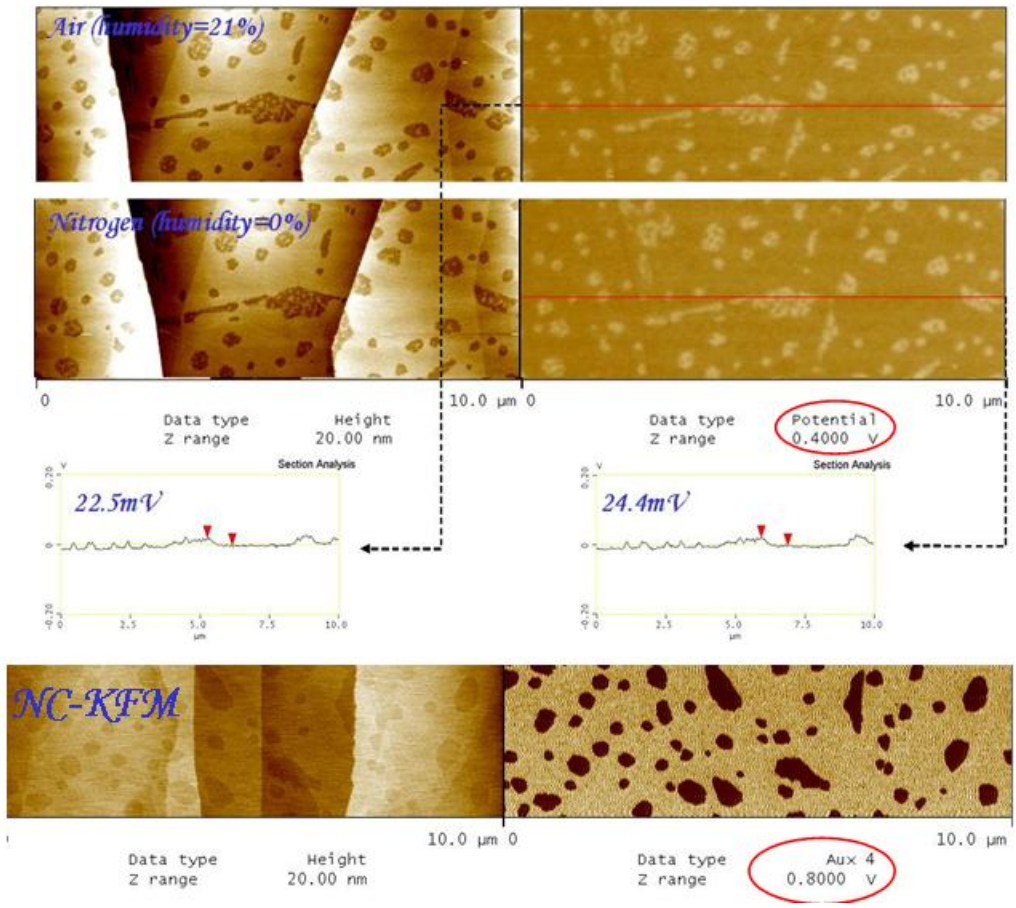

Fig. 3.32 KFM imaging on HOPG sample respectively in air (a), under N_2 (b) and in secondary vacuum (c). Pr/Ir coated silicon tip is used. Experimental parameters: in (a) and (b) A= 25 nm, f_0= 67 kHz, *lift* height of 15 nm, V_{ac}= 6 V. *In* (c) A= 5 nm, f_0= 67 kHz, Δf_0= -50 Hz, V_{ac}= 1 V and f_{el}= 427 kHz.

increase. However, the results can be slightly varied depending on the area analyzed. In order to compare the KFM results obtained on the same location, cross marks on the sample is needed.

3.4.2 Comparison of KFM under secondary vacuum and in air

A cross-mark made by focus ion beam (FIB) on a refreshed HOPG sample has been taken as a reference. As this cross-mark is visible with an optical microscope [see in Fig. 3.33(a)], the relative position is known during each scanning. Several KFM images are scanned nearby and combined into a bigger image [Fig. 3.33(b)] for area identification. Once the same area has been localized, the comparative scan is performed.

In Fig. 3.34, the same area on HOPG sample has been measured by KFM respectively in air and in secondary vacuum. As previously discussed, the sample is contaminated with

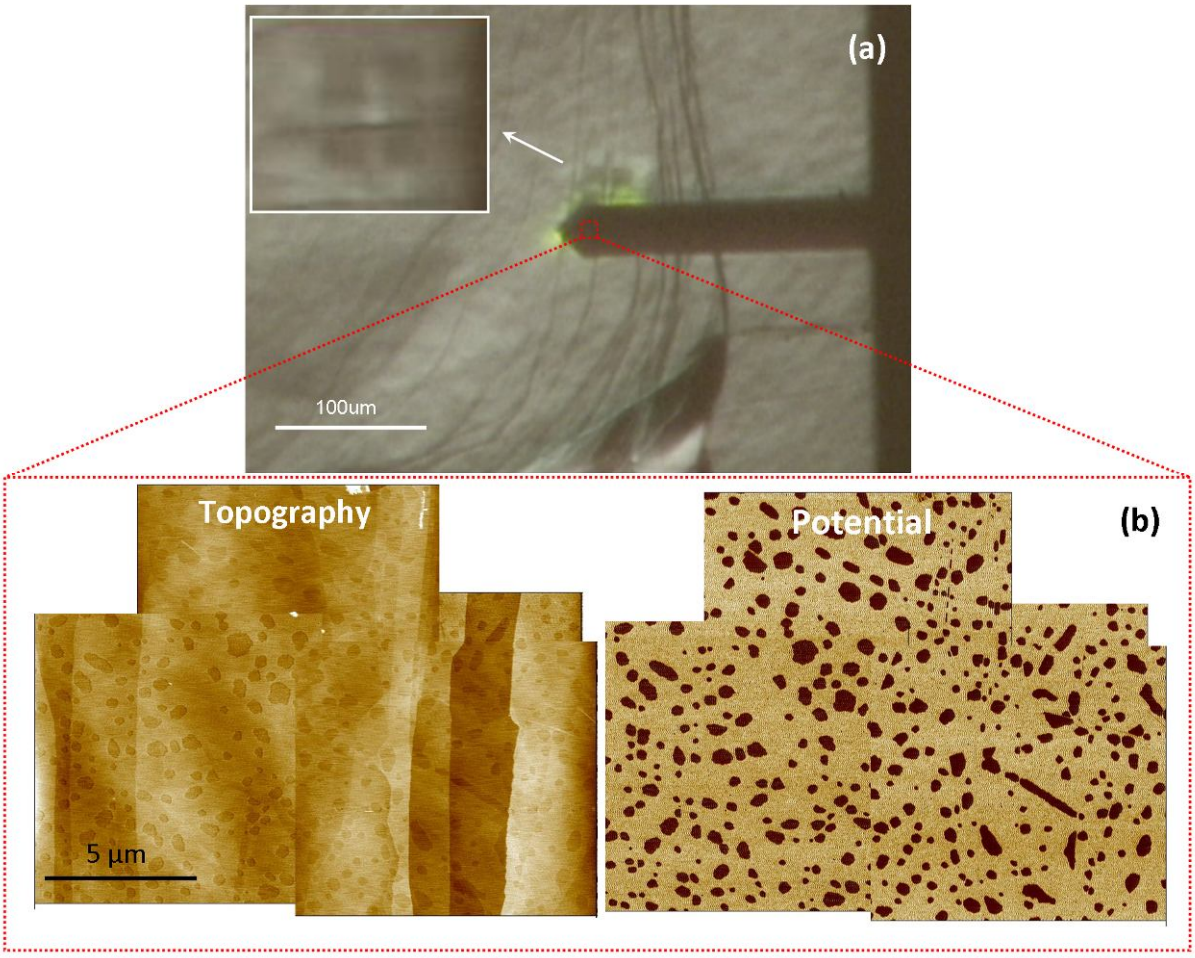

Fig. 3.33 (a) Optical image showing the cross-mark as well as the cantilever position. (b) Several reference scans can be put together to localize the area to compare.

SnO_2 during soldering and allows a high CPD contrast to be observed. In Fig. 3.34(a) and (c), topography mappings are presented in the same scale. The topography image obtained in Tapping™ mode in air brings slightly sharper image than the one obtained in non-contact mode under secondary vacuum. However, no contrast is visible on CPD image obtained by KFM in Lift-mode, while a high contrast of approximately 300 mV is achieved under secondary vacuum.

The same tip is used to do this experiment. The interpretation of the CPD contrast and CPD shift differences can be made in three aspects:

i) The lower tip-sample separation under secondary vacuum reduces the CPD averaging effect and therefore a higher contrast as well as a shift of the CPD average value is expected.

ii) The vacuum environment removes the thin film of the water layer between the tip and the sample surface, which induce a screening effect in air. Thus, no contrast is observed in air.

iii) The high quality factor under secondary vacuum improves the sensitivity of the measurement.

In the chapter 2 (section 2.1.2), the effect of the tip-sample separation is compared in different KFM modes in ambient atmosphere.

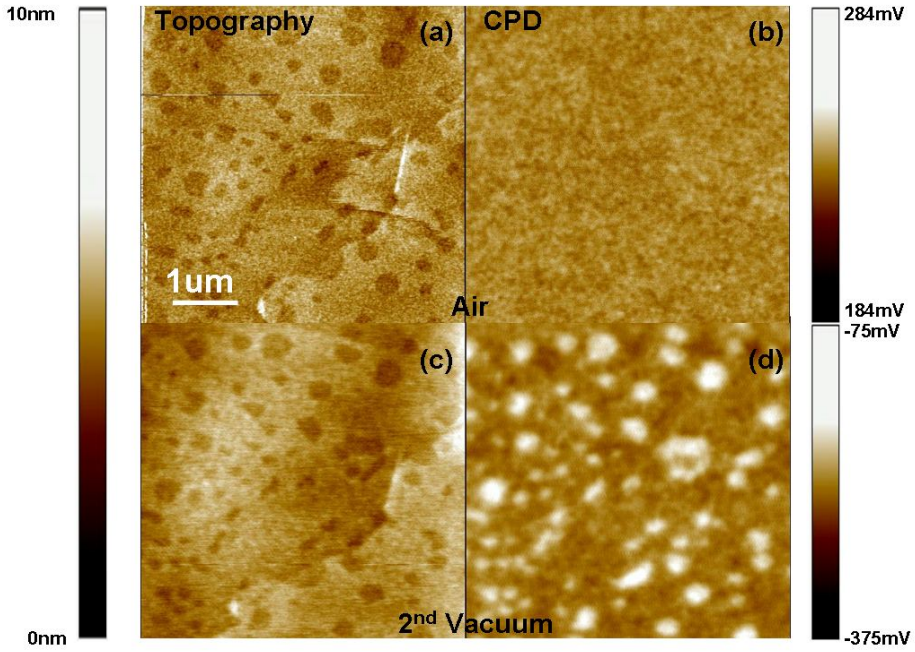

Fig. 3.34 Comparison of KFM measurements in air (Lift-mode KFM) and under secondary vacuum (in AM-KFM) on the same location of a HOPG sample. (a)(c) Topography (Δz=10nm) (b)(d) CPD mapping (ΔCPD=100 mV and 300 mV respectively). Experimental parameters: in (a) and (b) A= 30 nm, f_0= 67 kHz, *lift* height of 8 nm, V_{ac}= 8 V. *In* (c) and (d) A= 5 nm, f_0= 67 kHz, Δf_0= -7 Hz, V_{ac}= 400 mV and f_{el}= 427 kHz.

3.5 Summary

The KFM technique is mainly used in air allowing a quick start and ease of use for multiple comparative analyses with semi-qualitative results. However, more accurate and reliable measurements can be achieved by working under vacuum. In summary, we described in this chapter the implementation of work function measurement by Kelvin probe force microscopy (KFM) under secondary vacuum. The instrumentation work is carried out with an EnviroScope™ AFM from Bruker. An external electronic from Nanonis was installed to perform AFM imaging in non-contact and relating surface potential measurements. Consequently, challenges of compatibility, calibration and optimization have been overcome to reach this goal. Our results show that UHV comparable results can be obtained under secondary vacuum.

Chapter 4

Investigation of charge transport in CdTe/CdS heterojunction using Kelvin force microscopy

In this chapter, the Kelvin force microscopy (KFM) and the scanning Auger microscopy (SAM) are combined to characterize the electrical and chemical properties of the CdTe/CdS heterojunction, which seems to be a good candidate for solar cell applications. These two techniques are evaluated in order to achieve a better understanding of the mechanisms involved in the charge transport inside of the solar cell. A protocol for the cross section sample preparation has been specifically developed. Mechanical polishing after cleavage is used to decrease the roughness of the surface. The CdTe/CdS heterojunction is studied under polarization both in dark and under illumination. The depleted region near the CdTe/CdS heterojunction is well observed by the KFM technique and is clearly widened under reverse bias polarization. Under illumination, a change of the surface potential distribution is observable mainly induced by the creation of electrons and holes at the CdTe/CdS interface. The influence of the CdS layer thickness is also studied because of its dramatic effect on the solar cell efficiency. The efficiency difference can be explained firstly by the presence of an unexpected electric field near the CdS/ITO interface as evidenced by KFM and secondly by a lower transparency of the CdS layer due to the chemical modification induced by the tellurium diffusion occurring at the CdTe/CdS interface.

4.1 Motivation

CdTe/CdS based photovoltaic modules have become the lowest-cost producer of solar electricity, despite working at lower efficiency (≤16.5 %) than crystalline silicon cells (≤ 21 %). [105] There are two main reasons. Firstly, CdTe has a direct band gap of 1.5 eV, which is optimal for the conversion of the solar radiation. [106,107] Secondly,

polycrystalline CdTe cells outperform their single crystalline counterparts, [108] resulting in lower material-quality requirements and manufacturing costs. Currently, the record efficiency of 16.5 % is still much below the theoretical maximum of 29 %. [109] This means that more knowledge of the device operation is required to further improve the performance.

Among the techniques, capable of measuring the electrical properties at nanometric scale with a good sensitivity, the Kelvin force microscopy (KFM) [37,38,39] has shown its potential to become a routine characterization tool for different kinds of photovoltaic modules. [94,95,97] In this way, spatially resolved analysis can be done to study the local variation of the contact potential difference (CPD) induced by any surface dipole or surface charge distribution or by a bulk chemical potential modification.

In this chapter, capabilities of the KFM technique are evaluated for the electrical characterization of the CdTe/CdS heterojunction. Complementary analysis such as SAM technique, SIMS or C-AFM are also used to get a better understanding of the mechanisms involved in the charge transport inside of the solar cell.

4.2Experiments

4.2.1 CdTe/CdS heterojunction for solar cell application

4.2.1.1 Sample description

The typical structure of the cell is shown in Fig. 4.1. The thin-film solar cell consists of a substrate, a transparent conductive oxide (TCO) layer, the active region composed of a window layer and an absorber layer and finally a metal contact. Each of the component material has different physical and chemical properties and each affects the overall performance of the device in some way or another. A critical understanding of the behavior of these individual components is essential for designing a device. The function of these different layers is described as follows:

Glass substrate

CdTe based devices are fabricated preferably in superstrate configuration where the glass substrate is not only used as a supporting structure but also as a transparent window for the illumination and as a part of the encapsulation (see Fig. 4.1). Two kinds of glass substrate are used: the borosilicate or the soda-lime glass. Its thickness is larger than the one of the other layers, which is required to strengthen the device. It should be noted that the substrate absorb in the infrared ($\lambda > 2$ µm) because of an increase of the temperature within the substrate. This is very important because otherwise, the infrared light would be absorbed in the active region of the cell, which could result in a degradation of the cell

performance. The borosillicate has fewer impurities than the soda lime, and so low optical absorption, but it is more expensive. As a consequence, the soda-lime glass is often used in laboratory.

Transparent conductive oxide (TCO)

The transparent conductive oxide layer acts as an electrode which must have a good transparency in the visible spectral range together with a high electrical conductivity. In general, *n* type degenerate semiconductors, such as SnO_2 or In_2O_3, are used: Sn (ITO) [110], where the resistivity is respectively 2×10^{-4} Ω·cm and $3.5\text{-}5 \times 10^{-4}$ Ω·cm [111] and the transparency is 95 % and 90 %, respectively. [112,113]

Window layer (CdS)

Polycrystalline n-type CdS material is chosen as the window layer to form the heterojunction with the CdTe absorber layer. As the CdS bandgap is 2.44 eV, a typical thickness of 60 nm is sufficient to limit as little as possible the photon absorption in the ultraviolet to blue light spectral range. In theory, no photocurrent is generated in this layer. [114] The lattice mismatch at the CdS/CdTe heterojunction is about 9.7 %, which is relatively high in comparison with, for example, the almost perfect lattice match between CIGS (112) and CdS(001). However, the Te diffusion occurring during the CdTe growth forms a $CdS_{1-x}Te_x$ interfacial layer, which reduces the lattice mismatch near the interface. It is worth noticing that the CdS material exhibits an intrinsic n-type doping induced by sulfur vacancies.

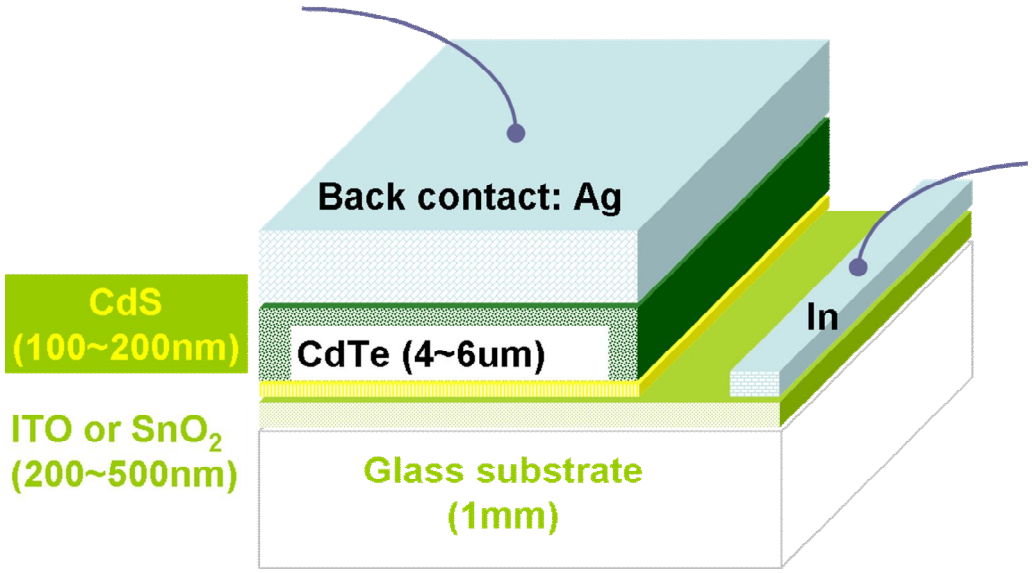

Fig. 4.1 Simplified schematic of the solar cell structure: glass substrate (1 mm)/ ITO (200 nm used in sample 1) or SnO_2 (500 nm used in sample 2)/ CdS as a the window layer (between 100 and 200 nm)/ CdTe as the absorber layer (between 4 and 6 µm)/ a Te-rich p+ layer/ Silver back contact. Indium is soldered on transparent conductive oxide (TCO) as another contact.

Absorber layer (CdTe)

CdTe is an ideal p-type absorber material with a direct bandgap of 1.44 eV and an absorption coefficient around 10^{-5} cm^{-1} in the visible region. [115] This indicates that the 90 % of incident photons can be absorbed in a few micrometers thickness (typically 2 µm is sufficient). A typical thickness in the range between 4 and 6 µm is classically deposited in order to achieve micron grain in size, which results in higher performance. CdTe has intrinsic native defects such as Cd vacancies (dominant acceptor) or Te anti-site which results in intrinsic p-doped material.

In this chapter, two different samples have been characterized:

- Sample 1: a 1 mm thick borosilicate glass is taken as a substrate covered with a 200 nm indium-tin oxide (ITO) layer deposited by sputtering as the window layer. The CdS layer is grown by chemical-bath deposition (CBD) with an expected thickness of 100 nm. [116,117,118] Closed-space sublimation (CSS) [119,120,121] is used to produce polycrystalline CdTe in a expected thickness range of 4 µm to 6 µm. [122] As discussed elsewhere [123,124,125], a $CdCl_2$ treatment at high temperature (380 °C) for 30 minutes seems improve the cell performance. In order to form an ohmic contact, Cu-doped graphite paste is firstly deposited and annealed to create a Te-rich p^+ layer. [118,126] Finally, this paste is removed to achieve the back contact with silver paste.
- Sample 2: similar to the sample 1 excepted that ITO layer is replaced by a 500 nm thick SnO_2 layer deposited by spray pirolysis on a 3 mm thick soda-lime glass substrate. Moreover, a 200 nm thick CdS layer was deposited by CBD.

4.2.1.2 Protocol of sample preparation

Preliminary KFM measurements have been done on the CdTe surface in order to check the topography and the illumination influence on the CPD. In Fig. 4.2.a, the rough surface and the related CPD mapping are presented in dark condition[8]. As already shown in previous chapter, the CPD contrast exhibits a strong correlation with the topography features. In Fig. 4.2.b, the visible light provided by the optical microscope as well as the room illumination light are switched on to test the influence on the CPD contrast. No obvious change on the CPD mapping is observed (871 mV comparing with 873 mV in dark), as shown on histograms.

As a consequence, the following drawbacks may impinge the CdTe surface analysis by KFM. As the CdTe has a thickness in the range of 4 to 6 µm, the KFM technique cannot

[8] Both light illumination from the room and the optical microscope are switched off.

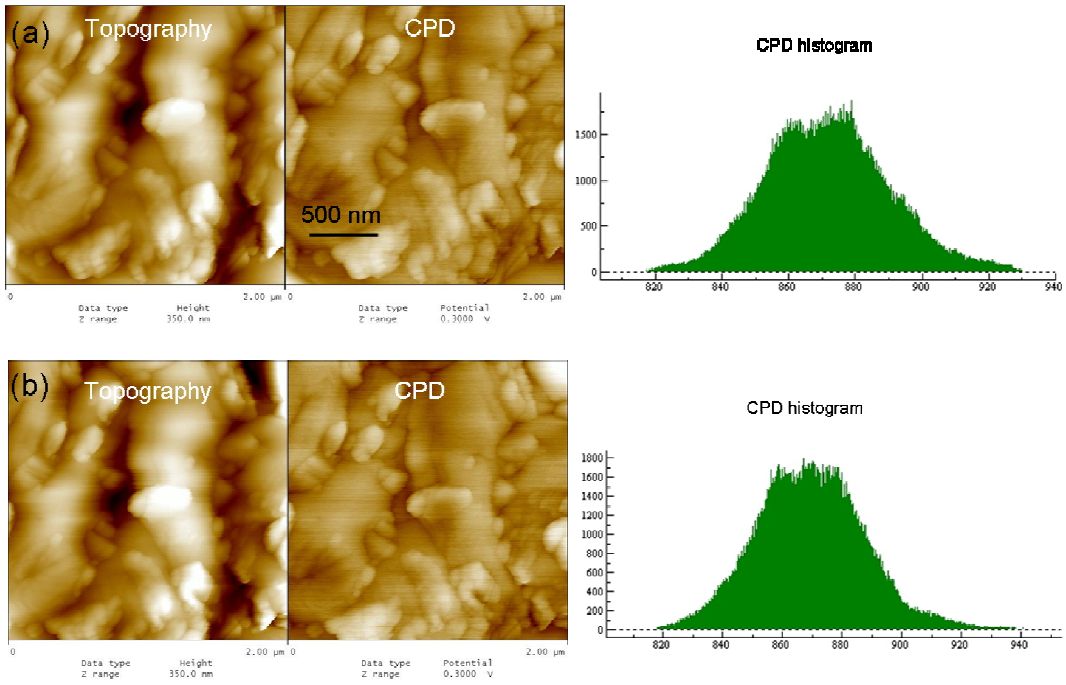

Fig. 4.2 Topography and CPD mappings of the CdTe surface of sample 1 performed in dark (a) and under illumination (b). The KFM measurement is done in Lift-mode (lift height = 15 nm) and both contacts are grounded. No obvious change on the CPD mapping is observed (871 mV comparing with 873 mV in dark).

probe the CdTe/CdS p-n heterojunction, which is more interesting to understand the mechanism of the charge transport involved in the device. Moreover, the illumination of the CdS/CdTe heterojunction is not optimized, mainly because it is difficult to reach the CdS layer through the glass subtrate-ITO as shown in Fig. 4.1.

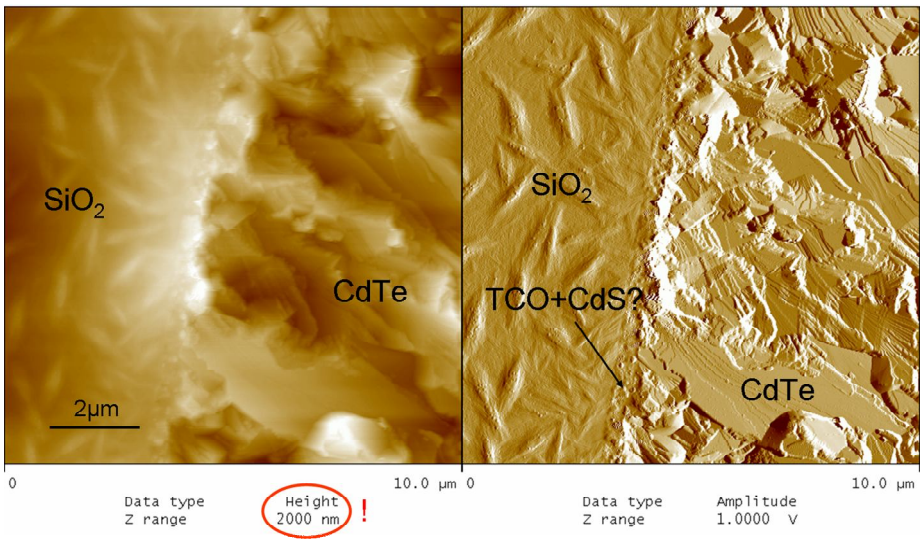

Fig. 4.3 Topography image on the cross section after the cleavage of the sample 1. A huge variation of the topography is visible (peak-to-peak of 2 µm).

Therefore, a cleavage of the structure is done to make possible the KFM analysis on the cross-section. The corresponding topography after the cleavage is shown in Fig. 4.3. Two obvious different areas are well distinguishable on the z-feedback error image (amplitude image) corresponding to the glass substrate (on the left part) and the CdTe layer (on the right part). At the interface of these two parts, both ITO and CdS layers can barely be distinguished. In fact, the peak-to-peak topography of about 2 µm indicates a very rough surface, where precise KFM measurements are impossible. To overcome this problem, a sample preparation protocol has been developed.

In this protocol, the glass/TCO/CdS/CdTe structure is cleaved along a scratch line done on the substrate backside. Fig. 4.4(d) clearly reveals a polycrystalline structure of the CdTe layer which cannot, due to the roughness, be analyzed directly by KFM. To decrease the roughness, the sample 1 and 2 have been polished by using a Centar Frontier equipment from Gatan[9] (Pleasanton, USA). Both samples are firstly polished with 6 µm diamond lapping film to remove the sharp fringes caused by the cleavage. As a result, a rms roughness less than 20 nm (see Fig. 4.4.a) is obtained. Samples are then successively polished with 1 µm diamond film and 0.25 µm SiO_2 lapping film, to decrease the rms roughness down to 3 nm (see Fig. 4.4.b). After these steps the rms roughness is low enough to do KFM but in order to make the interface visible, we keep on polishing the cross section with non-crystalline 0.02 µm colloidal silica by VibroMet 2 Vibratory Polisher from Buehler[10] (Lake bluff, USA). Finally the sample is cleaned up by wiping the cross section with a soft fine tissue. However, this step degrades the rms roughness up to 10 nm (images not shown here). The main reason is that the amorphous silver back

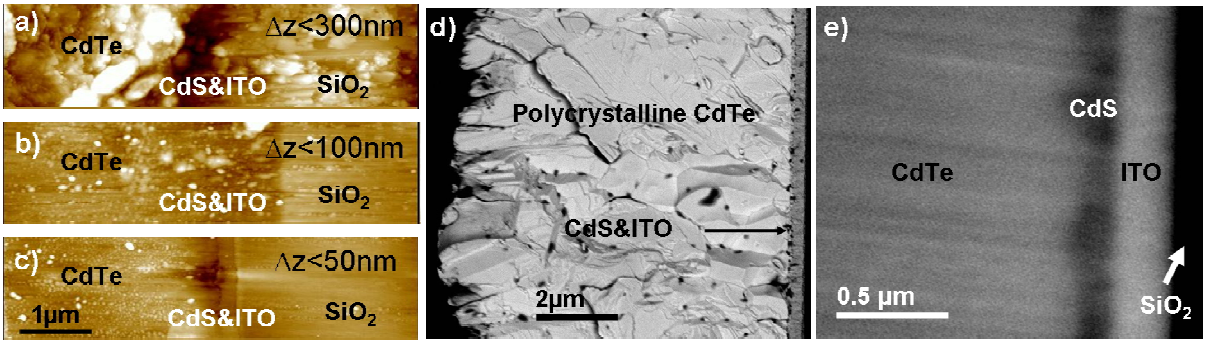

Fig. 4.4 (a-c) Topography images of polished cross-section of sample 1. The lapping film grain is successively 6 µm diamond, 0.25 µm SiO_2 and 0.05 µm alumina. (d-e) SEM images on cross-section before and after polishing.

[9] Details are given on this website: http://www.gatan.com/specimenprep/images/FrontierDsheetFinal.pdf

[10] Details are given on this website: http://www.buehler.com/productinfo/Petro/pdf/VIBROMET.pdf

contact generates various particles on the surface after soft tissue polishing. The best results were achieved by gently polishing the surface with 0.1 µm diamond and then 0.05 µm alumina lapping film. After this procedure, the surface rms roughness decreased down to 1 nm and as shown in Fig. 4.4(c) and (e) the 200 nm layer of ITO can be clearly distinguished.

Although the polishing protocol provides a low roughness surface suitable for KFM measurement, it always pollutes the sample surface with small particles coming from the lapping pad. These particles cannot be easily removed as they are physically studded into the different layers. Nevertheless, as we will show later, these particles have no significant influence on the results.

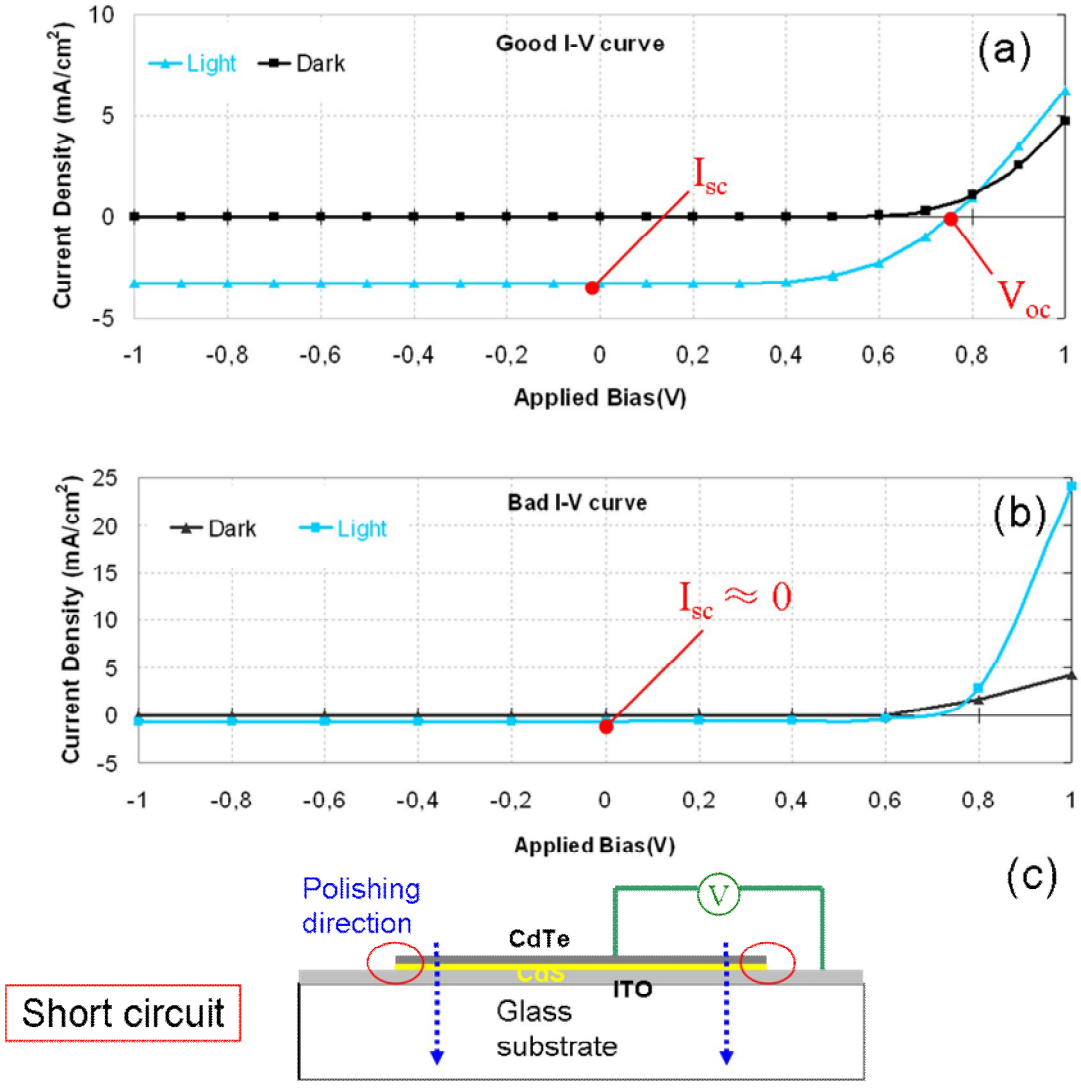

Fig. 4.5 Typical I-V characterizations after polishing steps. (a) Normal I-V curve. (b) I-V curve showing a short circuit. (c) Schematic of the sample structure shows where the short circuit appears.

In order to check if the sample preparation degrades the cell performance, I-V curves [see Fig. 4.5(a)] have been done, after polishing, both with and without illumination. Sometimes, under illumination, the current I_{sc} is equal to zero [Fig. 4.5(b)]. This is due to a short circuit created, during the polishing, between the TCO layer (ITO or SnO_2) and the CdTe layer [the red circle in Fig. 4.5(c) shows the location of a possible short-circuit]. In practice, the cell can be repaired by scratching off the CdTe and the CdS layers near the edge.
To sum up, Fig. 4.6 describes the preparation protocol of CdTe/CdS samples.

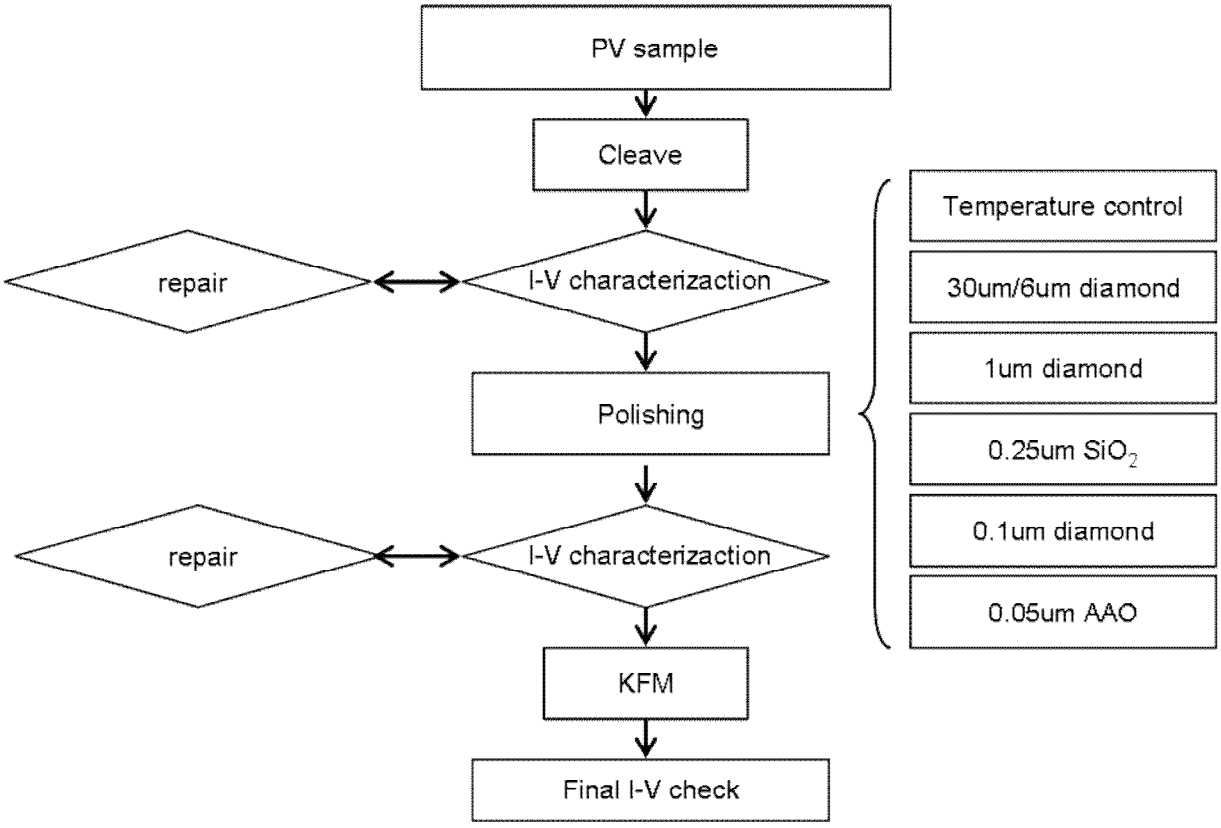

Fig. 4.6 Protocol of CdTe/CdS cross-section preparation.

4.2.2 Electrical properties of CdTe/CdS heterojunction

4.2.2.1 Experimental setup

The KFM experimental setup for cross-section analysis is presented on Fig. 4.7. The ITO layer is grounded via an indium contact while silver paint is used to connect the grounding wire of the CdTe layer. The experiments under polarization are performed by using a digital multimeter from Keithley Instruments (Solon, USA), located between the silver

paint contact and the ground. The experiments under illumination are performed with a 2 W white LED source from CJ-Light GmbH located at 5 cm away from the glass side.

KFM measurements are carried out both with Dimension 3100 and MultiMode Microscopes from Bruker (Santa Barbara, USA) equipped with Nanoscope IIIa and Quadrex for KFM measurements in Lift-mode. Pt/Ir coated silicon tips from Budget Sensors with a force constant of about 3 $N \cdot m^{-1}$ are used. Some experiments have been performed with the Nanonis dual-OC4 electronic (SPECS, Berlin, Germany) in order to realize the simultaneous topography and KFM imaging in a single-scan mode. In this case, KFM experiments have been performed in the amplitude modulation (AM) mode.

4.2.2.2 Contact Potentiel Difference (CPD) distribution in dark

The typical topography image obtained on the cross-section of the sample 1 can be seen in Fig. 4.8(a). It shows a flat surface after the polishing procedure. Due to the similar stiffness of CdS and CdTe materials, the 100 nm CdS layer can barely be seen, whereas the ITO layer can be distinguished. Fig. 4.8(b) shows the typical CPD distribution obtained in dark conditions. Starting from the right of the image, there is a slight CPD variation along the CdTe layer due to the polycrystalline structure, until we reach the CdTe/CdS interface where a large drop of potential is observed corresponding to the pn heterojunction. In this case, both contacts of the sample (i.e. Ag and In contacts) are grounded in order to avoid a transport of charges along the surface. However, as can be seen on the left of the image, a high CPD is observed on the glass substrate probably induced by an accumulation of trapped charges.

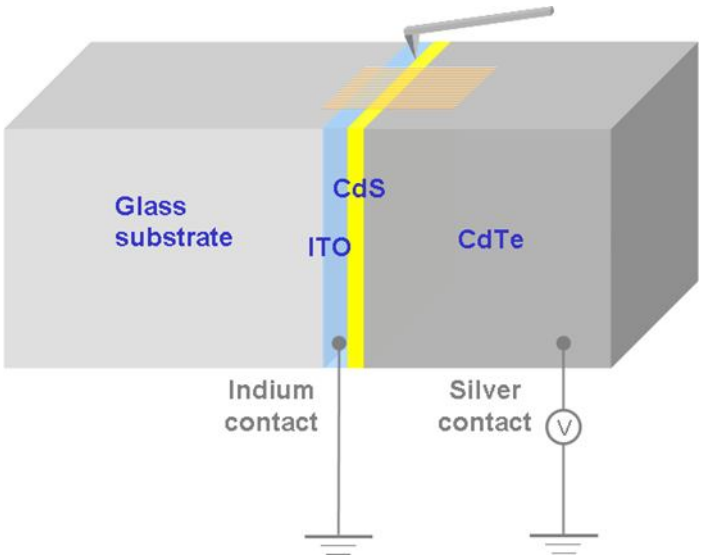

Fig. 4.7 Experimental setup of the KFM measurement done on the cross-section of the cell structure. Here sample 1 is taken as an example.

Fig. 4.8(c) shows the line profile of both topography and CPD mapping on the indicated position in Fig. 4.8(b). The apparent positions of interfaces are deduced from the topography image [see Fig. 4.8(a)]. An accurate location of CdS layer is hard to distinguish due to the similar mechanical properties of CdTe, therefore the verification of layer thickness is necessary, which will be discussed in the section 4.2.4. In our expectation, CdS material has a lower work function (4.7 eV in reference [127]) than the CdTe material (between 5.5 and 5.9 eV found in references [128,129,130]). According to Eq. (1.24), the CPD on CdS part should be higher than on CdTe part, but this conclusion is not in agreement with our experiment results. As explained elsewhere, Fermi level pinning effect can be induced by the polishing process resulting in a modification of the CPD near the surface and leading to measured values different than the bulk values. [131] In order to overcome this effect, a reverse bias can be applied to the solar cell and will be discussed in section 4.2.2.5.

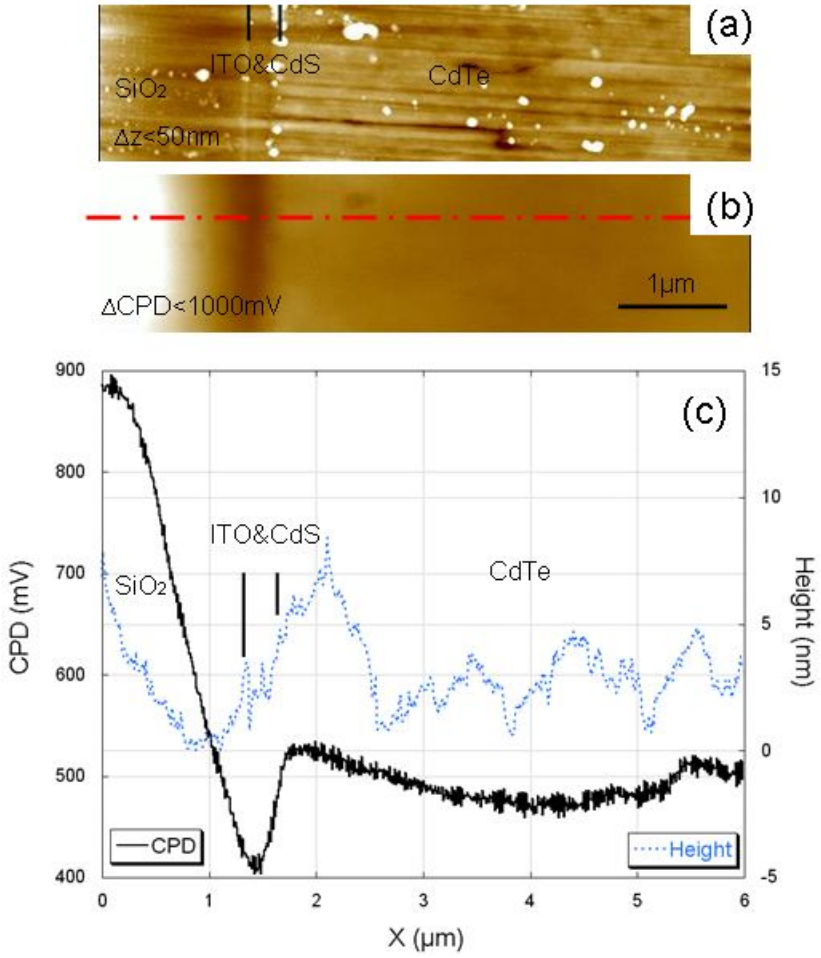

Fig. 4.8 KFM measurement on cross-section. (a) Topography (with a 1st order flatten). (b) CPD distribution and (c) line profile where the apparent positions of layer interfaces are deduced from the topography image.

4.2.2.3 Estimation of the CdS layer thickness

As the different thin layer has different resistivity, scanning spreading resistance microscopy (SSRM) has been employed to estimate the CdS layer thickness. In SSRM, a hard conductive tip (diamond tips are currently used) is scanned on the surface in contact mode while a dc bias is applied to the sample. The schematic of SSRM setup is presented in Fig. 4.9(a). The current flowing between the tip and the sample is measured with a logarithmic current-voltage amplifier (SSRM module from Bruker) allowing a current measurement in the range of 10 pA to 0.1 mA. This module converts the current into resistance, corresponding to a typical range of 10^4 Ω to 10^{11} Ω with 1 V dc bias. The measured total resistance R is a sum of resistance in series including the tip resistance R_{tip}, the tip to semiconductor contact resistance $R_{contact}$ that defines the nature of the contact (ohmic or Schottky), the spreading resistance R_{spread}, the sample series resistance R_{series} and the back contact resistance R_{back} :

$$R = R_{tip} + R_{contact} + R_{spread} + R_{\text{series}} + R_{\text{back}} . \quad \textbf{(4.1)}$$

If the force applied onto the sample surface is high enough, Eq. (4.1) is dominated by the spreading resistance, which in a simplified model is related to the local resistivity ρ of the semiconductor according to:

$$R_{spread} = \frac{\rho}{4R_e}, \quad \textbf{(4.2)}$$

where R_e is the "electrical contact radius". The radius R_e is generally smaller than the tip radius. One possible explanation is that the large pressure (>12 GPa) used in SSRM results in the following phase transformation: Si-I (diamond structure) → Si-II (β-Sn). The highly conductive Si-II phase forms a small pocket underneath the probe responsible for a good electrical contact with an apparent radius smaller than the tip radius. [132] The SSRM imaging on the cross section of sample 1 is shown in Fig. 4.9(b) and a line profile in is presented in Fig. 4.9(c). Owing to their change in resistance, different layers can be discriminated. Due to the large range of the measured resistances a logarithmic scale is used. The very high insulating part (red color) and the high conductive part (blue) are supposed to be respectively the glass substrate and the ITO layer (200 nm in thickness). Between the ITO layer and the CdTe layer (yellow color), a high resistance layer is observed, which is supposed to be the CdS layer. The CdS layer presents a non-uniform

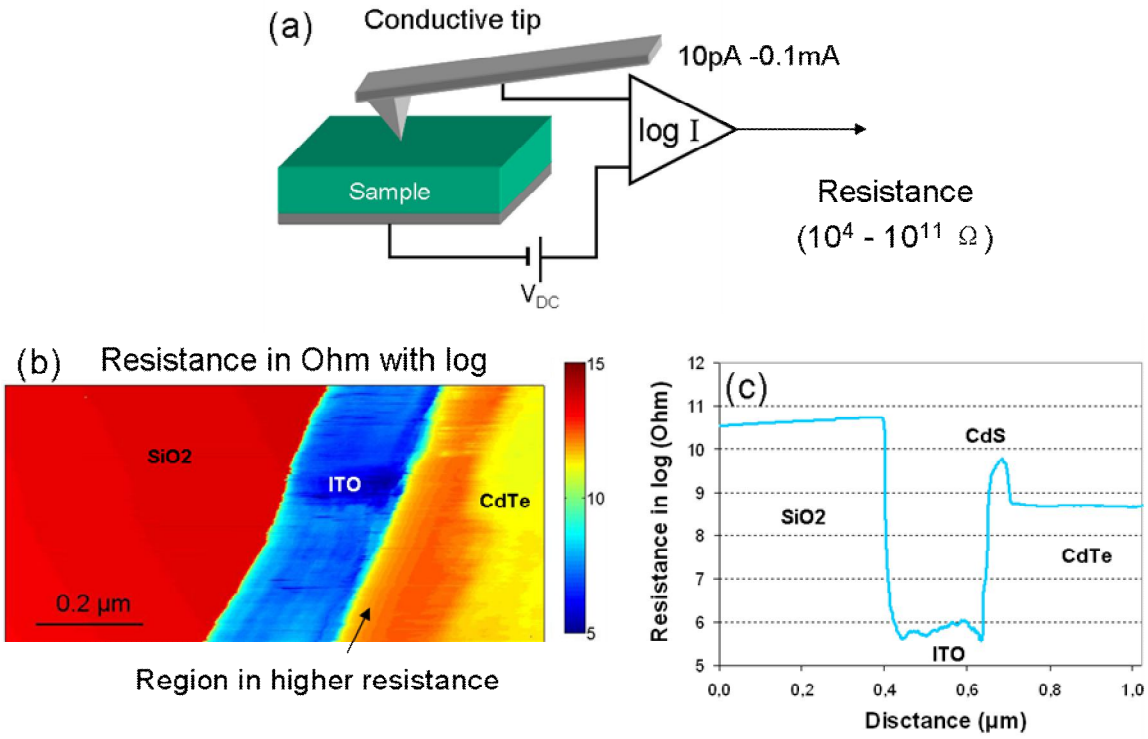

Fig. 4.9 (a) Principle of scanning spreading resistance microscopy (SSRM). (b) Resistance mapping obtained by SSRM on the cross section of the sample 1. (c) Line profile extracted from the resistance mapping.

thickness which ranges between 100 nm and 150 nm, this non-uniformity is probably induced by Te diffusion, a mechanism that will be discussed later. It is worth noting that the non-uniformity of the CdS thickness is also visible on the SEM image presented in Fig. 4.4(e).

4.2.2.4 CPD evolution under illumination

A comparison of CPD measurement by KFM in dark and under illumination is presented in Fig. 4.10. The sample illumination with a 2 W white LED source located 5 cm away from the glass substrate is sufficient to observe a variation of the CPD. In order to quantify this variation, CPD measurements have been done in the same area both with and without illumination. Typical line profiles (indicated as the red line) are extracted from the CPD mapping. Due to the mechanical drift between the two series of images, maybe induced by the illumination, the line profile done on topography images is used to match the features to make sure that the corresponding CPD line profiles are exactly at the same position. As we can see on bottom left of the Fig. 4.10, the resulting topography line

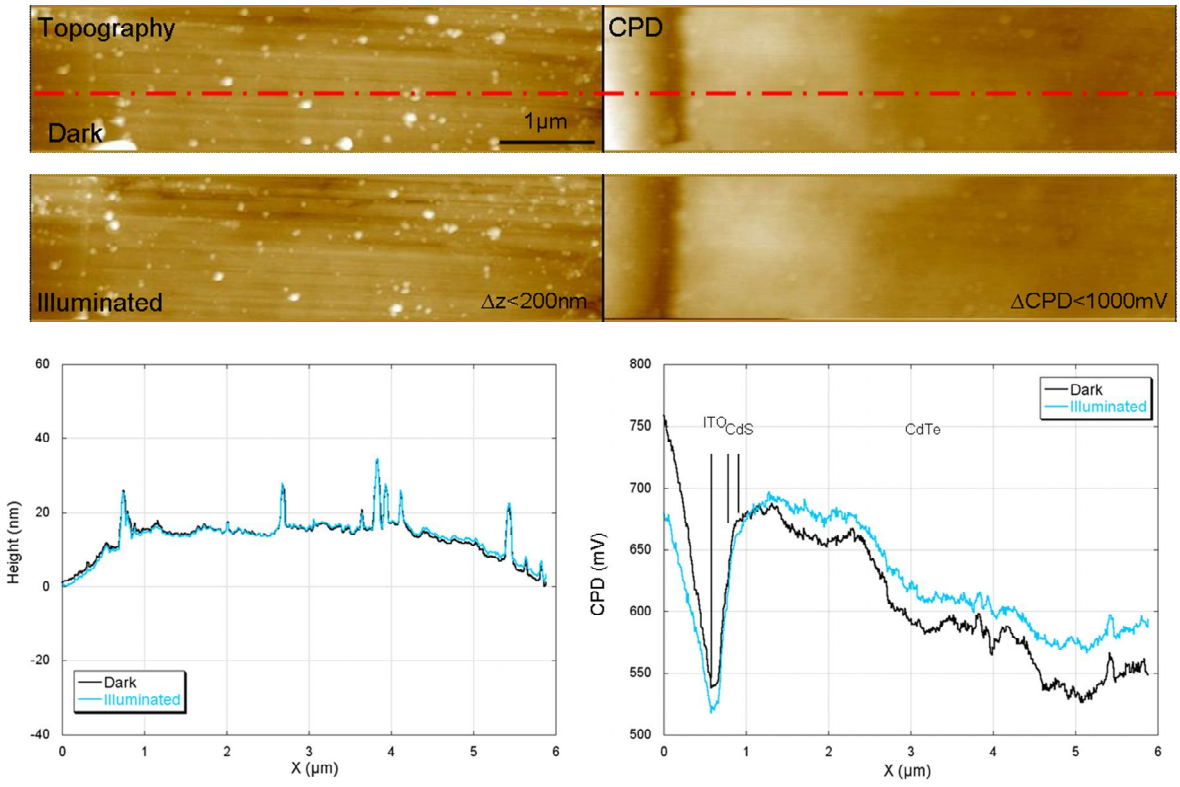

Fig. 4.10 KFM measurement performed on the cross section of sample 1 in dark and under illumination.

profiles match very well. Their corresponding CPD line profiles are shown on the bottom right. A slight increase of the CPD under illumination is visible in the CdTe layer while a very small decrease is barely seen in the CdS layer mainly due to because the holes are generated at the CdTe side while electrons at the CdS side.

4.2.2.5 Electric field evolution under polarization

Experiment under polarization has been done on the same area of the sample 1. Fig. 4.11 shows typical CPD line profiles obtained with a bias ranging between -5 V to 5 V. To compensate the CPD profiles-shifting, these superimposed by matching their associated topography line profiles. These topography line profiles (not shown here) remain the same regardless the applied biases, this confirms that even strong biases do not impact the topography mapping.

A large change of CPD arises in the neighborhood of the CdTe/CdS interface. As expected, when a forward bias is applied, the CPD in the CdTe layer is constant. The region adjacent to the CdS/CdTe interface and inside the CdTe layer is the depletion region. As expected, the width of the depletion region increases when the reverse bias

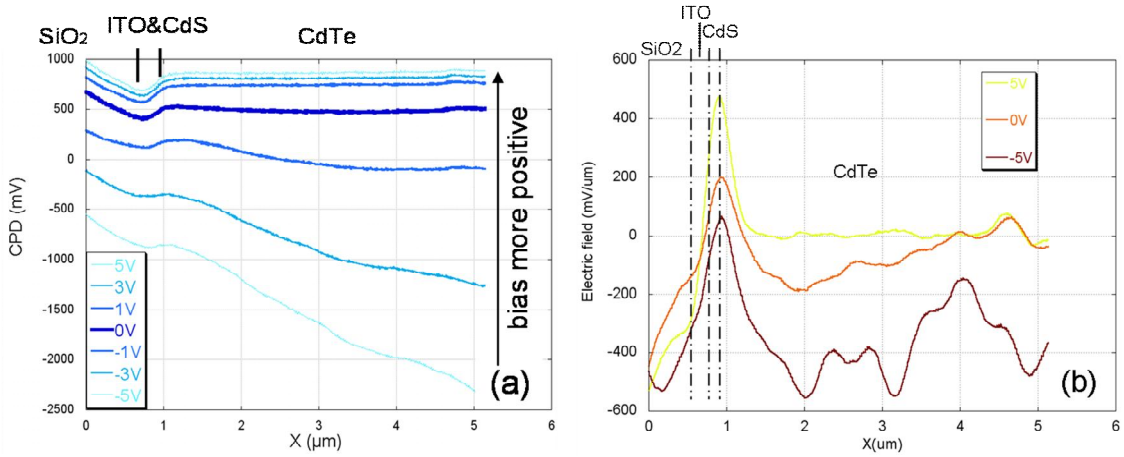

Fig. 4.11 (a) KFM scanning results with different bias along (b) The electric field distribution (derivative of KFM data) under -5V, 0V and 5V biases.

increases. As can be seen in the Fig. 4.11(a) the space charge region extends to a width of about 4 µm and no region with a small potential drop, which could correspond to a neutral region inside the CdTe, is observed. Notice that the depletion region does not extend much into the CdTe if no reverse bias is applied. These results are similar with results obtained by Mouthino *et al.* on the same structure. [131] The authors of this paper show that the CPD variation is not in agreement with the theoretical band diagram of the structure. Fermi level pinning at the surface of the material induced probably by the polishing protocol is certainly the main reason that could explain this disagreement. Thus, the sample preparation can strongly affect the CPD measurement. .

To obtain further information on the properties of the CdTe/CdS interface and depletion layer, the electric field distribution inside of the structure is evaluated by taking the first derivative of the CPD potential curve shown in Fig. 4.11(a). Fig. 4.11(b) shows the result respectively at -5 V, 0 V and 5 V biases. As expected, the electric field is maximal near the CdTe/CdS junction. Moreover, some variations are also observable inside of the CdTe a maximal electric field layer which is probably induced by the polycrystalline structure of the CdTe. The maximum of the electric field indicates the position of the pn CdS/CdTe heterojunction.

4.2.3 **Chemical composition analysis**

In order to assess both the thicknesses and the chemical composition of the different layers, time-of-flight secondary ion mass spectrometry (ToF-SIMS)[11] has been performed

[11] Ion Tof GmbH, Münster, Germany

on sample 1.The sample is alternatively sputtered by an O_2^+ beam (2 keV, 400 nA and raster size of 250 µm × 250 µm) and analyzed using a Bi^+ ion beam (25 keV pulsed at 1 ns over a 80 µm × 80 µm area). The working pressure is 2.6×10^{-8} mbar. The results can be seen in Fig. 4.12. The profile shows that the Cd and Te chemical elements are stable in the CdTe layer. In the same way, the S and Cd elements presents the same behaviour in the CdS layer. However, a large amount of Te is detected in the CdS layer, which means that a CdS_xTe_{1-x} alloy is present. The Sn element start to reach its peak as the beam reaches ITO layer. Finally, Si^+ is obviously detected in SiO_2 substrate.

It is worth noting that it is difficult to accurately position interfaces between different layers. The apparent diffusion of Sn into SiO_2 is likely to be sputter depth profiling artifact. The reason for this is that the comparatively large analysis area (80 µm x 80 µm) and the non homogeneous layer can lead to a non-synchronized layer exposure time. Moreover, the estimated depth of each layers are calculated by the average etching rate of CdTe/CdS/ITO layers. Due to the difference of the real etching time in such layers, the depth measurement can not be considered as the real layer thickness.

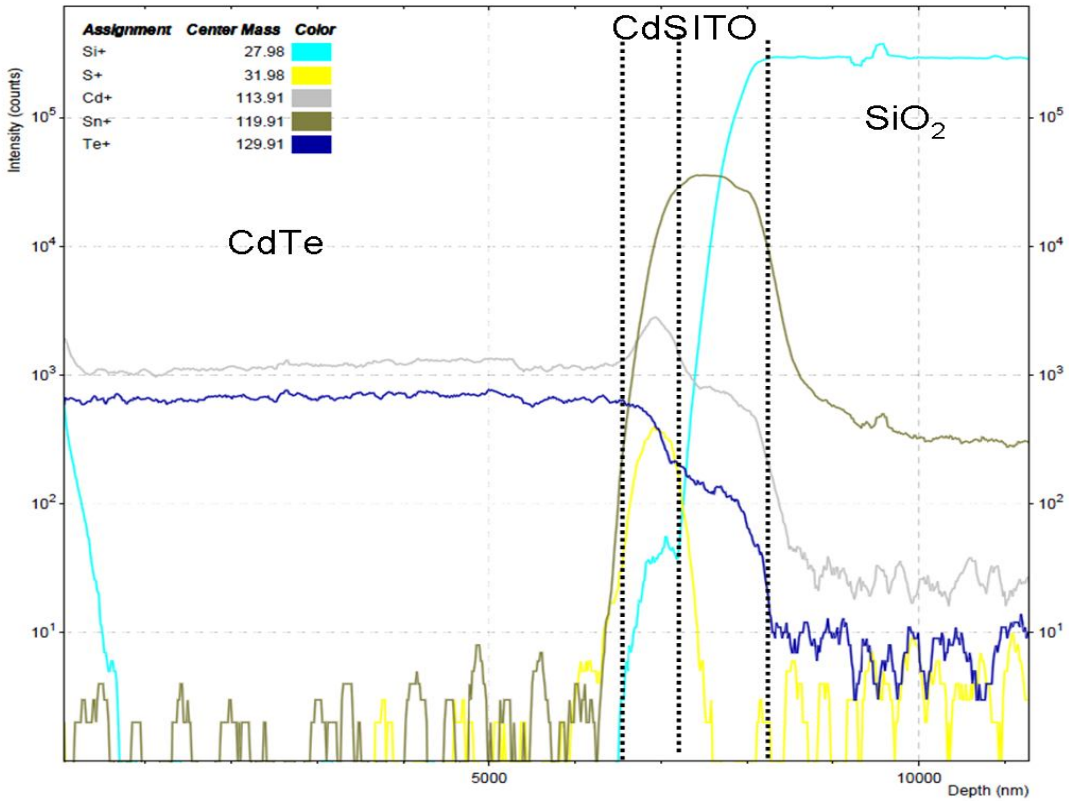

Fig. 4.12 ToF-SIMS depth profile on sample 1 defined as CdTe (6 µm)/CdS (100 nm)/ITO (200 nm)/SiO_2 (1 mm). The depth is estimated by the average O^{2+} sputtering rate on CdTe/CdS/ITO layer.

This measurement indicates the existence of an interfacial CdS_xTe_{1-x} layer. Therefore, Auger electron spectroscopy is employed to confirm this result. The Fig. 4.13(a) shows the schematic of the PHI 700Xi scanning Auger nanoprobe system from Physical Electronics (PHI, Lake Drive East, USA) used for this analysis. An Ar^+ ion gun set as 20° with respect to the sample surface can be used to sputter the sample. The electron gun is vertically installed to reduce shadowing effects. Auger electrons are collected with a cylindrical mirror analyzer, coaxial to the electron gun. The SEM image presented on the Fig. 4.13(b) confirms the thickness non-homogeneity of the CdS layer. Localized analyses in point mode are performed at different places typically in the CdTe, CdS and ITO layers. The results [see Fig. 4.13(c)] show that Cd(mnn) and Te(mnn) peaks are detected in CdTe and In(mnn) and O(kll) peaks are detected in ITO. In the layer of CdS (point 2), an additional Te(mnn) peak can also be seen. To show this more clearly, smoothing and numerical derivation of the data are performed [see Fig. 4.13(d)]. A considerable huge Te(mnn) peak is observed in CdS (the blue peak in the inset on the right). This result is consistent with the CdTe/CdS interdiffusion phenomenon observed by ToF-SIMS.

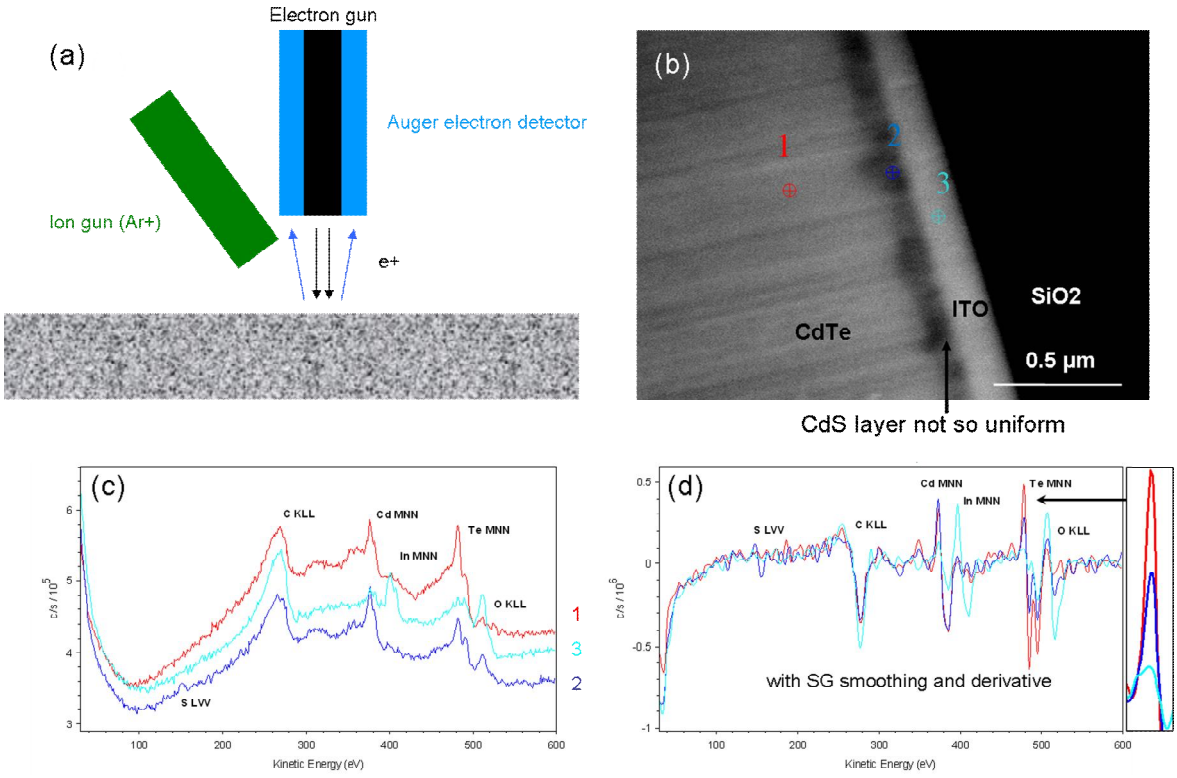

Fig. 4.13 (a) Simplified schematic of SAM system. (b) SEM image of the sample cross-section (c) Scanning Auger Spectroscoy results on 1, 2 and 3 positions indicated in (b). (d)The derivative data of (c) after smoothing.

4.2.4 Effect of the CdS thickness

To study the impact of the CdS layer thickness on electrical characteristics, KFM measurements on sample 1 were compared with measurements on the sample 2, with a CdS layer thickness of 200 nm. The efficiency of the sample 2 is only 5 % compared to 10 % for sample 1, determined according to the AM 1.5 standard.

Typical AFM topography images on the cross-section of sample 1 and sample 2 can be seen respectively on Fig. 4.14(a) and (b). For both, it shows a flat surface after the polishing procedure. Due to the similar stiffness of CdS and CdTe, the CdS layer can barely be seen, whereas the conductive layer, respectively ITO and SnO_2, can be distinguished. The Fig. 4.14 shows also typical CPD mappings obtained in dark for both samples. Starting from the right of the images, there is a slight CPD variation along the CdTe layer probably due to the polycrystalline structure, until we reach the CdTe/CdS interface where a large drop of potential is observed corresponding to the pn heterojunction area. In both cases, the contacts of the sample (i.e. Ag and In contacts) are grounded in order to avoid a transport of charges along the surface. However, as can be seen on the left of the image, a high CPD is observed on the glass substrate probably induced by an accumulation of trapped charges.

The electric field distributions were obtained by calculating the derivative of the surface potential obtained by KFM. Fig. 4.14(a) shows the electric field distribution on sample 1 with both contacts grounded in dark. The presence of a strong electric field at the CdS/CdTe interface is observed corresponding to the heterojunction.

On sample 2 there is an additional peak of high electric field at the SnO_2/CdS interface, as shown on Fig. 4.14(a). It can be seen that KFM is able to resolve these two peaks, whose separation is only 200 nm, demonstrating the potential of the technique. This effect is unexpected and means that there is a second junction, maybe due to material modification due to the Te diffusion. A reason for the lower efficiency of this sample maybe unwanted electron/hole separation increasing the recombination rate. The lower efficiency of sample 2 might be due to a higher recombination rate in the thicker CdS layer.

In order to verify the thicknesses of the different layers and also to check their chemical composition, scanning Auger microscopy is done on the cross-section of the two samples. The thin semiconductors films are close to the glass substrate, which suffers from a strong charging effect due to the electron beam. Therefore, charge neutralization is performed using a low energy Ar beam (70 eV). As a result of low inelastic mean free paths for Auger electrons (about 1 nm), SAM is extremely sensitive to the sample surface. Therefore, to remove the upper hydrocarbon contamination layer, we use Ar sputtering

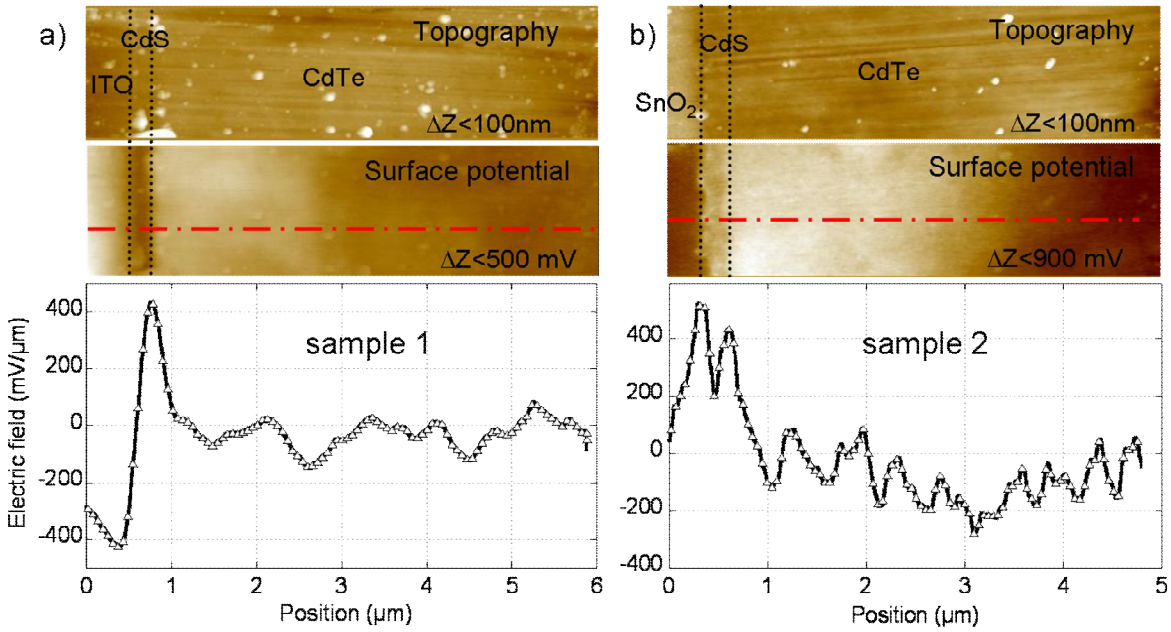

Fig. 4.14 a) Topography and surface potential images obtained on the cross section of sample 1 defined as ITO/CdS/CdTe. Electric field evolution calculated from the surface potential with both contacts grounded. b) Same as in a) but for the sample 2 defined as SnO_2/CdS/CdTe.

(2 keV, 1 µA, raster size of 1 mm × 1 mm, 2 minutes, tilt of 30°) to clean the surface and increase the sensitivity. Figure 4.15 presents the AES line scan on the cross-sections with charge neutralization.

Results of sample 1 show the elements distribution along the cross-section [see Fig. 4.15(a)]. Based on the full-width half-maximum of the sulfur and indium line scans, which are the unique elements present in the CdS and ITO layers respectively, we confirmed the CdS/CdTe and CdS/ITO apparent interfaces previously observed in Fig. 4.14. Moreover, we observed a diffusion of Te into the CdS layer, creating a homogeneous CdS_xTe_{1-x} layer. Since the experiment conditions do not change during the line analysis, the surface stoichiometric ratio of N_{Cd}/N_{Te} can be calculated, assuming that the surface composition is homogeneous over the sampling depth [133]:

$$\frac{N_{Cd}}{N_{Te}} = \frac{I_{Cd}}{I_{Te}} \frac{S_{Te}}{S_{Cd}} \tag{4.3}$$

where I_{Cd} and I_{Te} are AES signal intensities of the Cd(MNN) and Te(MNN) peaks, S_{Cd} and S_{Te} are respectively the sensitivity factors of Cd and Te. Assuming that the ratio of Cd and Te sensitivity factors does not change in CdTe and CdS layers, we have:

$$\frac{N_{Cd}}{N_{Te}} \frac{I_{Te}}{I_{Cd}} = \left(\frac{N_{Cd}}{N_{Te}}\right)' \left(\frac{I_{Te}}{I_{Cd}}\right)' \tag{4.4}$$

where the prime terms apply to the "CdS" layer. Taking the intensity ratios measured for both CdTe and CdS layers into account (see Fig. 4.15), we determine $\left(\frac{N_{Cd}}{N_{Te}}\right)' = 3.64$. This means that instead of CdS the layer is made of $CdS_{0.7}Te_{0.3}$.

The same AES analysis was performed on sample 2. The result is shown on Fig. 4.15(b). Tellurium diffusion into the CdS layer occurred, changing it to CdS_xTe_{1-x}, as in the case of sample1. It can also be seen that the S concentration is significantly lower than in the CdS layer of sample 1, which drastically changes its transparency (CdS has a 80% transparency to visible light while CdTe is not transparent). This might be another reason for the lower efficiency measured on this sample.

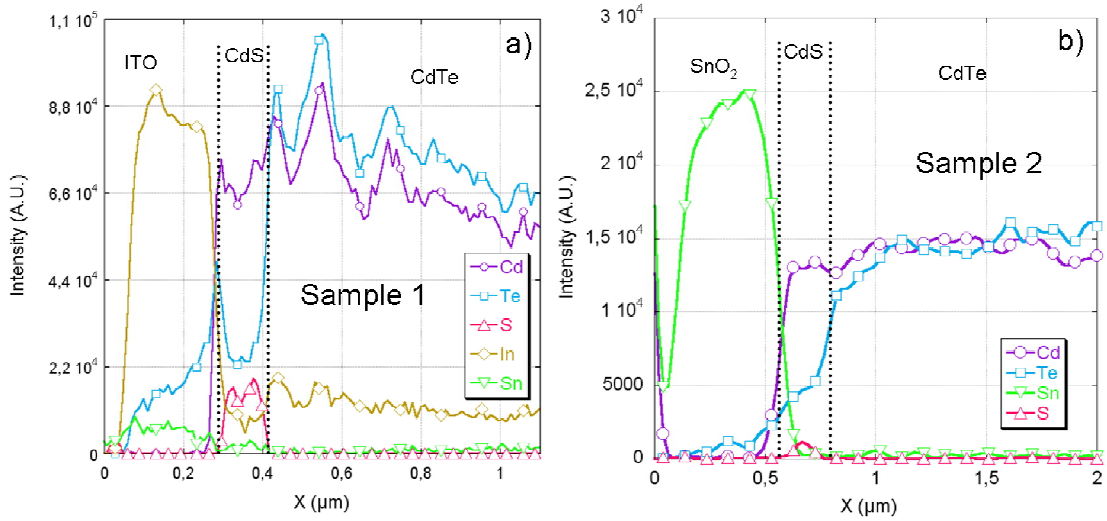

Fig. 4.15 Auger electron spectroscopy line scans on the cross-section respectively for sample 1 (a) and sample 2 (b). An interdiffusion at the CdS/CdTe interface is clearly observed for both samples. Consequently, CdS has turned to be CdS_xTe_{1-x} with a lower S concentration for sample 2 (see details in the text).

4.3 Conclusion

In this work, a protocol of sample preparation on CdTe/CdS thin film solar cell cross-section characterization has been constructed. The combination of KFM and AES has shown the great potential to characterize the electrical and chemical properties of of CdTe/CdS thin film solar cell cross-section. KFM allowed to observe the spreading of the width of the space charge region under forward bias and to resolve two space charge regions which are only separated by 200 nm. In the SAM results we observed the interdiffusion between CdTe and CdS and stoichometrically determined the chemical composition of CdSxTe1-x instead of CdS. It was found that the S content of the thicker CdS layer was significantly lower than that of the thinner CdS layer leading to a lower transparency of the layer.

Conclusions

This thesis deals with two important topics:

- The development of an innovative method for measuring the work function by KFM operating in single-pass both under atmospheric pressure and under secondary vacuum (10^{-6} mbar). The gain in terms of spatial resolution and sensitivity has been demonstrated on graphene layers.
- The application of the KFM method to localize the junction of CdS/CdTe heterostructures used in photovoltaic applications. The KFM measurements were performed with or without illumination. These heterostructures were also characterized by ToF-SIMS and by scanning Auger microscopy.

More specifically, the main conclusions and results of this thesis are summarized hereafter.

Single-scan operation of KFM both in frequency and amplitude modulation mode under ambient conditions:

KFM operating in ambient atmosphere is often used in a common Lift-mode, where the topography and the CPD are *successively* acquired. The single scan operation based on a *simultaneous* acquisition has been developed on commercial AFMs allowing to reduce the time acquisition but also to extend the capabilities of the technique. Both force and force gradient sensitive detection, associated respectively with the frequency modulation (FM) mode and the amplitude modulation (AM) mode, have been implemented. A benchmark of theses modes has been conducted on epitaxial graphene layers. The results show that higher contrasts are achieved using single-scan FM-KFM regardless the tip-sample operating distance. The measurement in AM mode, either in single scan or in Lift-mode, is more dependent on the tip-sample separation. Independently of acquisition mode used, a spatial resolution of about 30 nm is achievable by working at typical tip-sample distance of about 10 nm. However, the CPD contrast stays higher in FM-KFM due to the dominant influence of the tip apex in the electrostatic interaction.

Non-contact imaging and CPD measurement under secondary vacuum:

Under vacuum, organic contamination is better controlled and Q-factors of the cantilever are higher. For these two reasons, accurate and reliable measurements are achievable. By using an external configurable electronic from Nanonis, non-contact imaging and simultaneous CPD measurement under secondary vacuum have been implemented on an Enviroscope™ AFM from Bruker. An important instrumental work has been done to implement this new measurement mode: compatibility issues between electronics, inevitable discrepancies between system calibration, optimization and operating protocols.

Preliminary results on HOPG sample as well as on graphene layers have been obtained, showing that UHV comparable results can be obtained under secondary.

CdTe/CdS heterojunction characterization by complementary techniques:

This work has shown the characterization of the CdTe/CdS heterojunction used in thin film solar cell. High resolved surface potential imaging by KFM have been combined with complementary techniques such as nano-resolved Auger electron spectroscopy (AES), scanning spreading resistance microscopy (SSRM), time-of-flight secondary ion mass spectroscopy (ToF-SIMS) and scanning electronic microscopy (SEM). A protocol for the cross section sample preparation has been specifically developed. Roughness below 1 nm has been achieved. SSRM and SEM imaging has been used to verify the thicknesses of each layer of the solar cell device, which results in a clear observation of the non-uniformity of the CdS thickness. The CPD variation measured on cross section has highlighted the presence of high electric field electric near the CdS/CdTe interface. Moreover, a significant CPD change has been observed under illumination mainly induced by the generation of electrons and holes at the CdTe/CdS interface. On the other hand, the influence of the CdS thickness has been studied because of its dramatic effect on the solar cell efficiency. The efficiency difference can be explained firstly by the presence of an unexpected electric field near the CdS/ITO interface as evidenced by KFM and secondly by a lower transparency of the CdS layer due to the chemical modification induced by the tellurium diffusion occurring at the CdTe/CdS interface. Indeed, the AES and SIMS results revealed the interdiffusion between the CdTe and the CdS layers, generating a CdS_xTe_{1-x} layer. Moreover, the S content is higher in high efficiency sample and lower in low efficiency sample.

Bibliography

[1] E. Wigner and J. Bardeen; **Theory of the Work Functions of Monovalent Metals**; *Physical Review*; 48, 84 (1935).

[2] J. Bardeen; **Theory of the Work Function. II. The Surface Double Layer**; *Physical Review*; 49, 653 (1936).

[3] N. W. Ashcroft and N. D. Mermin; **Solid state physics**; World Publishing Corp., (1976).

[4] H. Lüth; **Solid Surfaces, Interfaces and Thin Films**; Springer Berlin Heidelberg; (2010).

[5] C. Ballif, H. R. Moutinho and M. M. Al-Jassim; **Cross-sectional electrostatic force microscopy of thin-film solar cells**; *Journal of Applied Physics*; 89, 1418 (2001).

[6] G. J. de Raad, D. M. Bruls, P. M. Koenraad and J. H. Wolter; **Interplay between tip-induced band bending and voltage-dependent surface corrugation on GaAs(110) surfaces**; *Physical Review B*; 66, 195306 (2002).

[7] G. Liu, T. Schulmeyer, J. Brötz, A. Klein and W. Jaegermann; **Interface properties and band alignment of Cu2S/CdS thin film solar cells**; *Thin Solid Films*; 431-432, 477 (2003).

[8] H. Narita, A. Kimura, M. Taniguchi, M. Nakatake, T. Xie, S. Qiao, H. Namatame, S. Yang, L. Zhang and E. G. Wang; **Tip-induced band bending effect and local electronic structure of Al nanoclusters on Si(111)**; *Physical Review B*; 78, 115309 (2008).

[9] D. Cahen and A. Kahn; **Electron Energetics at Surfaces and Interfaces: Concepts and Experiments**; *Advanced Materials (Weinheim, Germany)*; 15, 271 (2003).

[10] N. A. Burnham, R. J. Colton and H. M. Pollock; **Interpretation of force curves in force microscopy**; *Nanotechnology*; 4, 64 (1993).

[11] D. P. Woodruff, T. A. Delchar and J. E. Rowe; **Modern Techniques of Surface Science**; *Physics Today*; 41, 90 (1988).

[12] G. Binnig, H. Rohrer, C. Gerber and E. Weibel; **Surface Studies by Scanning Tunneling Microscopy**; *Physical Review Letters*; 49, 57 (1982).

[13] G. Binnig, C. F. Quate and C. Gerber; **Atomic Force Microscope**; *Physical Review Letters*; 56, 930 (1986).

[14] F. J. Giessibl; **Atomic Resolution of the Silicon (111)-(7x7) Surface by Atomic Force Microscopy**; *Science*; 267, 68 (1995).

[15] S. Morita, R. Wiesendanger and E. Meyer; **Noncontact atomic force microscopy**; Springer, (2002).

[16] T. Junno, K. Deppert, L. Montelius and L. Samuelson; **Controlled manipulation of nanoparticles with an atomic force microscope**; *Applied Physics Letters*; 66, 3627 (1995).

[17] E. A. Boer, L. D. Bell, M. L. Brongersma, H. A. Atwater, M. L. Ostraat and R. C. Flagan; **Charging of single Si nanocrystals by atomic force microscopy**; *Applied Physics Letters*; 78, 3133 (2001).

[18] X. Ou, P. D. Kanungo, R. Kögler, P. Werner, U. Gösele, W. Skorupa and X. Wang; **Carrier Profiling of Individual Si Nanowires by Scanning Spreading Resistance Microscopy**; *Nano Letters*; 10, 171 (2009).

[19] P. De Wolf, M. Geva, T. Hantschel, W. Vandervorst and R. B. Bylsma; **Two-dimensional carrier profiling of InP structures using scanning spreading resistance microscopy**; *Applied Physics Letters*; 73, 2155 (1998).

[20] C. D. Bugg and P. J. King; **Scanning capacitance microscopy**; *Journal of Physics E: Scientific Instruments*; 21, 147 (1988).

[21] H.-J. Butt, B. Cappella and M. Kappl; **Force measurements with the atomic force microscope: Technique, interpretation and applications**; *Surface Science Reports*; 59, 1 (2005).

[22] J. E. Sader; **Parallel beam approximation for V-shaped atomic force microscope cantilevers**; *Review of Scientific Instruments*; 66, 4583 (1995).

[23] D. Ziegler; **Techniques to Quantify Local Electric Potentials and Eliminate Electrostatic Artifacts in Atomic Force Microscopy**; (2009).

[24] R. García and R. Pérez; **Dynamic atomic force microscopy methods**; *Surface Science Reports*; 47, 197 (2002).

[25] F. J. Giessibl; **Advances in atomic force microscopy**; *Review of Modern Physics*; 75, 949 (2003).

[26] U. Dürig; **Interaction sensing in dynamic force microscopy**; *New Journal of Physics*; 2, 5 (2000).

[27] P. Martin, S. Marsaudon, J. P. Aimé and B. Bennetau; **Experimental determination of conservative and dissipative parts in the tapping mode on a grafted layer: comparison with frequency modulation data**; *Nanotechnology*; 16, 901 (2005).

[28] Y. Martin, C. C. Williams and H. K. Wickramasinghe; **Atomic force microscope-force mapping and profiling on a sub 100-A scale**; *Journal of Applied Physics*; 61, 4723 (1987).

[29] Y. Sugimoto, S. Innami, M. Abe, O. Custance and S. Morita; **Dynamic force spectroscopy using cantilever higher flexural modes**; *Applied Physics Letters*; 91, 093120 (2007).

[30] S. Sadewasser, P. Jelinek, C.-K. Fang, O. Custance, Y. Yamada, Y. Sugimoto, M. Abe and S. Morita; **New Insights on Atomic-Resolution Frequency-Modulation Kelvin-Probe Force-Microscopy Imaging of Semiconductors**; *Physical Review Letters*; 103, 266103 (2009).

[31] R. Erlandsson, L. Olsson and P. Mårtensson; **Inequivalent atoms and imaging mechanisms in ac-mode atomic-force microscopy of Si(111)7×7**; *Physical Review B*; 54, R8309 (1996).

[32] T. R. Albrecht, P. Grütter, D. Horne and D. Rugar; **Frequency modulation detection using high?Q cantilevers for enhanced force microscope sensitivity**; *Journal of Applied Physics*; 69, 668 (1991).

[33] B. Gotsmann and H. Fuchs; **Dynamic AFM using the FM technique with constant excitation amplitude**; *Applied Surface Science*; 188, 355 (2002).

[34] U. Durig, H. R. Steinauer and N. Blanc; **Dynamic force microscopy by means of the phase-controlled oscillator method**; *Journal of Applied Physics*; 82, 3641 (1997).

[35] M. Gauthier, R. Pérez, T. Arai, M. Tomitori and M. Tsukada; **Interplay between Nonlinearity, Scan Speed, Damping, and Electronics in Frequency Modulation Atomic-Force Microscopy**; *Physical Review Letters*; 89, 146104 (2002).

[36] A. Schirmeisen, H. Hölscher, B. Anczykowski, D. Weiner, M. M. Schäfer and H. Fuchs; **Dynamic force spectroscopy using the constant-excitation and constant-amplitude modes**; *Nanotechnology*; 16, S13 (2005).

[37] T. Glatzel, M. C. Lux-Steiner, E. Strassburg, A. Boag and Y. Rosenwaks; **Principles of Kelvin Probe Force Microscopy**; Springer New York; (2007).

[38] M. Nonnenmacher, M. P. O. Boyle and H. K. Wickramasinghe; **Kelvin probe force microscopy**; *Applied Physics Letters*; 58, 2921 (1991).

[39] L. Kelvin; **Contact electricity of metals**; *Philosophical Magazine*; 46, (1898).

[40] W. A. David, C. Williams, J. Slinkman and H. K. Wickramasinghe; **Lateral dopant profiling in semiconductors by force microscopy using capacitive detection**; *Journal of Vacuum Science and Technology B*; 9, 703 (1991).

[41] A. Kikukawa, S. Hosaka and R. Imura; **Vacuum compatible high-sensitive Kelvin probe force microscopy**; *Review of Scientific Instruments*; 67, 1463 (1996).

[42] T. Glatzel, S. Sadewasser and M. C. Lux-Steiner; **Amplitude or frequency modulation-detection in Kelvin probe force microscopy**; *Applied Surface Science*; 210, 84 (2003).

[43] A. Gil and et al.; **Electrostatic force gradient signal: resolution enhancement in electrostatic force microscopy and improved Kelvin probe microscopy**; *Nanotechnology*; 14, 332 (2003).

[44] Y. Leng, C. C. Williams, L. C. Su and G. B. Stringfellow; **Atomic ordering of GaInP studied by Kelvin probe force microscopy**; *Applied Physics Letters*; 66, 1264 (1995).

[45] K. Kaja; **Developpement de techniques nano-sondes pour la mesure du travail de sortie et application aux materiaux en microelectronique**; (2010).

[46] U. Zerweck, C. Loppacher, T. Otto, S. Grafström and L. M. Eng; **Accuracy and resolution limits of Kelvin probe force microscopy**; *Physical Review B*; 71, 125424 (2005).

[47] S. Hudlet, M. S. Jean, C. Guthmann and J. Berger; **Evaluation of the capacitive force between an atomic force microscopy tip and a metallic surface**; *European Physical Journal B: Condensed Matter Physics*; 2, 5 (1998).

[48] S. Belaidi, P. Girard and G. Leveque; **Electrostatic forces acting on the tip in atomic force microscopy: Modelization and comparison with analytic expressions**; *Journal of Applied Physics*; 81, 1023 (1997).

[49] H. O. Jacobs, P. Leuchtmann, O. J. Homan and A. Stemmer; **Resolution and contrast in Kelvin probe force microscopy**; *Journal of Applied Physics*; 84, 1168 (1998).

[50] J. Colchero, A. Gil and A. M. Baró; **Resolution enhancement and improved data interpretation in electrostatic force microscopy**; *Physical Review B*; 64, 245403 (2001).

[51] H. Jacobs; **Methods to measure and modify electrical properties on a nanometer scale and their applications in science and technology** (1999).

[52] S. Hudlet, M. S. Jean, B. Roulet, J. Berger and C. Guthmann; **Electrostatic forces between metallic tip and semiconductor surfaces**; *Journal of Applied Physics*; 77, 3308 (1995).

[53] K. Kaja, N. Chevalier, D. Mariolle, F. Bertin, G. Feuillet and A. Chabli; **Effects of Experimental Parameters on the Work Function Measurement: A Kelvin Force Microscopy Study**; *AIP Conference Proceedings*; 1173, 224 (2009).

[54] N. A. Burnham, A. J. Kulik, G. Gremaud and G. A. D. Briggs; **Nanosubharmonics: The Dynamics of Small Nonlinear Contacts**; *Physical Review Letters*; 74, 5092 (1995).

[55] G. Koley; **Surface potential measurements on GaN and AlGaN/GaN heterostructures by scanning Kelvin probe microscopy**; *Journal of Applied Physics*; 90, 337 (2001).

[56] A. Liscio, V. Palermo, K. Mullen and P. Samorì; **Tip-sample Interactions in Kelvin Probe Force Microscopy: Quantitative Measurement of the Local Surface Potential**; *The Journal of Physical Chemistry C*; 112, 17368 (2008).

[57] R. Smoluchowski; **Anisotropy of the Electronic Work Function of Metals**; *Physical Review*; 60, 661 (1941).

[58] C. J. Fall, N. Binggeli and A. Baldereschi; **Work-function anisotropy in noble metals: Contributions from d states and effects of the surface atomic structure**; *Physical Review B*; 61, 8489 (2000).

[59] L. Maciej, M. Daniel, A. Miftahul, M. Takeshi, J. Ryszard and T. Michiharu; **Observation of individual dopants in a thin silicon layer by low temperature Kelvin Probe Force Microscope**; *Applied Physics Letters*; 93, 142101 (2008).

[60] K. Sridhara, L. Borowik, D. Mariolle, N. Chevalier and J.-P. Colonna; **Environment and baking influence on charge retention on silicon nitride charge trap layers**; *Journal of Applied Physics*; 111, 023710.

[61] N. Kobayashi, H. Asakawa and T. Fukuma; **Nanoscale potential measurements in liquid by frequency modulation atomic force microscopy**; *Review of Scientific Instruments*; 81, 123705.

[62] F. Bocquet, L. Nony, C. Loppacher and T. Glatzel; **Analytical approach to the local contact potential difference on (001) ionic surfaces: Implications for Kelvin probe force microscopy**; *Physical Review B (Condensed Matter and Materials Physics)*; 78, 035410 (2008).

[63] Y. Rosenwaks, S. Saraf, O. Tal, A. Schwarzman, T. Glatzel and M. Lux-Steiner; **Kelvin Probe Force Microscopy of Semiconductors**; (2007).

[64] T. Glatzel, L. Zimmerli and E. Meyer; **Molecular Assemblies on Insulating Ultrathin Films Analyzed by NC-AFM and KPFM**; *Israel Journal of Chemistry*; 48, 107 (2008).

[65] W. Melitz, J. Shen, A. C. Kummel and S. Lee; **Kelvin probe force microscopy and its application**; *Surface Science Reports*; 66, 1 (2011).

[66] D. Ziegler and S. Andreas; **Force gradient sensitive detection in lift-mode Kelvin probe force microscopy**; *Nanotechnology*; 22, 075501 (2011).

[67] S. Kitamura, K. Suzuki and M. Iwatsuki; **High resolution imaging of contact potential difference using a novel ultrahigh vacuum non-contact atomic force microscope technique**; *Applied Surface Science*; 140, 265 (1999).

[68] X. D. Ding, J. An, J. B. Xu, C. Li and R. Y. Zeng; **Improving lateral resolution of electrostatic force microscopy by multifrequency method under ambient conditions**; *Applied Physics Letters*; 94, 223109 (2009).

[69] E. Palacios-Lidon, B. Perez-Garcia and J. Colchero; **Enhancing dynamic scanning force microscopy in air: as close as possible**; *Nanotechnology*; 20, 085707 (2009).

[70] P. Girard, M. Ramonda and D. Saluel; **Electrical contrast observations and voltage measurements by Kelvin probe force gradient microscopy**; *Journal of Vacuum Science and Technology B: Microelectronics and Nanometer Structures*; 20, 1348 (2002).

[71] A. Kikukawa, S. Hosaka and R. Imura; **Silicon pn junction imaging and characterizations using sensitivity enhanced Kelvin probe force microscopy**; *Applied Physics Letters*; 66, 3510 (1995).

[72] A. John, M. Sergei and M. Martin; **Topography and surface potential in Kelvin force microscopy of perfluoroalkyl alkanes self-assemblies**; *Journal of Vacuum Science and Technology B*; 27, 903 (2009).

[73] S. C. Gupta; **Phase-locked loops**; *Proceedings of the IEEE*; 63, 291 (1975).

[74] S. Barbet, R. Aubry, M. A. di Forte-Poisson, J. C. Jacquet, D. Deresmes, T. Melin and D. Theron; **Surface potential of n- and p-type GaN measured by Kelvin force microscopy**; *Applied Physics Letters*; 93, 212107 (2008).

[75] L. Justin; **The effect of drive frequency and set point amplitude on tapping forces in atomic force microscopy: simulation and experiment**; *Nanotechnology*; 20, 245703 (2009).

[76] Y. Ebenstein, E. Nahum and U. Banin; **Tapping Mode Atomic Force Microscopy for Nanoparticle Sizing: Tip-Sample Interaction Effects**; *Nano Letters*; 2, 945 (2002).

[77] T. R. Rodriguez and R. Garcia; **Tip motion in amplitude modulation (tapping-mode) atomic-force microscopy: Comparison between continuous and point-mass models**; *Applied Physics Letters*; 80, 1646 (2002).

[78] L. NONY; **Analyse de la microscopie de force dynamique : application à l'étude de l'A.D.N.**; (2000).

[79] P. Bleuet, P. Cloetens, P. Gergaud, D. Mariolle, N. Chevalier, R. Tucoulou, J. Susini and A. Chabli; **A hard x-ray nanoprobe for scanning and projection nanotomography**; *Review of Scientific Instruments*; 80, 056101 (2009).

[80] T. Filleter, K. V. Emtsev, S. Th and R. Bennewitz; **Local work function measurements of epitaxial graphene**; *Applied Physics Letters*; 93, 133117 (2008).

[81] D. Ziegler, P. Gava, uuml, J. ttinger, F. Molitor, L. Wirtz, M. Lazzeri, A. M. Saitta, A. Stemmer, F. Mauri and C. Stampfer; **Variations in the work function of doped single- and few-layer graphene assessed by Kelvin probe force microscopy and density functional theory**; *Physical Review B*; 83, 235434 (2011).

[82] T. Seyller, A. Bostwick, K. V. Emtsev, K. Horn, L. Ley, J. L. McChesney, T. Ohta, J. D. Riley, E. Rotenberg and F. Speck; **Epitaxial graphene: a new material**; *physica status solidi (b)*; 245, 1436 (2008).

[83] C. Virojanadara, M. Syväjarvi, R. Yakimova, L. I. Johansson, A. A. Zakharov and T. Balasubramanian; **Homogeneous large-area graphene layer growth on 6H-SiC(0001)**; *Physical Review B*; 78, 245403 (2008).

[84] H. Hibino, H. Kageshima, M. Kotsugi, F. Maeda, F. Z. Guo and Y. Watanabe; **Dependence of electronic properties of epitaxial few-layer graphene on the number of layers investigated by photoelectron emission microscopy**; *Physical Review B*; 79, 125437 (2009).

[85] Ł. Borowik, K. Kusiaku, D. Théron and T. Mélin; **Calculating Kelvin force microscopy signals from static force fields**; *Applied Physics Letters*; 96, 103119 (2010).

[86] L. Portes, P. Girard, R. Arinero and M. Ramonda; **Force gradient detection under vacuum on the basis of a double pass method**; *Review of Scientific Instruments*; 77, 096101 (2006).

[87] C. Sommerhalter, T. Glatzel, T. W. Matthes, A. Jäger-Waldau and M. C. Lux-Steiner; **Kelvin probe force microscopy in ultra high vacuum using amplitude modulation detection of the electrostatic forces**; *Applied Surface Science*; 157, 263 (2000).

[88] S. Hudlet, M. Saint Jean, C. Guthmann and J. Berger; **Evaluation of the capacitive force between an atomic force microscopy tip and a metallic surface**; *The European Physical Journal B - Condensed Matter and Complex Systems*; 2, 5 (1998).

[89] M. J. Gordon and T. Baron; **Amplitude-mode electrostatic force microscopy in UHV: Quantification of nanocrystal charge storage**; *Physical Review B*; 72, 165420 (2005).

[90] H. O. Jacobs, H. F. Knapp, S. Müller and A. Stemmer; **Surface potential mapping: A qualitative material contrast in SPM**; *Ultramicroscopy*; 69, 39 (1997).

[91] J. Jacobs, B. Hamilton, E. Whittaker, U. Bangert and M. Missous; **Imaging sub-surface dopant and free electron distributions using scanning tunneling microscopy**; *Institut of Physics Conference Series*; 164, 633 (1999).

[92] D. Ziegler, N. Naujoks and A. Stemmer; **Feed-forward compensation of surface potential in atomic force microscopy**; *Review of Scientific Instruments*; 79, 063704 (2008).

[93] D. Ziegler, J. Rychen, N. Naujoks and A. Stemmer; **Compensating electrostatic forces by single-scan Kelvin probe force microscopy**; *Nanotechnology*; 18, 225505 (2007).

[94] T. Glatzel, H. Hoppe, N. S. Sariciftci, M. C. Lux-Steiner and M. Komiyama; **Kelvin Probe Force Microscopy Study of Conjugated Polymer/Fullerene Organic Solar Cells** *Japanese Journal of Applied Physics*; 44, 5370 (2005).

[95] T. Glatzel, M. Rusu, S. Sadewasser and M. C. Lux-Steiner; **Surface photovoltage analysis of thin CdS layers on polycrystalline chalcopyrite absorber layers by Kelvin probe force microscopy**; *Nanotechnology*; 19, 145705 (2008).

[96] K. Shin'ichi and I. Masashi; **High-resolution imaging of contact potential difference with ultrahigh vacuum noncontact atomic force microscope**; *Applied Physics Letters*; 72, 3154 (1998).

[97] E. J. Spadafora, R. Demadrille, B. Ratier and B. Grelì vin; **Imaging the Carrier Photogeneration in Nanoscale Phase Segregated Organic Heterojunctions by Kelvin Probe Force Microscopy**; *Nano Letters*; 10, 3337 (2010).

[98] Y. Martin, C. C. Williams and H. K. Wickramasinghe; **Atomic force microscope--force mapping and profiling on a sub 100-[A-ring] scale**; *Journal of Applied Physics*; 61, 4723 (1987).

[99] B. Francois; **Cours de microscopie a froce atomique**; CEA-LETI, (2005).

[100] L. Nony, A. Baratoff, D. Schar, O. Pfeiffer, A. Wetzel and E. Meyer; **Noncontact atomic force microscopy simulator with phase-locked-loop controlled frequency detection and excitation**; *Physical Review B (Condensed Matter and Materials Physics)*; 74, 235439 (2006).

[101] H. Bluhm, A. Wadas, R. Wiesendanger, K. P. Meyer and L. Szczes-acuteniak; **Electrostatic force microscopy on ferroelectric crystals in inert gas atmosphere**; *Physical Review B*; 55, 4 (1997).

[102] R. M. Nyffenegger, R. M. Penner and R. Schierle; **Electrostatic force microscopy of silver nanocrystals with nanometer-scale resolution**; *Applied Physics Letters*; 71, 1878 (1997).

[103] A. Baalmann and V. Schlett; **AES and XPS investigations for the topochemical characterization of dope elements on WC powders**; *Fresenius' Journal of Analytical Chemistry*; 341, 200 (1991).

[104] E. Hoque, J. A. DeRose, P. Hoffmann, H. J. Mathieu, B. Bhushan and M. Cichomski; **Phosphonate self-assembled monolayers on aluminum surfaces**; *The Journal of Chemical Physics*; 124, 174710 (2006).

[105] K. Zweibel; **The Impact of Tellurium Supply on Cadmium Telluride Photovoltaics**; *Science*; 328, 699 (2010).

[106] K. L. Chopra, P. D. Paulson and V. Dutta; **Thin-film solar cells: an overview**; *Progress in Photovoltaics: Research and Applications*; 12, 69 (2004).

[107] J. L. Joseph; **Theoretical Considerations Governing the Choice of the Optimum Semiconductor for Photovoltaic Solar Energy Conversion**; *Journal of Applied Physics*; 27, 777 (1956).

[108] M. Burgelman; **Cadmium Telluride Thin Film Solar Cells: Characterization, Fabrication and Modeling**; John Wiley & Sons, Ltd, Chichester, UK, (2006).

[109] A. Morales-Acevedo; **Can we improve the record efficiency of CdS/CdTe solar cells?**; *Solar Energy Materials and Solar Cells*; 90, 2213 (2006).

[110] S. Major, A. Banerjee and K. L. Chopra; **Highly transparent and conducting indium-doped zinc oxide films by spray pyrolysis**; *Thin Solid Films*; 108, 333 (1983).

[111] N. Romeo, A. Bosio, V. Canevari, M. Terheggen and L. Vaillant Roca; **Comparison of different conducting oxides as substrates for CdS/CdTe thin film solar cells**; *Thin Solid Films*; 431–432, 364 (2003).

[112] J. Britt and C. Ferekides; **Thin-film CdS/CdTe solar cell with 15.8% efficiency**; *Applied Physics Letters*; 62, 2851 (1993).

[113] M. Z. Ruud E. I. Schropp; **Amorphous and microcrystalline silicon solar cells: modeling, materials, and device technology**; Kluwer Academic Publishers, Boston, (1998).

[114] W. Xuanzhi; **High-efficiency polycrystalline CdTe thin-film solar cells**; *Solar Energy*; 77, 803 (2004).

[115] S. Saha, U. Pal, A. K. Chaudhuri, V. V. Rao and H. D. Banerjee; **Optical Properties of CdTe Thin Films**; *physica status solidi (a)*; 114, 721 (1989).

[116] J. M. Dona and J. Herrero; **Chemical Bath Deposition of CdS Thin Films: Electrochemical In Situ Kinetic Studies**; *Journal of the Electrochemical Society*; 139, 2810 (1992).

[117] D. H. Rose, F. S. Hasoon, R. G. Dhere, D. S. Albin, R. M. Ribelin, X. S. Li, Y. Mahathongdy, T. A. Gessert and P. Sheldon; **Fabrication procedures and process sensitivities for CdS/CdTe solar cells**; *Progress in Photovoltaics: Research and Applications*; 7, 331 (1999).

[118] R. Mendoza-Perez, G. Santana-Rodriaguez, J. Sastre-Hernandez, A. Morales-Acevedo, A. Arias-Carbajal, O. Vigil-Galan, J. C. Alonso and G. Contreras-Puente; **Effects of thiourea concentration on CdS thin films grown by chemical bath deposition for CdTe solar cells**; *Thin Solid Films*; 480-481, 173 (2005).

[119] N. Abbas Shah, A. Ali, Z. Ali, A. Maqsood and A. K. S. Aqili; **Properties of Te-rich cadmium telluride thin films fabricated by closed space sublimation technique**; *Journal of Crystal Growth*; 284, 477 (2005).

[120] N. Abbas Shah, A. Ali, A. K. S. Aqili and A. Maqsood; **Physical properties of Ag-doped cadmium telluride thin films fabricated by closed-space sublimation technique**; *Journal of Crystal Growth*; 290, 452 (2006).

[121] N. Romeo, A. Bosio, V. Canevari and A. PodestÃ **Recent progress on CdTe/CdS thin film solar cells**; *Solar Energy*; 77, 795 (2004).

[122] T. L. Chu; **Thin film cadmium telluride solar cells by two chemical vapor deposition techniques**; *Solar Cells*; 23, 31 (1988).

[123] H. R. Moutinho, R. G. Dhere, C. Ballif, M. M. Al-Jassim and L. L. Kazmerski; **Alternative procedure for the fabrication of close-spaced sublimated CdTe solar cells**; *The 46th international symposium of the american vacuum society*; 18, 1599 (2000).

[124] H. R. Moutinho, M. M. Al-Jassim, D. H. Levi, P. C. Dippo and L. L. Kazmerski; **Effects of CdCl2 treatment on the recrystallization and electro-optical properties of CdTe thin films**; 16; pp.1251 (1998).

[125] J.-H. Lee and D.-J. Lee; **Effects of CdCl2 treatment on the properties of CdS films prepared by r.f. magnetron sputtering**; *Thin Solid Films*; 515, 6055 (2007).

[126] K. Durose, P. R. Edwards and D. P. Halliday; **Materials aspects of CdTe/CdS solar cells**; *Journal of Crystal Growth*; 197, 733 (1999).

[127] G. Liu, T. Schulmeyer, J. Brötz, A. Klein and W. Jaegermann; **Interface properties and band alignment of Cu2S/CdS thin film solar cells**; *Thin Solid Films*; 431–432, 477 (2003).

[128] A. Alnajjar, S. A. Jawad and N. Yusuf; **Investigation of ohmic contact to P-type CdTe:P using ac and dc techniques**; *Renewable Energy*; 27, 417 (2002).

[129] E. Centurioni and D. Iencinella; **Role of front contact work function on amorphous silicon/crystalline silicon heterojunction solar cell performance**; *Electron Device Letters, IEEE*; 24, 177 (2003).

[130] J. L. Freeouf and J. M. Woodall; **Schottky barriers: An effective work function model**; *Applied Physics Letters*; 39, 727 (1981).

[131] H. R. Moutinho, R. G. Dhere, C. S. Jiang, Y. Yan, D. S. Albin and M. M. Al-Jassim; **Investigation of potential and electric field profiles in cross sections of CdTe/CdS solar cells using scanning Kelvin probe microscopy**; *Journal of Applied Physics*; 108, 074503 (2010).

[132] F. Giannazzo, P. Fiorenza and V. Raineri; **Applied Scanning Probe Methods X**; Springer Berlin Heidelberg; (2008).

[133] M. C. Burrell and N. R. Armstrong; **Stoichiometry and thickness of the initial oxide formed on clean titanium surfaces determined by quantitative Auger electron spectroscopy, electron energy loss spectroscopy, and microgravimetry**; *Journal of Vacuum Science & Technology A: Vacuum, Surfaces, and Films*; 1, 1831 (1983).